ABSTRACT

Title of Document: CELLULAR CONTACT GUIDANCE THROUGH DYNAMIC SENSING OF NANOTOPOGRAPHIES VIA ACTIN POLYMERIZATION WAVES.

Xiaoyu Sun, Doctor of Philosophy, 2015

Directed By: Professor John T. Fourkas,
Department of Chemistry and Biochemistry

Many biological and physiological processes depend upon directed migration of cells, which is typically mediated by chemical or physical gradients. However, conventional chemical or physical gradients have finite dynamic range and can therefore operate only over limited distances. Cells can overcome this limitation by relaying chemotactic signals, but chemical relay of directional information requires intricate orchestration of timing of signals. Nanotopographies that are on a comparable length scale with the features in the extracellular matrix offer an option to guide cells over large distances without a global gradient.

Here I show that both cell motion and actin-wave propagation in *Dictyostelium discoideum* (*D. discoideum*) are guided bidirectionally on nanoridges/nanogrooves. The guidance efficiency depends on the ridge spacing. Actin polymerization preferentially occurs around individual ridges, giving rise to coupled actin streaks on the opposite sides of a single ridge. Cells can be guided in a single preferred direction

based solely on local asymmetries in nanosawteeth on subcellular scales, which can be repeated over arbitrarily large areas, providing directional guidance over an unlimited distance. The direction and strength of the guidance is sensitive to the details of the nanosawteeth, suggesting that this phenomenon plays a context-dependent role *in vivo*. I demonstrate that asymmetric nanosawteeth guide the direction of internal actin polymerization waves, and that cells move in the same direction as these waves. This phenomenon is observed both for the pseudopod-dominated migration of the amoeboid *D. discoideum* and for the lamellipod-driven migration of human neutrophils. The conservation of this mechanism across cell types and the asymmetric shape of many natural scaffolds suggest that actin-wave-based guidance is important in biology and physiology.

Even symmetric nanotopographies can induce unidirectional bias in actin-wave propagation and cell motion. This bias presumably originates from the intrinsic actin chirality. A counterclockwise bias in both cell motion and actin-wave propagation is observed in *D. discoideum* migrating on 0.8-μm-spaced nanorings and in neutrophils migrating on 2-μm-spaced nanorings. The different effects of ring spacing on guidance efficiency between *D. discoideum* and neutrophils may arise from the difference in the ultrastructure of the actin network between those two cell types.

CELLULAR CONTACT GUIDANCE THROUGH DYNAMIC SENSING OF NANOTOPOGRAPHIES VIA ACTIN POLYMERIZATION WAVES

By

Xiaoyu Sun

Dissertation submitted to the Faculty of the Graduate School of the
University of Maryland, College Park, in partial fulfillment
of the requirements for the degree of
Doctor of Philosophy
2015

Advisory Committee:
Professor John T. Fourkas, Chair
Professor Wolfgang Losert, Co-advisor
Professor Norma Andrews, Dean's Representative
Professor Neil Blough
Professor Zhihong Nie
Professor YuHuang Wang

Acknowledgements

First and foremost, I would like to thank my advisor, Dr. John Fourkas, who is genuinely kind and always amazes me with brilliant scientific ideas. It was his guidance and encouragements that made almost everything described in this thesis possible. His optimism, creativity and curiosity, have influenced me a lot for the past few years and will influence me later on through my life. I would also like to thank my co-advisor, Dr. Wolfgang Losert, for introducing a whole new world of biophysics to me. Dr. Losert is always enthusiastic about science and available to give advice, and provide brainstorming solutions from an interdisciplinary perspective. I am fortunate to work under the guidance of both of them, and will forever look up to them.

I would also like to thank my dear parents, who always care about me and have confidence in me. They ignited my interests in science when I was a kid, and encouraged me to pursue my dreams and always try to be a better self with every effort. They instilled in me the strong values of diligence, modesty and perseverance, without which I would never be able to complete all of the work detailed in this thesis.

I would also like to thank everyone in the Fourkas and Losert Groups for their unconditional help and support: Meghan Driscoll, for all the incredible suggestions and ideas she offered as a research mentor and the happy hours we spent together as friends; Satarupa Das, for all the help she offered in the neutrophil experiments and suggestions she provided as a cell biologist; Sijia Qin, the first person who taught me how to perform nanofabrication with MAP and who was always available to help; Chenlu Wang, for all the seminal discussions on *Dictyostelium discoideum* and actin

waves, and for being the best friend I could ever imagine (I will always miss the delicious dumplings, hot pots and barbecues she prepared for me); Can Guven, for the helpful discussion on the actin wave modeling; Sanghee Nah, for being such a great friend (I will always cherish the coffee talks and shopping time with her, and the cute cupcakes she brought for me when I was running late in lab); Matt Hourwitz, who is always ready to help and cheer me up with his jokes; and Lexi Suberi, for taking care of my cell cultures and inviting me to the fancy Thanksgiving party with her family. I cannot forget Floyd Bates, John Bender, Leonard Campanello, Desu Chen, Samuel Cohen, Dr. Farah Dawood, Dr. Samrat Dutta, Dr. Matt Harrington, Dr. Xiaoxiao He, Deborah Hemingway, Chris Hernandez, Dr. George Kumi, Rachel Lee, Dr. Jarrett Leeds, Dr. Nikolaos Liaros, Dr. Kathleen Monaco, EChO Ory, Dr. Joshua Parker, Sandra Razo, Dr. Chris Rivera, Yang Shen, Dr. Alison Sikorsky, Amanda Souna, Dr. Mike Stocker, and Zulya Tomova.

I would also like to thank several individuals from outside of my research groups, who have helped with my research in various ways: Dr. Carole Parent, for providing valuable comments on my paper; Dr. Paul Kriebel, for providing *Dictyostelium discoideum* cells, as well as pivotal and detailed suggestions on my experiments; Dr. Orion Weiner, for providing the actin-YFP neutrophil-like HL-60 cells; Dr. Amy Beaven, for training me on the Leica SP5 confocal microscope; Dr. Tim Maugel and Dr. Larry Lai, for training me on the scanning electron microscope; Dr. Karen Gaskell, for training me on the atomic force microscope; and Dr. Dong Hun Park, for his help on the reactive ion etching.

Finally, I thank the members of my committee: Professor John T. Fourkas, Professor Norma Andrews, Professor Neil Blough, Professor Wolfgang Losert, Professor Zhihong Nie, and Professor Yuhuang Wang.

Table of Contents

List of Tables

List of Figures

Chapter 1: Introduction

1.1. Cell migration

Directed cell migration is essential for many critical biological and physiological processes (*1*), such as embryonic development (*2*), wound healing (*3*), immune response (*4*) and angiogenesis (*5*). The modes and mechanisms that cells adopt in their migration are cell-type and context dependent. For instance, macrophages and neutrophils migrate as single entities to defend against bacterial infection (*6, 7*); *Dictyostelium discoideum* (*D. discoideum*) cells tend to stream and aggregate upon starvation, and migrate as slugs to feed (*8*); epithelial cells migrate as a sheet to close a wound (*9*). The failure of cell migration, or the migration of cells to inappropriate sites, can lead to congenital defects or severe diseases in adults, such as vascular disease, autoimmune syndrome, defective wound healing, and cancer metastasis. Understanding the mechanisms by which cells migrate will provide insight into developing new therapeutics to cure those diseases and will help to improve the properties of artificial tissues used in transplantation.

The typical migration of an individual cell on a 2D surface is a cyclic process that has been categorized into five successive steps (Figure 1.1) (*10*). The first step is morphological polarization. Cells prepare for migration by acquiring an asymmetric spatial distribution of cytoskeletal components (*e.g.* microtubules) and molecules (*e.g.* protein receptors), and establishing a clear distinction between the front and the rear.

The second step is membrane extension. Actin polymerization, which will be discussed in detail in Section 1.3, exerts force on the leading edge of the plasma membrane, and thus pushes it forward. Another model explains the membrane extension by an "elastic Brownian ratchet," in which thermal energy bends the nascent short actin filaments, and unbending of the elongated filaments against the leading edge generates force to push the membrane forward. The third step is the formation of adhesion. The adhesion of a cell's ventral membrane to the substrate can either be stable and specific, as the ones observed in fibroblasts, or be transient and non-specific, as the ones observed in *D. discoideum*. The fourth step is contraction and translocation of the cell body. Myosin-based contraction of actin filaments generates contractive force on the cytoplasm. Adhesions serve as traction sites as the cell migrates over them. The last step is rear release. For integrin-based focal adhesions, proteolytic cleavage and integrin endocytosis may be required for the rear detachment. However, for transient and non-specific adhesion, the contraction generated by myosin at the back of a cell is sufficient to release the rear. All of these steps coordinate and cycle elaborately, enabling an individual cell to move.

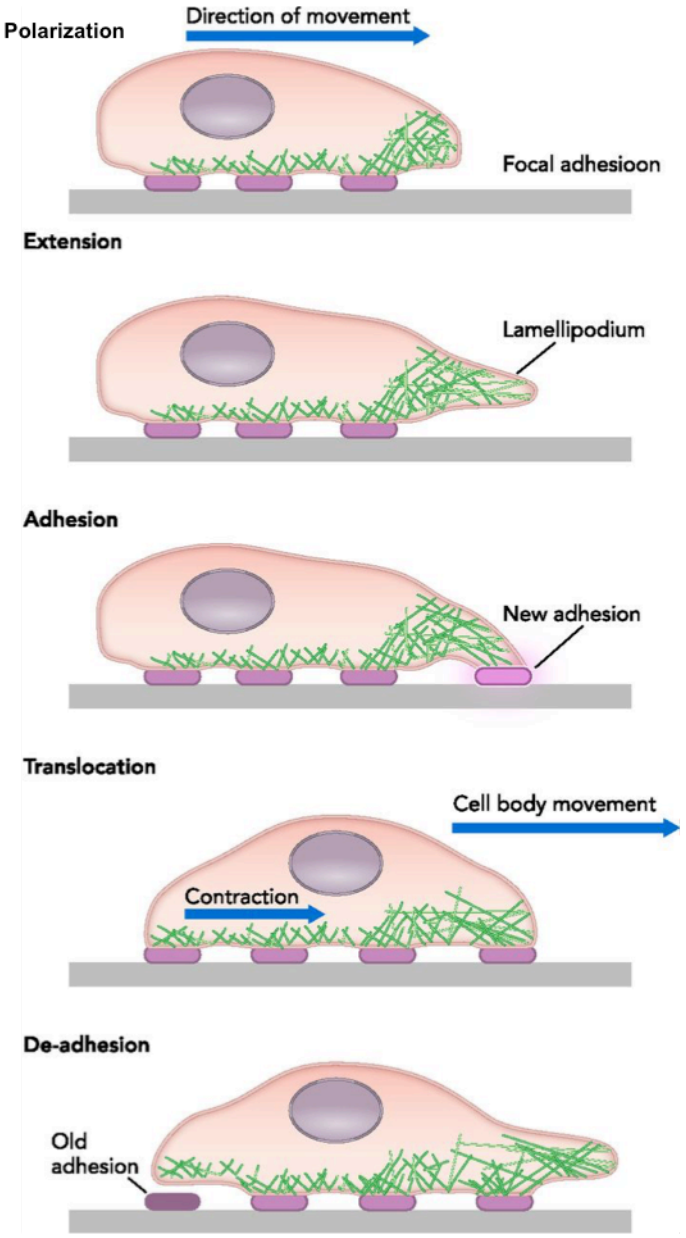

Figure 1.1. Schematic representation of the five-step cyclic process of cell migration on a 2D surface (*11*).

Amoeboid migration is a common cell migration mode that is adopted by fast-moving and weakly adhesive cells, such as *D. discoideum* and neutrophil-like HL-60

cells, which were used in the work presented in this thesis. Tumor cells can also switch to an amoeboid morphology under certain conditions to disseminate from the primary tumor and invade a distant tissue (*12*). Studying amoeboid migration will thus shed light on the mechanism of cancer metastasis. Amoeboid migration is characterized by the actin-polymerization-generated protrusion in the anterior of the cell and myosin-contraction-generated retraction in the posterior of the cell. It has been shown that on a high-adhesivity surface, both actin polymerization and myosin contraction are required for a cell to move efficiently, whereas on a low-adhesivity surface, actin polymerization alone is sufficient to propel the whole cell forward (*13*). Because the surfaces used in this thesis work exhibit moderate adhesivity, I will mainly focus on the effect of actin polymerization on cell migration.

Because most events of cell migration that occur in a physiological context exhibit various degrees of directionality, many studies have attempted to guide cell migration in a particular direction. It has been demonstrated that guidance of cells can be achieved through external gradients in properties such as chemical concentration (chemotaxis) (*14, 15*), substrate rigidity (durotaxis) (*16*), electric field (electrotaxis) (*17, 18*), and adhesion (haptotaxis) (*19*). However, the total distance over which gradients can guide cells is limited by the finite dynamic range of cellular sensing. Although cells can overcome this limitation by relaying chemotactic signals, chemical relay of directional information requires intricate orchestration and timing of signals (*7, 8, 15*). Shear flow is another approach to guide cells unidirectionally over large distances, but it is an active process that requires constant fluid flow.

Additionally, the flow rate and the viscosity of the fluid need to be controlled precisely to produce an accurate shear stress (*20, 21*).

The extracellular matrix (ECM) in a physiological system not only provides a molecular frame for specific cell-matrix adhesion, but also serves as a mechanical frame for cell migration that provides a specific density, gap size, stiffness, and orientation. Provenzano and coworkers have found that a radial reorganization of collagen fibers surrounding tumors facilitates tumor cell invasion by providing a structural guidance along which the cells can migrate (*22*). This directional cell migration is attributed to physical contact guidance. As a passive method that does not require a global gradient, contact guidance is a superior approach to guide cells over large distances. With the development of micro- and nanofabrication techniques, various structures that mimic the features in ECM can be created and used in the study of directed cell migration. The next section will discuss previous studies on contact guidance in detail.

1.2. Contact guidance

Contact guidance is an approach to guide cell migration with shapes or topographies that are on the micro- or nano-scale. In early studies, artificial or natural fibers and interfaces were used to guide a group of cells or a whole explant (*23-26*). Individual *D. discoideum* cells were found to align along 2 to 5 μm wide grooves on agar films (Figure 1.2A) (*27*). Later, micro- or nano-scale ridges and grooves fabricated with photolithography (Figure 1.2B) (*28-35*), as well as oriented fibers constructed with proteins (Figure 1.2C) (*36*), copolymers (*37*), and carbon nanotubes

(*38*), were shown to guide cell alignment or migration in parallel with those features. Table 1 is a brief summary of the various studies on contact guidance of different cell types. Recently, Yamada and coworkers have shown that oriented fibronectin fibers guide not only cell alignment, but also the alignment of intracellular actin stress fibers in parallel (Figure 1.2D) (*39*), indicating that cell alignment could result from actin alignment. Topographies with a feature size of hundreds of nanometers are on a length scale that is comparable to that of cytoskeletal components, such as actin. Therefore, the main focus of this thesis is the effect of nanotopography on actin polymerization, and the subsequent effect on cellular contact guidance.

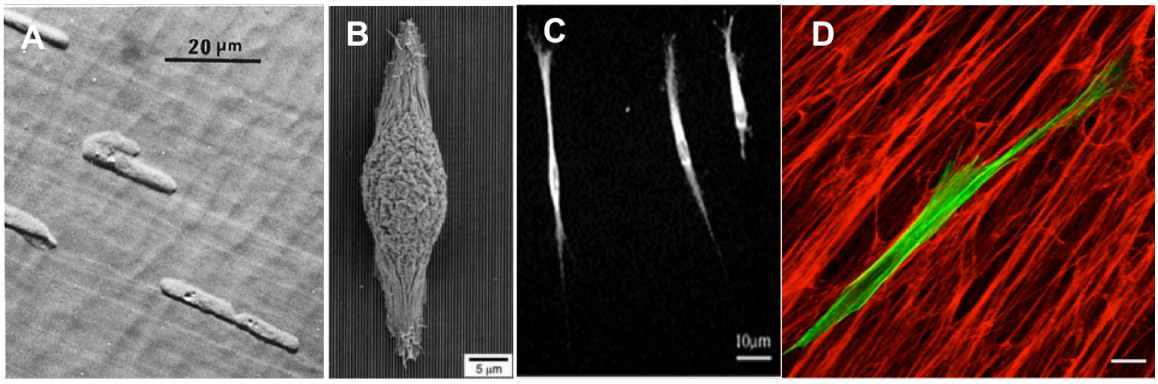

Figure 1.2. Contact guidance manifested in different cell types. (A) *D. discoideum* cells align along microgrooves on an agar film (*27*). Scale bar, 20 μm. (B) A human corneal epithelial cell align along nanoridges (*34*). Scale bar, 5 μm. (C) Endothelial cells align along vertically oriented collagen fibers (*36*). Scale bar, 10 μm. (D) The intracellular stress fibers (green) in a fibroblast align along the oriented fibronectin fibers (red) (*39*). Scale bar, 20 μm.

Table 1. Contact guidance of different cell types on various topographies.

Cell type	Topography	Guidance effect
Mesenchymal cells	Grooves that are 1 to 4 μm wide and 1 μm deep (*28*)	Cell migration is predominantly parallel to the grooves.
Fibroblasts	Grooves that are 1-10 μm wide and 1 μm deep (*29*)	Fibroblasts align along the grooves, with the focal adhesion and actin filament oriented parallel to the grooves.
Corneal epithelial cells	Nanoridges with spacings of 400 to 4000 nm (*30*)	Cells align and migrate along all the ridges and grooves.
	Nanoridges with spacings of 20 to 200 nm (*34*)	In the presence of serum, the focal adhesions align along the nanoridges. The width of the focal adhesion depends on the width of the ridges.
Endothelial cells	Oriented collagen fibrils (*36*)	Cell migration along the fibrils is induced without chemoattractant.
Smooth muscle cells (SMCs)	Aligned copolymer nanofibers that are 500 nm thick (*40*)	SMCs adhere and migrate along the axis of aligned nanofibers. The distribution of cytoskeleton proteins inside the SMCs is parallel to the nanofibers.
Osteoblast-like cells	Carbon-nanotube-composed microlanes that are 9 to 76 μm wide and 4 μm high (*38*)	Cells exhibit maximum alignment of 55 % to the microlanes that are 10 to15 μm wide.

1.3. Actin polymerization

Actin is a 42-kDa, globular, multi-functional protein that is found in all eukaryotic cells. It is one of the three major components of the cytoskeleton, and is responsible for controlling cell shape, morphology and motility. A cell's ability to undergo dynamic shape change and migration results from the dynamic nature of intracellular actin polymerization. Actin monomers can polymerize into right-handed helical filaments, known as F-actin. In contrast to other biopolymers such as DNA, the backbone of which is formed through covalent bonding, F-actin is assembled through a weak interaction between actin monomers. This weak interaction facilitates the remodeling of actin and contributes to its dynamic nature. F-actin exhibits polarity, which is characterized by a fast-growing barbed end and a slow-growing pointed end. In the physiological or biological context, actin polymerization is coupled to ATP hydrolysis and comprises four cyclic steps (*41*): (i) addition of ATP-G-actin at the barbed end; (ii) conversion of ATP-actin to ADP-actin through slow hydrolysis; (iii) release of ADP-G-actin from the pointed end through depolymerization; and (iv) conversion of ADP-G-actin to ATP-G-actin in the cytoplasm, replenishing the reservoir with reactive actin monomers. When the polymerization rate at the barbed end equals the depolymerization rate at the pointed end, the F-actin reaches a steady state whereby the filament moves forward with a constant length. Such a steady state is called "treadmilling." It has been shown that the rate of barbed end growth equals the speed of lamellipodia extension (*42*), providing direct support for actin polymerization as the driving force for cell migration.

Because the actin polymerization rate *in vivo* is 100 to 200 times faster than the pure actin polymerization rate *in vitro*, regulatory proteins must be involved in the acceleration of the process. Figure 1.3A is a schematic showing the actin polymerization machinery that generates protrusions at the cell's leading edge with regulatory proteins. Among all of the regulatory proteins, Arp2/3 complex is a crucial element in the formation of the dendritic actin network observed in lamellipodia (Figure 1.3B). As an actin nucleation factor that promotes the branching of F-actin, Arp2/3 has been shown to bias the formation of a daughter filament on the convex face of a curved mother filament at an angle of 70° (*43*). Another recent study has found that T cells tend to migrate along the concave surfaces of sinusoidal wavy structures, and that inhibiting the Arp2/3 complex abolishes this preference (*44*). Both of these studies indicate that regulatory proteins involved in the actin polymerization machinery may be sensitive to curvature and shapes, and thus could bias the actin polymerization involved in contact guidance.

As a highly dynamics process, actin polymerization has been found to exhibit wave-like characteristics. For instance, Gerisch and coworkers observed actin waves in *D. discoideum* cells that were recovering from Latrunculin-induced actin depolymerization (Figure 1.3C) (*45*). Orion and coworkers found that the leading edge of a neutrophil contains moving waves of Hem-1, an actin nucleation activator (*46*). Recent reports of the self-organized traveling actin waves in *D. discoideum (45, 47, 48)* and neutrophils (*46*) provide insight into the influence of substrate topography on the propagation of actin polymerization. Bretschneider and coworkers showed that actin and its associated proteins are recruited from the cytoplasm to form distinct

three-dimensional patterns in actin waves, indicating that the propagation of actin waves is based on the activation and inactivation of actin polymerization in a defined temporal and spatial pattern (*49*). As the actin waves couple to a substrate composed of three-dimensional, asymmetric nanotopography with a temporal periodicity, it is possible that the asymmetric topography reorganizes and biases the actin waves, leading to unidirectional cell migration (see Chapter 4).

F-actin is a chiral molecule (*50*). Like other biopolymers with a helical structure, such as DNA and collagen, F-actin tends to form a superhelix or a super coil upon bending, to relax the accumulated torsional strain. It has been demonstrated that *Listeria monocytogenes* forms consistent right-handed helical actin comet tails during actin-based motility in cell-free extracts (Figure 1.3D) (*51*). Therefore, it is reasonable to propose that bending the actin waves in a particular direction, or preventing the formation of helical waves with confinement, may bias the actin polymerization waves unidirectionally, and thus lead to unidirectional cell motion (see Chapter 5).

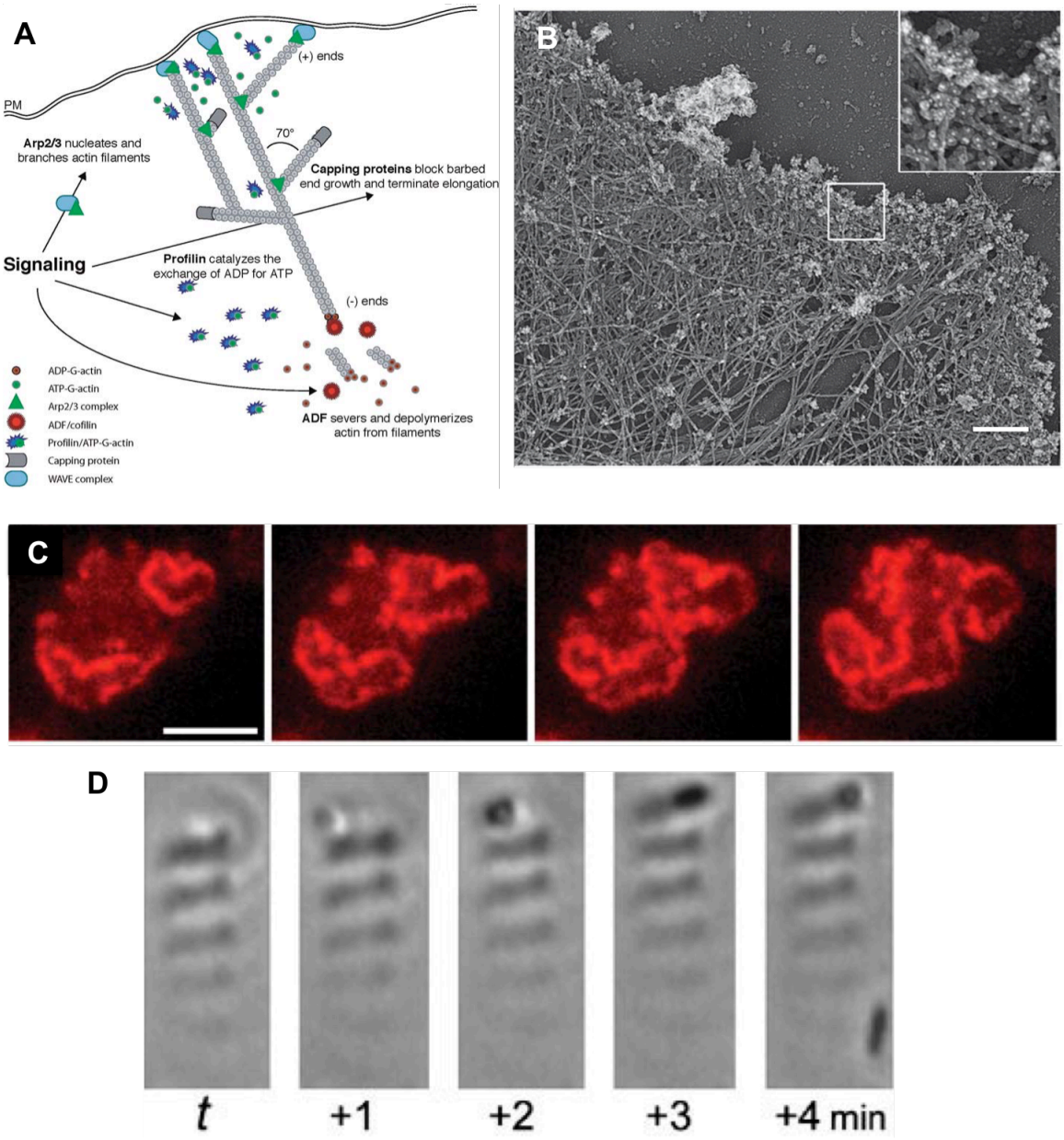

Figure 1.3. (A) Schematic representation of the actin polymerization machinery that triggers dendritic nucleation for protrusion at the leading edge (*41*). (B) Electron micrograph of the dendritic actin network inside a lamellipodium (*52*). Scale bar, 300 nm. (C) Actin wave dynamics in *D. discoideum* on a 2D surface (*45*). Scale bar, 5 μm. (D) Right-handed actin comet tail formed by *Listeria monocytogenes* in a cell-free extract (*51*).

1.4. Model systems: Dictyostelium discoideum and neutrophils

In this thesis, I present the results of the studies of the migration of and actin polymerization waves in *D. discoideum* and neutrophil-like HL-60 cells on various nanotopographies. These cell types are both the model systems for studying amoeboid cell migration. The actin polymerization machinery is conserved between *D. discoideum* and neutrophils. However, *D. discoideum* migrates by extending pseudopodia that can be microns above the surface, whereas neutrophils migrate by extending flat, fan-like lamellipodia that flow along the surface. Although the molecules involved in the adhesion of *D. discoideum* to the substrate are not well characterized, the adhesion is commonly considered to be non-specific. A previous study in our group showed that *D. discoideum* is able to adhere and migrate on surfaces with different properties, such as glass and surfaces coated with poly-l-lysine, and that *D. discoideum* even migrates normally on surfaces coated with bovine serum albumin and perfluorocarbon, which are known for their anti-adhesive properties (*53*). In contrast, neutrophils adhere specifically to fibronectin- or collagen-coated surfaces through the integrin-based focal adhesions. Therefore, in this thesis work, *D. discoideum* was studied on pure polyacrylate surfaces; neutrophils were studied on polyacrylate surfaces coated uniformly with fibronectin.

D. discoideum is an amoeba that lives in the soil. It can transform from individual cells to a multicellular slug, and eventually to a fruiting body with spores (*54*). The lifecycle of *D. discoideum* is shown in Figure 1.4. When food, such as bacteria, is sufficient, *D. discoideum* cells stay in the vegetative stage and chemotax up the gradient of a bacterial metabolic product, folic acid. When food is deficient,

the cells undergo aggregation by secreting and sensing a chemoattractant called cyclic adenosine monophosphate (cAMP), and by forming head-to-tail cell streams through signal relay. Large cell aggregates then transform into slugs, and eventually differentiate into spore and stalk cells (*54*). *D. discoideum* cells in the aggregated stage undergo differentiation and exhibit the most active migration capability, and are thus widely used as a model system to study cell migration. During differentiation, cyclic AMP is synthesized intracellularly via an enzyme called adenyl cyclase A (encoded in gene *aca*) and is secreted in pulses every ~ 6 min. Cells move up the gradient of cAMP concentration at an average speed of 10 μm/min for ~ 60 s and then stop until the next secretion occurs. In my experiments, a mutant with the *aca* gene knocked out (aca^-) was used to eliminate the influence of a gradient of cAMP concentration on cell directionality (*8*). Aca^- *D. discoideum* does not secret cAMP, but still senses it. To induce differentiation, cells were starved and pulsed with cAMP every 6 min for 5 h. *D. discoideum* cells with the *aca* gene intact were also used in my experiments. Because caffeine has been found to inhibit the activation of adenyl cyclase A without affecting the cell viability (*55*), those cells were incubated with caffeine to eliminate cAMP secretion (see Section 4.4.2).

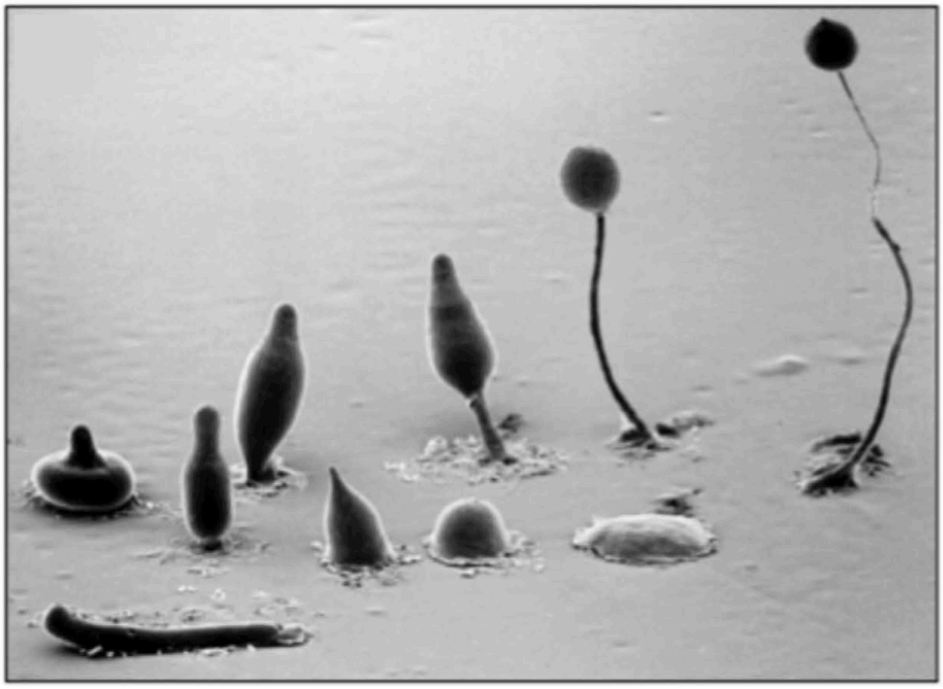

Figure 1.4. Lifecycle of *Dictyostelium discoideum.* When starved, *D. discoideum* aggregate to form slugs, which further differentiate into a fruiting body with a stalk and a spore. (Image Copyright, M. J. Grimson & R. L. Blanton, Biological Sciences Electron Microscopy Laboratory, Texas Tech University)

To visualize actin polymerization waves in *D. discoideum,* two types of mutant with labeled F-actin, LimEΔcoil-GFP (*56*) and Lifeact-TagRFP (*57*), were used in my experiments. LimE is a LIM-domain containing protein that is strongly recruited to polymerizing actin. The coiled-coil domain of LimE is not required for F-actin binding, and thus has been eliminated in our construct to reduce the steric hindrance during F-actin binding (*56*). Lifeact is a 17-amino-acid peptide that binds to F-actin with low affinity. This low binding affinity minimizes the effect of Lifeact-RFP

expression on actin polymerization, and helps to reveal the intrinsic dynamics of actin waves (*57*).

Neutrophils are the most abundant white blood cells in mammals and belong to the fastest migrating class of mammalian cells. These cells establish a polarized shape upon the stimulation with chemoattractant by forming broad lamellipodia in the front and a contracted uropod at the rear. Cell-level actin reorganization is involved in the polarization process. Because neutrophils are short-lived, terminally differentiated cells, genetic manipulation of these cells is difficult. Dimethylsulfoxide (DMSO) can be used to induce HL-60 cells to differentiate into neutrophil-like cells. It has been shown that the motile properties of neutrophil-like HL-60 cells are comparable to those of primary neutrophils (*58*). Therefore, actin-YFP, neutrophil-like HL-60 cells were employed in this thesis work.

1.5. Thesis outline

To investigate contact guidance exerted by topographies that mimic the features observed in the natural ECM, it is necessary to fabricate intricate structures on a subcellular length scale and to ensure biocompatibility of the topographies. Although micro- and nano-fabrication methods, such as multiphoton absorption polymerization (MAP), are able to fulfill this task, they are inherently serial voxel-by-voxel processes. Whitesides and coworkers developed a method called soft lithography to mold nanostructures using polydimethylsiloxane (PDMS) (*59*), but the resolution of molding high-aspect-ratio and dense structures is 500 nm. Based on a published method (*60*), we developed an approach called solvent-assisted nanotransfer molding

(nTM) towards mass production of MAP-fabricated nanotopographies with a resolution of approximately 30 nm. The key point of this approach is to reduce the viscosity of the hard-PDMS prepolymer by adding a fluidic solvent. The replica can be functionalized with various proteins. The functionality of the replica can be tuned by adjusting the UV curing time. Details of solvent-assisted nTM are described in Chapter 2.

Because linear collagen fibers on a length scale of hundreds of nanometers are the typical structures observed in the ECM, it is worthwhile to study the effect of nanoridges and nanogrooves on cell motion and actin-wave propagation. Chapter 3 describes the bidirectional guidance of nanoridges and nanogrooves on actin waves in *D. discoideum*, and discusses the effect of ridge frequency and gap width on actin-wave dynamics. Helical actin waves are observed on nanoridges that are spaced 1.5 to 2 μm apart. The transition between static and traveling actin waves observed on nanodots connected with nanoridges is also discussed.

Inspired by the bidirectional guidance of cell motion and actin waves that we observed on symmetric nanoridges, we investigated cell motion and actin waves on ridges composed of asymmetric nanosawteeth, aiming to bias the actin polymerization dynamics through the imposed asymmetric nanotopography, and eventually promote unidirectional cell motion. Chapter 4 focuses on the unidirectional guidance observed in both *D. discoideum* and neutrophil-like HL-60 cells in detail. We find that the preferred direction of actin-wave propagation is consistent with that of cell motion, and that the biased direction depends on the

details of the nanotopography. Separated nanosawteeth guide actin waves unidirectionally, but not cell motion.

Concentric nanorings were used to investigate the effect of bending on the direction of actin polymerization. Because we observed that the formation of helical actin waves depends on the gap width between adjacent ridges, we studied cell motion and actin-wave propagation on nanorings with different spacings and heights. Bending a helical actin wave will cause the helix to twist or untwist, and thus lead to an enhanced or reduced actin polymerization that depends on the traveling direction of the wave. The effect of both ring spacing and ring height on actin-wave propagation, cell motion, and cell polarization, are elaborated in Chapter 5.

Chapter 6 summarizes each project that has been discussed, and suggests future directions for this research.

Chapter 2: Fabrication of Nanotopographies Using Multiphoton Absorption Polymerization and High-Resolution Solvent-Assisted Nanotransfer Molding

2.1. Introduction

To study cellular contact guidance of nanotopographies, a fabrication technique that achieves nano-scale resolution is needed. Multiphoton absorption polymerization (MAP) is one such method. MAP has several advantages compared to other popular nanofabrication methods, such as e-beam lithography and dip-pen nanolithography, for example. First, MAP is capable of fabricating arbitrary 3D structures due to its voxel-by-voxel based approach. Also, the MAP process is insensitive to the environmental conditions (compared with the high vacuum required in e-beam lithography and rigorous humidity control in dip-pen nanolithography). Therefore, MAP offers great reproducibility and stability. Previous work in our group has demonstrated that 40-nm resolution can be achieved using a variation of MAP called resolution augmentation through photo-induced deactivation (RAPID) (*61*). However, MAP is inherently a serial voxel-by-voxel process. An intricate structure may take hours to fabricate. Therefore, the application of MAP in rapid mass production is limited.

Efforts have been made to address the time-intensive, serial nature of MAP. Two pioneering methods in this area are multipoint fabrication and multibeam interference

lithography. Kawata and coworkers demonstrated the first technique by placing a microlens array in the beam path before the objective, subdividing the laser beam into hundreds of focal points that can be used for MAP fabrication (*62, 63*). In the second technique, three or more laser beams are employed to create a complex 3D interference pattern, which is then used to expose to the photoresist (*64-66*). Although these techniques are capable of scaling up production, some drawbacks remain: (i) An amplified laser has to be employed to deliver enough power to each focal point; (ii) Uniformity in the intensity across the microlens array must be ensured to fabricate identical structures; and (iii) Only periodic arrayed features can be fabricated. To fabricate arbitrary 3D structures, other techniques are required.

Microtransfer molding (μTM) based on soft lithography opens the door to rapidly replicating complex 3D structures in a parallel manner (*59, 67*). In this method, a master structure is fabricated through the serial process. An elastomeric prepolymer, usually polydimethylsiloxane (PDMS), is poured on the master surface, cured, and peeled off. A resin is then sandwiched between the elastomeric mold and a new substrate. When the resin is cured, the mold is peeled away. The structures on the new substrate will be identical to the original master. Multiple molds can be made from the same master surface, and multiple copies can be replicated from the same mold. Our group has demonstrated that intricate 3D structures with closed loops and overhangs can be replicated through a technique called membrane-assisted microtransfer molding (*68*). Although conventional soft lithography is highly efficient in replicating structures on the scale of 500 nm or larger, it is inadequate to replicate dense and high-aspect-ratio structures in the sub-500-nm range due to the low elastic

modulus of Sylgard 184 PDMS. The glass transition temperature of PDMS is far below room temperature, which allows the polymer chains between crosslinks to move and causes inelastic deformation. To improve the resolution of μTM, Schmid and Michel formulated a polymeric composite with a high modulus, referred to as hard PDMS (h-PDMS), based on vinyl and hydrosilane end-linked polymers (*69*). The low viscosity of h-PDMS prepolymer allows it to come into conformal contact with the master surface; the low surface energy of h-PDMS (22-24 $\times$ 10^{-3} J/m^2) (*70, 71*) also facilitate the release of the master surface. Using this formulation, they achieved high-density-pattern replication at the 100-nm scale. However, cutting and releasing the cured h-PDMS usully causes cracking across the surface, resulting in debris being left on the surface. Whitesides and coworkers overcame this problem by using a composite PDMS mold consisting of a thin layer of rigid h-PDMS, which allows a high-resolution molding, and a slab of flexible s-PDMS, which prevents the cracking of the h-PDMS (*72*). Later, Lee and coworkers achieved a resolution of 40 nm by adding specific solvents into the h-PDMS prepolymer to lower the viscosity and improve the wettability, thus facilitating the penetration of h-PDMS into the voids (*60*).

The solvent-assisted nanotransfer molding (nTM) method is employed in my study to replicate nanotopographies in a parallel manner. The remainder of this chapter will discuss our fabrication and replication techniques in detail.

2.2. Fabrication of master nanotopographies via multiphoton absorption polymerization

2.2.1. Principles of multiphoton absorption polymerization

In the process of MAP, n photons ($n \geq 2$) need to arrive at the same place simultaneously for the n-photon polymerization to occur. The total energy of the photons is equal to that needed to promote the electron from the ground state to the excited state. In two-photon absorption polymerization, which is employed in this study, the probability of excitation is proportional to the square of the light intensity. Due to this nonlinear intensity dependence, localization of excitation within the focal volume of a laser beam can be achieved (Figure 2.1A). An arbitrary 3D structure can then be fabricated by moving the sample stage in three dimensions (Figure 2.1B). In contrast, for single-photon absorption, the number of molecules excited is independent of the illuminated area, which results in absorption throughout the whole volume in which the light propagates (*73*) (Figure 2.1A).

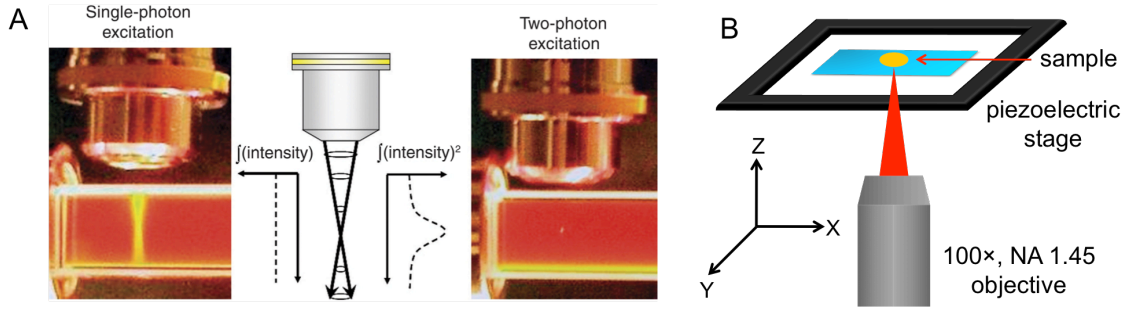

Figure 2.1. (A) Fluorescence in a rhodamine B solution excited by single-photon excitation (left) and by two-photon absorption of a mode-locked Ti:sapphire laser tuned to 800 nm (right) (*73*). (B) Schematic of the sample setup.

2.2.2. Experimental details

Coverslips were exposed to oxygen plasma (Harrick, PDC-32G) for 3 min and then functionalized with (3-acryloxypropyl)trimethoxysilane (SIA0200.0, Gelest) to enhance the adhesion of fabricated structures to the surface. Acrylic resin was prepared by mixing 49 wt% tris (2-hydroxyethyl) isocyanurate triacrylate (SR368, Sartomer) (Figure 2.2A), 49 wt% dipentaerythritol pentaacrylate (SR399, Sartomer) (Figure 2.2B) and 2 wt% Lucirin TPO-L (2,4,6-trimethylbenzoylethoxyphenylphosphine oxide, photoinitiator). Dipentaerythritol pentaacrylate tends to shrink upon polymerization. The shrinkage was used to fabricate finer features. One drop of acrylic resin was sandwiched between two coverslips, with two pieces of tape used between the coverslips as spacers. The sample was then mounted on a piezoelectric stage for 3D fabrication.

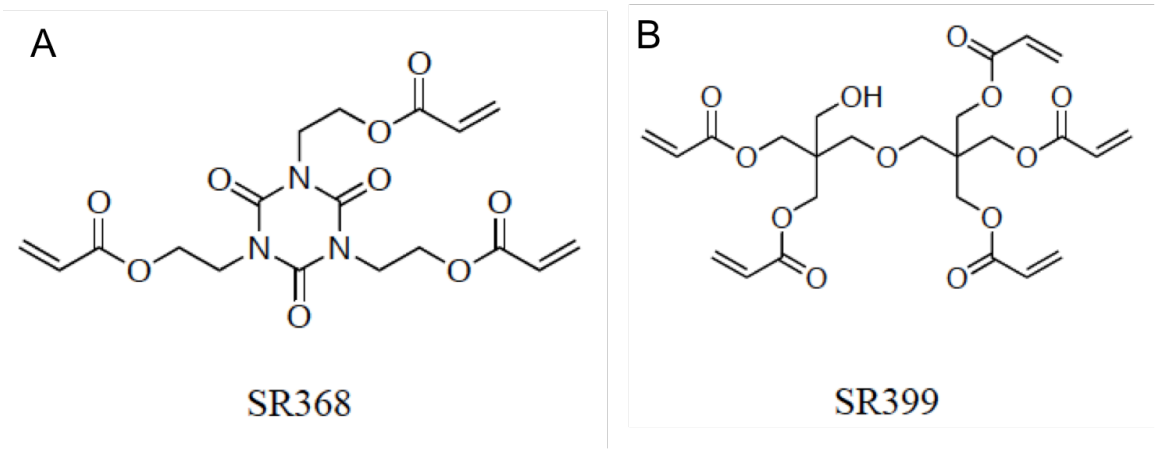

Figure 2.2. Chemical structures of (A) SR368 and (B) SR399.

A commercial Ti:sapphire laser (Coherent Mira 900 F) with a repetition rate of 80 MHz and a pulse duration of approximately 100 fs was employed as the excitation source. The laser was tuned to 800 nm and the beam was transmitted through a 100×, 1.45 NA, oil-immersion objective on an inverted microscope (Zeiss Axiovert 135). The average power for fabrication was 3 to 5 mW, as measured at the sample. The master nanotopographies were fabricated by moving the sample in three dimensions via a piezoelectric stage that was controlled by a LabVIEW program. The fabrication process was monitored in real time.

After fabrication, the master structures were developed in dimethyl formamide and ethanol. The substrate was then dipped in hexane to prevent structural collapse due to surface tension and baked at 90 °C to harden the structures.

2.3. High-resolution solvent-assisted nanotransfer molding

The master surfaces were functionalized with primary amines using a mixture of ethylenediamine (E26266, Sigma-Aldrich) and ethanol (1:4, V/V) for 30 min, and then were treated with a solution containing 0.03 g of perfluorooctadecanoic acid (L16837, Alfa Aesar), 4.5 g of hexafluorobenzene (H8706, Sigma-Aldrich), 16 mL of ethanol and 50 μL of methanol for 1 h to minimize the surface energy, facilitating the release of cured PDMS. To prepare h-PDMS, hexane was selected as the solvent, not only because of its low viscosity, high volatility and high solubility in PDMS (*74*), but also because its nonpolar nature would enhance the wettability on the hydrophobic surface. 1.7 g of vinyl PDMS prepolymer (VDT-731, Gelest), 9 μL of Pt catalyst (SIP6831.2, Gelest), 0.05 g of modulator (87927, Sigma-Aldrich), 0.5 g of hydrosilane (HMS-301, Gelest) and 1 g of hexane were mixed. The mixture was spin-coated on the master surface (1000 rpm, 40s), allowed to sit at room temperature for 2 h, and then baked at 60 °C for 1 h. Soft PDMS (s-PDMS) was prepared by mixing the base and curing agent (Sylgard 184, Dow Corning) in a 10:1 mass ratio. After degassing, the uncured s-PDMS was poured onto the precured h-PDMS and baked at 60 °C for 1 h. After curing, the composite PDMS was peeled off of the master surface (Figure 2.3). For the nanoridges and nanosawteeth that will be discussed in the following chapters, the peeling direction was along the lines and the slants with increasing height, respectively.

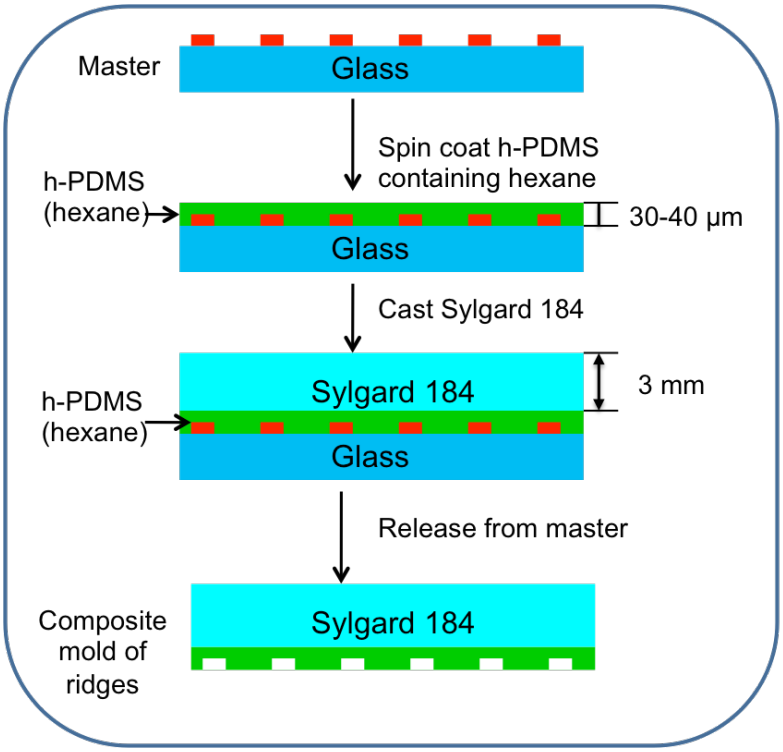

Figure 2.3. Flow chart of the solvent-assisted nanotransfer molding of nanoridges.

Replicas were created by sandwiching a drop of acrylic resin between the mold and an acrylate-functionalized coverslip and then UV curing (Blak-Ray, B-100AP, 100 W, 365 nm, samples were placed 254 mm from the source). The resin for making replicas was composed of 49 wt% tris (2-hydroxyethyl) isocyanurate triacrylate (SR368, Sartomer), 49 wt% ethoxylated (6) trimethylolpropane triacrylate (SR499, Sartomer) (Figure 2.4) and 2 wt% Lucirin TPO-L. This formulation exhibits little shrinkage, and thus can replicate the nanotopographies with high fidelity. Replicas were UV cured either for 5 min or 50 s, depending on the subsequent application.

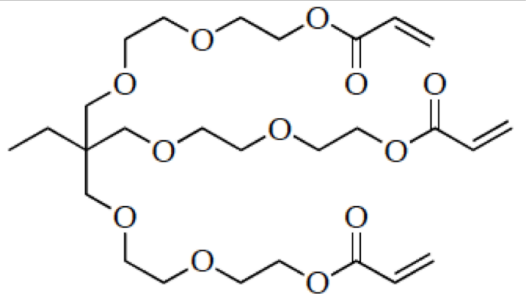

SR499

Figure 2.4. Chemical structure of SR499.

Nanogrooves (the negative of nanoridges) were prepared using a double-molding process, in which the mold of the nanoridges was treated as a master (Figure 2.5). The mold was exposed to oxygen plasma for 30 s and coated with (tridecafluoro-1,1,2,2,-tetrahydrooctyl)methyldichlorosilane (SIT8172.0, Gelest) in a dessicator to facilitate the release of PDMS. The master was then molded and replicated with the aforementioned method.

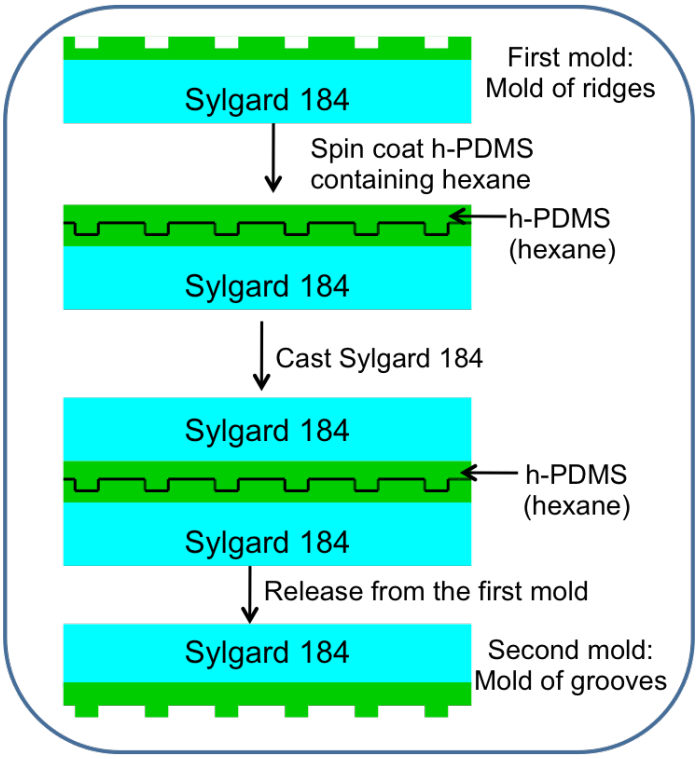

Figure 2.5. Flowchart of the replication of nanogrooves through double-molding process.

2.4. Surface coating with proteins

The surfaces for studying cell migration need to be pretreated to ensure biocompatibility for various cell types. All surfaces were immersed in ethanol for at least 5 h to allow the toxic residual photoinitiator and its by-products to diffuse out. Because *D. discoideum* adheres to the surface non-specifically, the surfaces for *D. discoideum* were UV-cured for 5 min without special coating. However, neutrophils migrate by forming focal adhesion complexes on the surfaces, so it is necessary to coat the surfaces with fibronectin or collagen. Surfaces for neutrophils were UV-

cured for 50 s. This shorter curing time renders the acrylic resin only partially cross-linked, which provides the residual vinyl groups needed to react with amine groups on the proteins through Michael addition. The surfaces were coated with 1 μg/mL fibronectin in Hank's balanced salt solution (HBSS) (F1141, Sigma-Aldrich; Hilyte Fluor 488 labeled fibronectin: FNR02-A, Cytoskeleton) at 37 °C for 1 h and washed with HBSS.

2.5. Results and Discussion

2.5.1. Characterization of nanotransfer-molded topographies

Both master and replica of nanoridges were coated with Pt/Pd and characterized by scanning electron microscopy. The nanoridges were faithfully reproduced (Figure 2.6), although the ridges on the replica are usually a few nanometers wider than those on the master (cf. Figures 2.6A and B), presumably due to the shrinkage of PDMS upon curing. Another factor that may contribute to the small deviation—which approaches the size of a large molecule—is the anti-adhesion perfluorocarbon coating on the master surface. The perfluorocarbon coating not only lowers the surface energy, but also introduces steric hindrance on the wetting of the master surface by h-PDMS prepolymer. To improve the resolution further, a different perfluorocarboxylic acid with a shorter chain length could be used, provided that the resultant surface energy is still low enough to prevent the h-PDMS from sticking to the master surface.

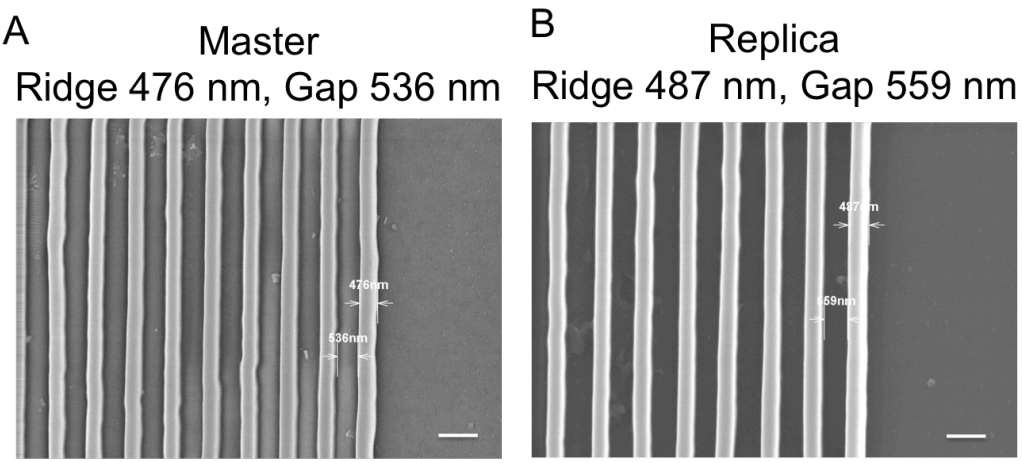

Figure 2.6. Scanning electron micrographs of master (A) and replica (B) of nanoridges. Scale bar, 1 μm.

Besides nanoridges, other nanotopographies, such as sawteeth, rings and dots, were also molded with high fidelity (Figure 2.7).

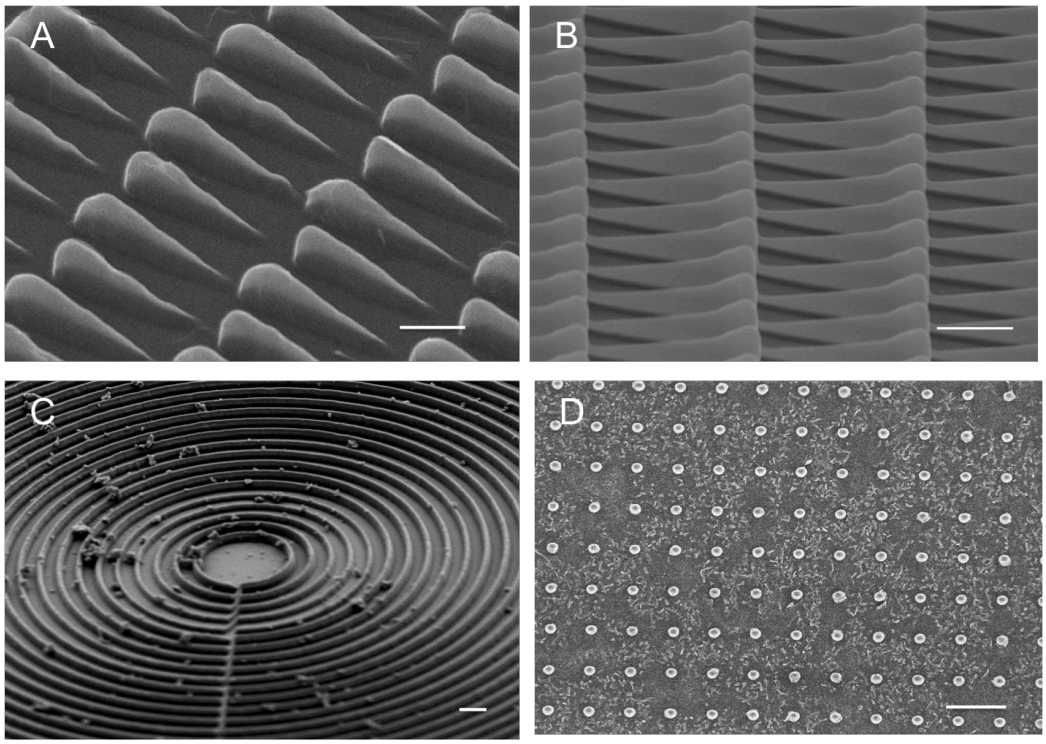

Figure 2.7. Scanning electron micrographs of (A,B) nanosawteeth, (C) concentric rings and (D) nanodots. Scale bars, (A) 1 μm, (B-D) 3 μm.

2.5.2. Characterization of nanogrooves molded through a double-molding process

The nanogrooves are more than 100 nm wider than the nanoridges replicated from the same master (cf. Figures 2.8A and 2.8B). One reasonable explanation for this effect is that the hexane in the h-PDMS prepolymer involved in the double-molding process may cause the first mold to swell and lengthen in every dimension.

This problem may be alleviated by replacing the 1 g of hexane in the h-PDMS prepolymer with a mixture of hexane and a poor PDMS solvent, such as ethanol, because a mixture of a good and poor PDMS solvent is known to reduce the swelling effect (*74*). On the other hand, in the double molding process, the anti-adhesion surface treatment of the first mold was carried out via vapor-phase deposition through the reaction between the fluorosilane and the oxidized PDMS. Because the fluorosilane is highly sensitive to water, moisture-induced copolymerization may occur, which leads to surface roughening and inhomogeneous coating (*75*). The roughened surface and coating inhomogeneity may prevent the h-PDMS prepolymer from accurately conforming to the intrinsic nanotopographies, and thus result in an enlarged complementary nanotopography on the second mold.

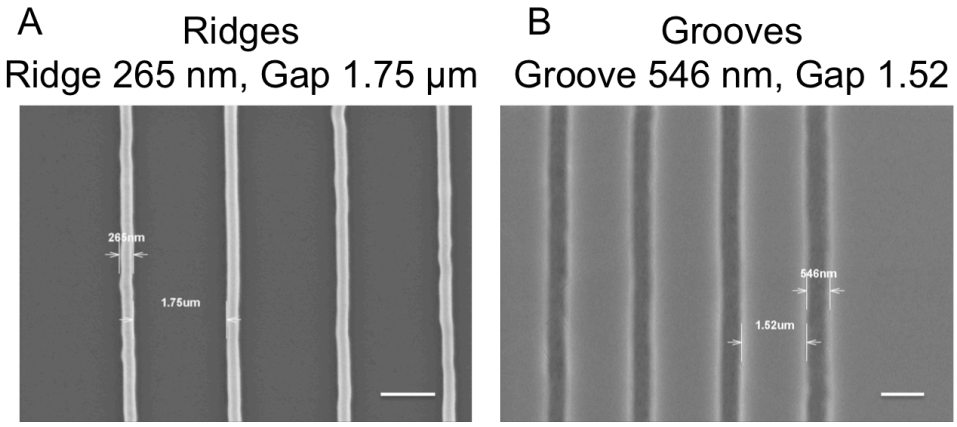

Figure 2.8. Scanning electron micrographs of molded nanoridges (A) and molded nanogrooves (B). Scale bars, 1 μm.

2.5.3. Resolution of solvent-assisted nTM

Nanotransfer molding using composite PDMS provides a practical route to replicating sub-50-nm (*76*) and even sub-10-nm features (*77-80*) in a parallel manner. Whitesides and coworkers have demonstrated the molding of 50-nm horizontal (*76*) and 2-nm vertical features (*77*). Rogers and coworkers extended both the horizontal and vertical resolution to less than 2 nm in the molding of single-walled carbon nanotubes attached to a substrate (*78, 79*). Replication of molecular-scale features (Ångstrom) has also been demonstrated by Whitesides and coworkers in the molding of regular arrays of single molecular-height steps on the faces of ionic crystals (*80*). Despite the established high resolution, the features that were used in these studies either distribute sparsely on the substrate or have a low aspect ratio (height:width < 1:5).

To investigate whether nTM could faithfully replicate dense nanotopographies with a relatively higher aspect ratio (height:width = 2:3), I fabricated a master surface composed of 250-nm-wide ridges spaced by 150-nm-wide grooves (pitch 0.4 μm). The AFM images in Figure 2.9 show that the width of the ridges is mostly reproduced, whereas the height of the ridges on the replica is slightly shorter than that of ridges on the master surface (cf. Figures 2.9A and B).

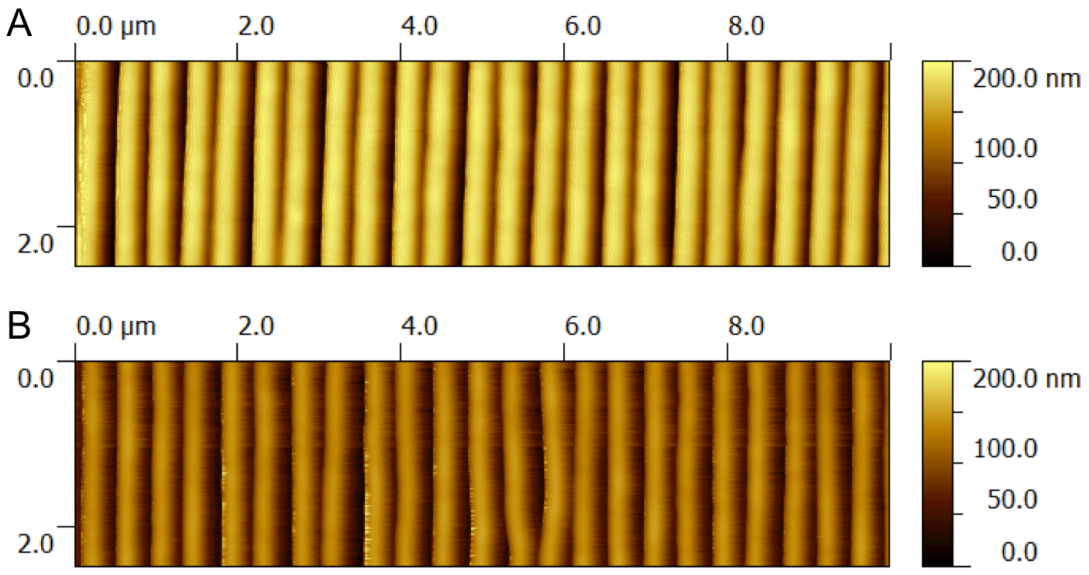

Figure 2.9. Atomic force micrographs of the master (A) and replica (B) of 0.4-µm-spaced nanoridges.

For further assessment of the nTM resolution, it would be desirable to mold even smaller and denser features. However, the width of a voxel fabricated with MAP is 200 to 300 nm. Therefore, MAP-fabricated nanoridges with a pitch smaller than 0.4 µm would be indistinguishable due to overlap with the adjacent ridges. As an alternative, nanograss created by treating nanoridges with reactive ion etching (RIE) was used to investigate the nTM resolution. In RIE, a plasma is created between two electrodes. Ions that chemically react with the sample are accelerated in an electric field, delivered vertically, and bombarded onto the sample, leading to anisotropic etching. To create nanograss by treating the molded nanoridges with RIE, we used a gas mixture of O_2 (5 sccm) and CHF_3 (15 sccm), with a radio frequency (RF) of 150

W, a pressure of 50 mTorr, and an etching time of 10 minutes. Because the surface of the nanograss is already coated with fluorocarbon through RIE, no anti-adhesion treatment is needed before the nTM. As shown in Figures 2.10A and B, nanograss created by RIE has a thickness of approximately 25 nm and a spacing of approximately 25 nm. In contrast, the molded nanograss appears thicker and the blocks connect to one another (Figures 2.10C and D). It is worth noting that nanoparticles with a diameter of 20-30 nm were created through RIE. Although some details of nanograss were lost in nTM, the shapes of nanoparticles were retained, presumably due to the low aspect ratio.

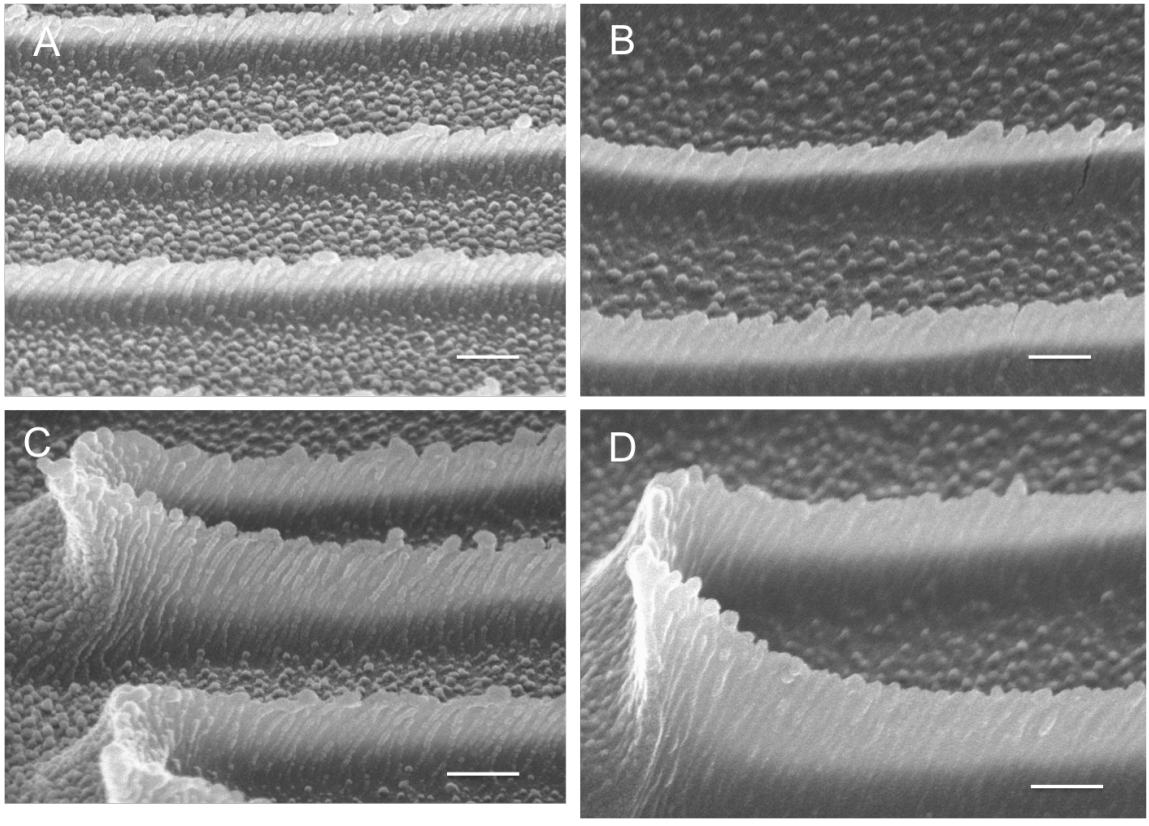

Figure 2.10. Scanning electron micrographs of the master (A,C) and replica (B,D) of RIE-treated nanoridges. Scale bars, 200 nm.

The theoretical limit of nTM is determined by the average chemical bond length and distance between crosslinks in h-PDMS (*78*), as well as by the molecular organization and interaction between the master and h-PDMS surfaces (*80*). In all the nTM experiments we performed, the master surfaces were coated with fluorocarbon to lower the surface energy and facilitate the release of the composite mold. However, a low-energy surface is associated with a low wettability, which prevents the h-PDMS prepolymer from perfectly conforming to the nanotopographies. One possible solution is adding a solvent into the h-PDMS prepolymer to reduce the surface tension of the mixture. Zisman has found that on a low-energy surface, cos θ (θ is the angle of contact) increases linearly as the surface tension of the liquid decreases (*81, 82*). For our nTM process, perfluorohexane is a promising solvent due to its low surface tension (γ = 11.91 mN/m at 20 °C, compare this, for example, with hexane for which γ = 18.43 mN/m at 20 °C) and low viscosity (0.67 cp at 25 °C). The molecular similarity between perfluorohexane and the perfluorocarbon coating on the master surface is also conducive to the conformal contact. Additionally, when the features to be molded are only an order of magnitude larger than the molecular scale—such as nanograss—the thickness of the anti-adhesion coating needs to be considered due to its influence on conformability. As discussed in Section 2.4.1, a perfluorocarboxylic acid with a shorter chain length could be used instead.

Some other processing conditions can also be adjusted to improve the nTM resolution. Rogers and coworkers have found that the resolution and crosslink density of the h-PDMS are correlated, and that the resolution and roughness are related (*78*). Therefore, we can further tune the formulation and curing temperature of h-PDMS

towards a higher crosslink density and resolution. Separating the replica from the PDMS stamp while the two are immersed in liquid has also been shown to decrease the surface roughness (*77*). Spin-casting h-PDMS prepolymer at a higher speed and pre-curing it under vacuum may improve the conformability. All of these processing conditions are worth further investigation.

2.5.4. Coating nanotopographies with protein

Nanosawteeth were replicated through solvent-assisted nTM with UV curing for 50 s. The surface was coated with HiLyt-488-labeled fibronectin as described in Section 2.3. A Leica SP5X laser scanning confocal microscope was used to image the fluorescent-fibronectin-coated nanotopographies. Figure 2.11A shows the maximum-intensity projection of the z-stack images of the coated surface obtained using the ImageJ software package (NIH) (*83*). The uniform fluorescence intensity indicates a uniform fibronectin coating. Live cell imaging shows that neutrophils elongate and migrate unidirectionally along the nanosawteeth, which will be discussed in detail in Chapter 4. Figures 2.11B and D are the bright-field micrographs of a fixed neutrophil on nanosawteeth (Figure 2.11B) and a flat surface (Figure 2.11D). The cells spread on the surface and exhibit polarized morphology. Paxillin, which is a focal-adhesion-associated protein, was fluorescently stained in the fixed neutrophils. The presence of focal adhesions further confirms that the surface was coated with fibronectin (Figures 2.11C and E). Because the coating is accomplished through the Michael addition reaction between the vinyl groups on the surface and the amine groups in the protein,

this method can be broadly applied to any type of protein to be coated onto the surface.

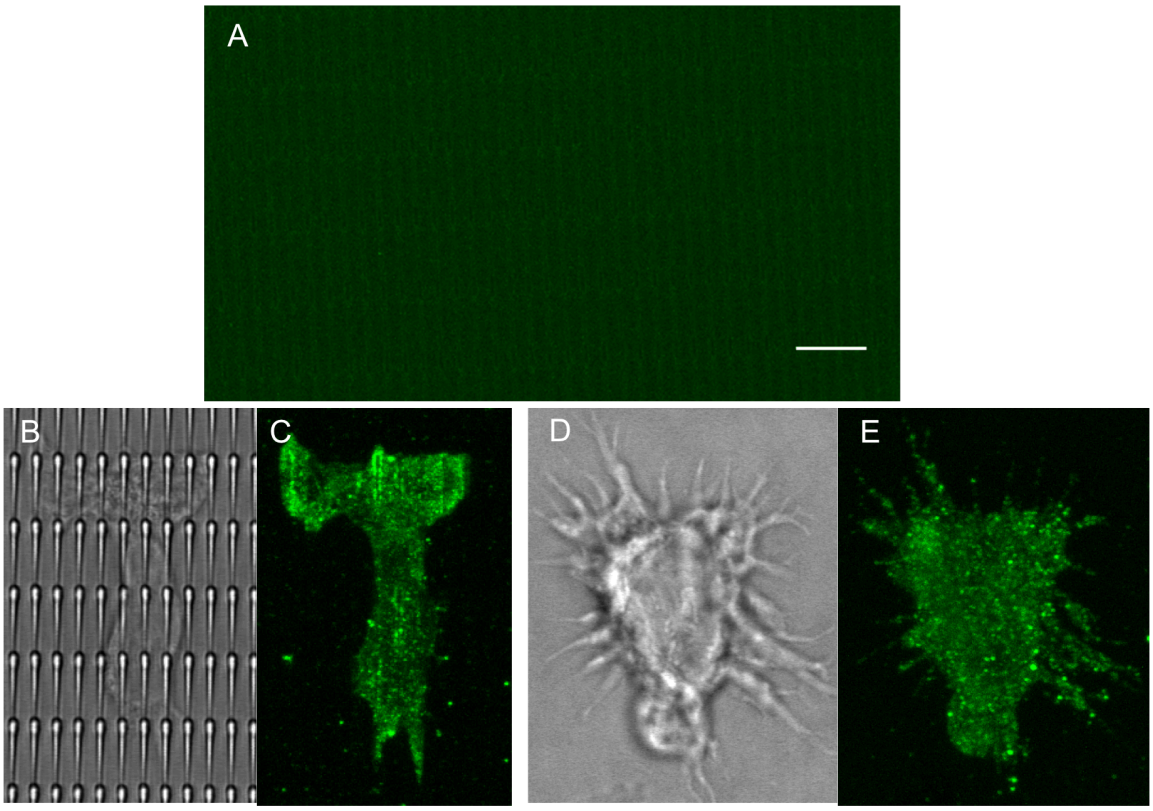

Figure 2.11. (A) Maximum-intensity projection of z-stack images of fluorescent-fibronectin-coated nanosawteeth. Scale bar, 8 μm. Bright-field micrographs of neutrophils on fibronectin-coated nanosawteeth (B) and flat surface (D). (C),(E) Maximum intensity projection of the same cells with paxillin stained.

Previous work in our group (unpublished) has demonstrated that perfluorocarbon-coated nanoridges trap air in the gaps when the surface is immersed

in water. Therefore, differential protein coating on the nanoscale may be achieved by coating the nanoridges with hydrophobic molecules (such as a hydrocarbon with a long chain length). Due to the hydrophobicity of the coated surface and the surface tension of water, water molecules will be prevented from penetrating into the gaps. If the surface is immersed in a protein solution, then the protein is only allowed to touch the tops of the nanoridges. Through the interaction between the hydrocarbon on the surface and lipophilic domain of the protein, differential protein coating on top of nanoridges could be accomplished in principle. This nanoscale differential coating could be one of our future directions.

2.6. Summary

Nanotopographies fabricated with MAP can be faithfully replicated using solvent-assisted nTM in a parallel manner. Adding solvent into the h-PDMS prepolymer to reduce the viscosity improves the conformability, leading to a higher molding fidelity. nTM is capable of replicating diverse nanotopographies, such as ridges, grooves, rings, sawteeth and dots. The molding resolution depends on the aspect ratio and density of the master structures. For dense structures with a high aspect ratio, such as nanograss, the molding resolution is larger than 30 nm. The functionality of the replica for protein coating can be manipulated by tuning the UV-curing period. Neutrophils plated on a fibronectin-coated nanosawteeth have been shown to form focal adhesions and migrate on these surfaces. Solvent-assisted nTM and surface coating with proteins open the door to mass production of biocompatible

and biofunctional surfaces with nanotopographies, which provide a versatile platform for studying various biological problems.

Chapter 3: Bidirectional Contact Guidance of Actin Waves through Dynamic Sensing of Nanoridges/Nanogrooves

Section 3.2.1. is adapted from M. K. Driscoll, X. Sun, C. Guven, J. T. Fourkas, W. Losert, Cellular Contact Guidance through Dynamic Sensing of Nanotopography. ACS Nano 8, 3546-3555 (2014). Driscoll and Guven developed the analysis tools. Sun carried out nanofabrication and cell experiments.

3.1. Introduction

In natural biological systems, cells are not only guided by chemoattractants, but also by the micro- and nano-scale topographies of the extracellular matrix (ECM), such as collagen fibers and a fibronectin meshwork. The length scale of these topographies ranges from microns for collagen fibers down to 3 nm for surface adhesion molecules. With the advent of new methods in nanofabrication, various topographies mimicking the length scale of the ECM have been fabricated to study contact guidance. Diverse cell types, such as mesenchymal cells, epithelial cells, fibroblasts and macrophages, have been shown to elongate and align parallel to micro- and nano-gratings (*28-31, 34, 35, 84, 85*). These cell types form focal adhesion complexes with the surface, and a selective clustering of integrins on the topographical features has therefore been speculated to induce contact guidance (*34, 85*).

To investigate whether focal adhesions or any other factors are required in contact guidance, we studied the effect of nanoridges on the migration and cell shape

dynamics of the amoeba *Dictyostelium discoideum* (*D. discoideum*), which lacks focal adhesion complexes and adheres to the surface non-specifically (*86*). We observed significant contact guidance of *D. discoideum* along nanoridges. Cells that moved parallel to the nanoridges were faster, more protrusive at their fronts, and more elongated than were cells that moved perpendicular to the nanoridges. The greatest contact guidance efficiency was achieved on ridges that were spaced 1.5 μm apart; this is a comparable length scale to previously reported actin waves (*45*). Cells treated with latrunculin, which sequesters actin monomers and depolymerizes F-actin, were round and immotile on nanoridges, suggesting that actin polymerization is required for contact guidance.

Because cell polarization and migration are the direct results of actin polymerization and depolymerization, a number of previous studies have attempted to elucidate the role of actin in contact guidance. Surfaces coated with nanoparticles that are 70 nm in diameter lead to a disruption of the actin scaffolding and a loss of stress fibers in osteoblasts (*87*). F-actin aligns along micro/nanogratings (*29, 85, 88-93*), and has been proposed as the driving force for the observed contact guidance. Actin stress fibers have also been shown to align along an oriented 3D matrix (*39*). Actin waves have been shown to dissipate upon colliding with large barriers, enabling the cell to reorient and flow around the barrier (*46*). In our experiments, we used F-actin-labeled *D. discoideum* to study the effect of nanoridges/grooves on actin-wave propagation. The remainder of this chapter will discuss the dynamics, morphology and guidance efficiency of actin waves in details.

3.2. Results and Discussion

3.2.1. Actin waves are guided along nanoridges/grooves

To investigate the dynamics and morphology of actin waves on nanoridges/grooves directly (Figures 2.8A and B), we imaged LimEΔcoil-GFP cells in an AX3 background. LimE is a LIM-domain containing protein that is strongly recruited to polymerizing actin (*94, 95*). The coiled-coil domain at the C-terminal end of LimE, which is not required for F-actin binding, has been eliminated in our construct because the truncated protein exhibits a reduced cytoplasmic fluorescence background (*56*).

We found that the actin polymerization waves travel along the nanoridges. Actin appears to polymerize into linear streak-like structures on the opposite sides of a nanoridge, with each streak extending up to 500 nm away from the nanoridge. The two linear actin waves exhibit coupled dynamics (Figure 3.1A), suggesting that the actin streaks connect to each other across the top of the nanoridge. Images taken at the top of the nanoridges still show the accumulation of F-actin, confirming the linkage between the two streaks (Figure 3.1B). Therefore, actin polymerization preferentially occurs around a nanoridge, and propagates along the nanoridge as a whole. The total actin wave size around a single ridge is about 1.2 μm (the sum of the width of two actin streaks and the width of the ridge), which is similar to the reported actin wave size on a flat surface (*45*). In contrast to the coupled dynamics of actin waves on nanoridges, actin waves in nanogrooves separated by microridges are not coupled and propagate independently (Figure 3.1C). We did not observe preferential

actin polymerization on top of microridges between adjacent nanogrooves. The absence of F-actin accumulation on top of microridges suggests that the width of the ridges may affect the coupling dynamics of actin waves, and that the curvature of the ridges may affect the initial actin polymerization. Curvature has been shown to bias the location of actin branching nucleation (*43*). Therefore, the high curvature on the top of nanoridges may promote the nucleation of F-actin and enhance the coupling of actin streaks.

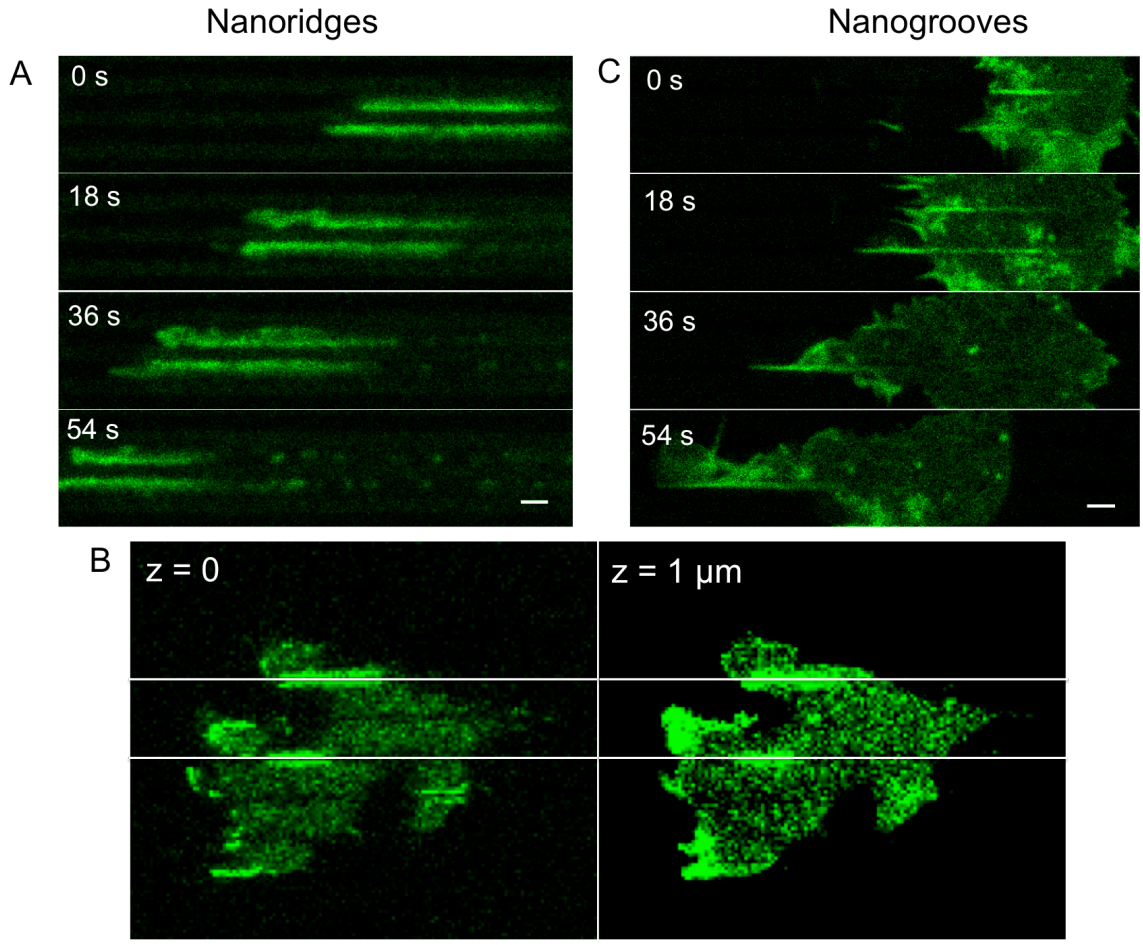

Figure 3.1. (A) Serial confocal images of coupled actin waves propagating along the sides of a single ridge. Scale bar, 1 μm. (B) Confocal images taken at the bottom (left) and top (right) of nanoridges, illustrating that actin polymerization occurs around individual ridges, the position of which are depicted with white lines. (C) Serial confocal images of actin waves propagating independently in nanogrooves. Scale bar, 2 μm.

We found that even in cells that migrate perpendicular to the nanoridges, actin waves still travel parallel to the nanoridges (Figure 3.2A). Our study on cell shape

dynamics using principal-component analysis has shown that cells that are perpendicular to nanoridges tend to turn to improve their alignment (*86*). The observed actin waves travelling along the nanoridges in cells that migrate perpendicular to the nanoridges may cause the cells to turn and rectify the direction of cell motion. The linear actin waves initially travel along the nanoridges at a constant speed, than stall and depolymerize (Figure 3.2B). The wave speed is 20 to 35 μm/min, which is comparable to the speed of membrane curvature waves (*96*), and is much faster than the 10-μm/min actin wave speed on a flat surface (*45*). Before stalling, the wave travels continuously on a time scale of 25 s (Figure 3.2B). This time scale is similar to the time scale that we found for dynamic, actin-based protrusions, as cells generate new protrusions roughly every 20 s (*96*).

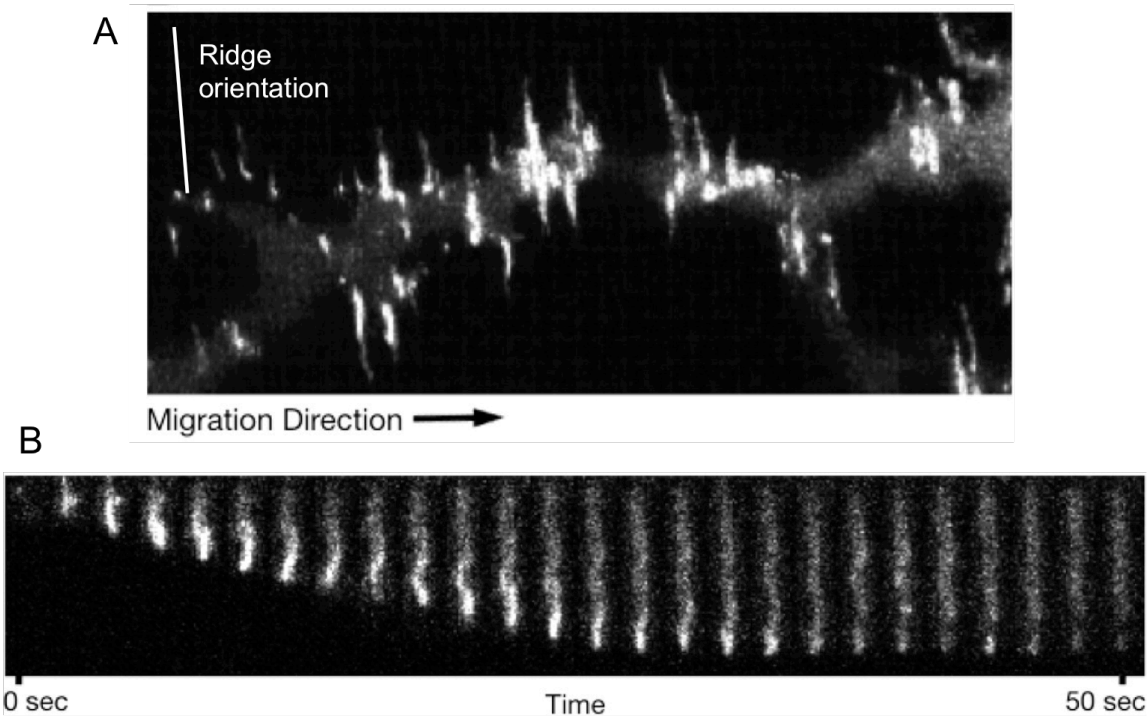

Figure 3.2. (A) Maximum-intensity projection of cells migrating perpendicular to 1.5-μm-spaced nanoridges. (B) Kymograph of an actin wave traveling between two 1.5-μm-spaced nanoridges. The wave's initial speed is 21 μm/min. Vertical scale, 13 μm.

3.2.2. Guidance efficiency on actin waves depends on ridge spacing

We imaged actin waves in *D. discoideum* cells on nanoridges that were spaced 0.8 μm, 1.5 μm, 3 μm, and 5 μm apart. We found that streaks of actin waves are more apparent on 0.8- and 1.5-μm-spaced ridges, whereas actin polymerization at the leading edge dominates on 3- and 5-μm-spaced ridges. This phenomenon can be explained by the number of ridges that individual cells span. Nanoridges with a small spacing (0.8 μm and 1.5 μm) provide more guidance cues for individual cells, and

thus promote the formation of more actin streaks. Actin streaks are also observed on nanoridges with a large spacing (3 μm and 5 μm), but the streaks often expand onto the flat area between ridges and convert into circular waves, as shown in Figure 3.3. These circular waves can still be guided when they encounter nanoridges. Figure 3.3 shows an example in which a circular wave that initially propagates perpendicular to the nanoridges collides with a ridge, transforming into actin streaks that are guided along the ridge.

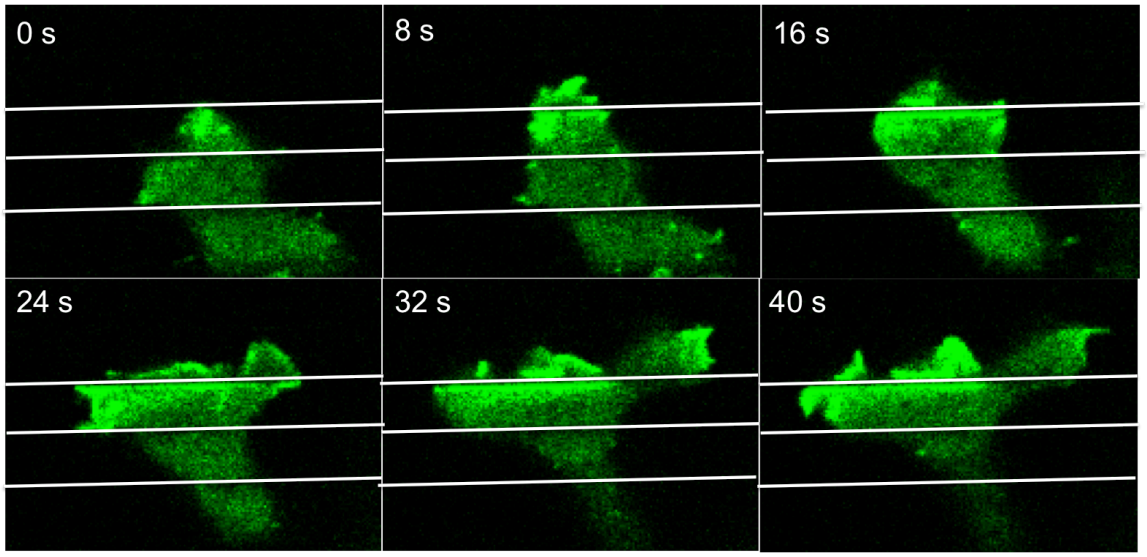

Figure 3.3. Serial confocal images of actin waves on 3-μm-spaced nanoridges. The nanoridge positions are depicted with white lines.

We adapted an optical-flow algorithm to determine the direction and magnitude of the apparent flux of actin polymerization for each pixel (details will be discussed with the tracking of actin polymerization in neutrophils in Chapter 4). The plots of actin-flux directionality show that nanoridges exert bidirectional guidance on actin

waves (Figure 3.4). The guidance efficiencies of 0.8- and 1.5-μm-spaced ridges are comparable, and are both higher than that of 3-μm-spaced ridges.

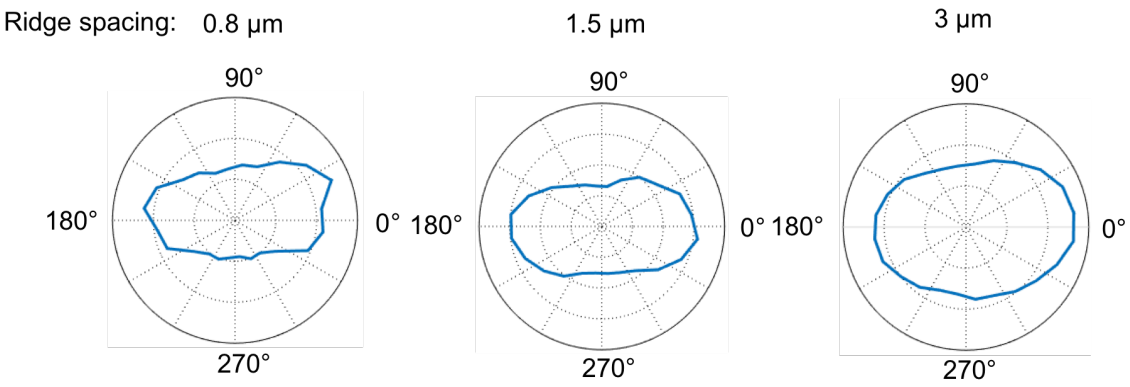

Figure 3.4. Directionality of actin waves on nanoridges with spacings of 0.8, 1.5 and 3 μm.

Our previous study showed that the highest guidance efficiency of cell motion is achieved on 1.5-μm-spaced nanoridges (*86*). This optimum spacing may be related to the intrinsic width of actin streaks. As previously discussed, the number of guidance cues for individual cells decreases as the ridge spacing increases, which explains the reduced guidance efficiency on nanoridges with a large spacing. However, as the spacing of nanoridges decreases, more actin streaks are formed. This enhanced actin polymerization may deplete the reservoir of actin monomers more quickly, and the geometric confinement between adjacent ridges may prevent new actin monomers from diffusing in. Therefore, nanoridges with a small spacing can give rise to relatively short actin streaks with a short persistence time. Such streaks may depolymerize before reaching the plasma membrane. This hypothesis can explain the

observed decrease in the guidance efficiency of 0.8-μm-spaced ridges compared with 1.5-μm-spaced ridges (*86*). Additionally, the gap between adjacent ridges can be smaller than the intrinsic width of actin streaks (500 nm), which may prevent the formation of actin streaks or result in thin actin streaks that are too weak to generate enough force on the plasma membrane. The 1.5-μm-spaced nanoridges have a ridge width of 300 nm and gap width of 1200 nm. The gap roughly fits two actin streaks adhering on the sides of adjacent ridges, presumably leading to the most efficient preferential actin polymerization along the ridges and thus the optimum contact guidance of cell motion.

We also analyzed the joint probability density of actin wave alignment and speed on nanoridges with different spacings (Figure 3.5). We found that both the variance of wave speed and the variance of wave alignment increase as the ridge spacing increases, suggesting that nanoridges constrain actin waves and mediate their characteristics.

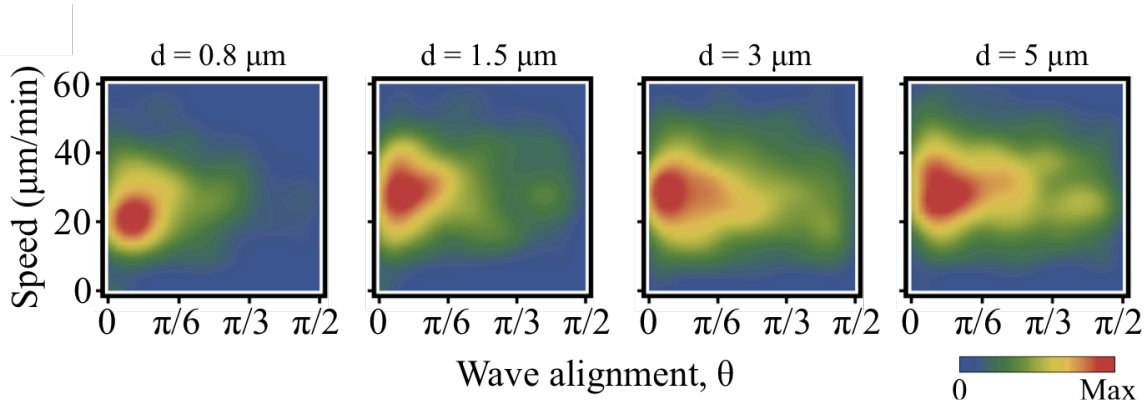

Figure 3.5. Joint probability distribution of total wave speed and wave alignment for all waves on different spacings. (Figure courtesy of Can Guven)

3.2.3. Helical actin waves between adjacent nanoridges versus linear actin waves in nanogrooves

We found that linear actin waves that initially adhere to the sides of the ridges can transform into helical waves that propagate through the gap between adjacent ridges if the nanoridges are closely spaced (spacing of 1.5 to 2 μm). Figures 3.6A and B show a top-view kymograph and a side-view snapshot, respectively, of such a helical wave on 2-μm-spaced nanoridges. The repeating helical length is 3.5 to 6.5 μm, and the diameter of the helix is 1 to 1.5 μm. The persistence time of the helical wave is roughly 22 s, after which the wave stalls and depolymerizes (Figure 3.6A). In most helical waves that we measured, the wave traveled through two helical repeating units before stalling and depolymerizing. The fact that the wave traveled through two helical lengths in 22 s gives a wave propagation speed of 19 to 35 μm/min (minimum speed: $3.5 \times 2 / 22 \times 60 = 19$ μm/min, maximum speed: $6.5 \times 2 / 22 \times 60 = 35$ μm/min), which matches the actin-wave speed that we have previously measured (see Section 3.2.1). Additionally, actin streaks adhering on the sides of a ridge also exhibit helical morphology with a half wavelength of roughly 2.5 μm, and the streaks tend to appear in opposite handedness (Figure 3.6C).

In contrast, due to the confinement in nanogrooves, actin polymerizes in linear waves (Figure 3.6D). The width of the nanogrooves is comparable to the intrinsic width of actin streaks, leaving no extra space for the helix to form. It is worth noting that persistent actin aggregates form sporadically on the linear waves, as highlighted

in white boxes in Figure 3.6D. The property and function of these actin aggregates require further investigation.

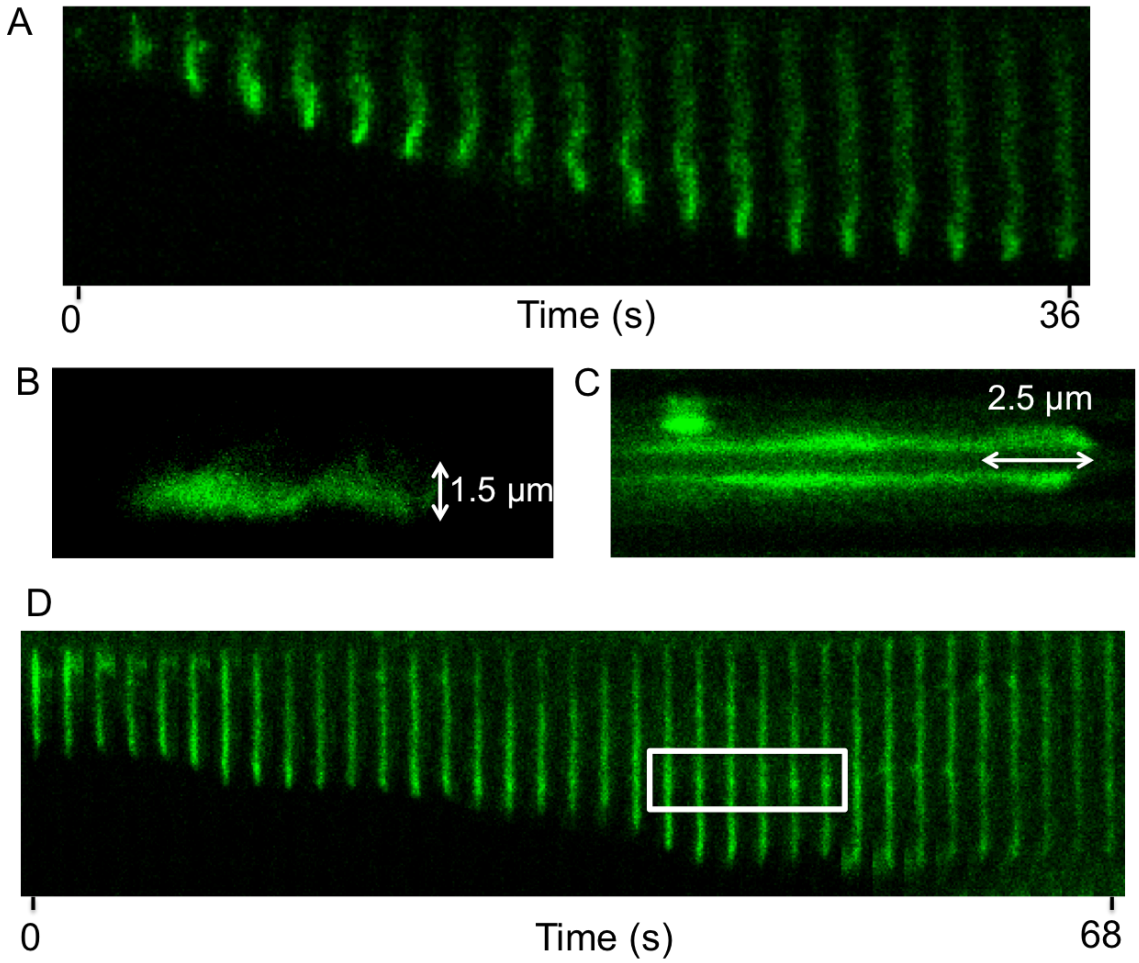

Figure 3.6. (A) Top-view kymograph and (B) side-view snapshot of a helical actin wave traveling between two 1.5-μm-spaced nanoridges. The diameter (height) of the helical wave is 1.5 μm. (C) Helical morphology of actin waves adhering on the sides of a single ridge. (D) Kymograph of straight actin waves traveling in nanogrooves that are 500-nm wide.

F-actin is intrinsically a right-handed helix (*50*). To release torque, helical filamentous molecules, such as DNA and collagen, tend to form a superhelix or a supercoil upon bending. The actin shaft within filopodia has been found to undergo helical coiling and rotational motion, leading to the axial shortening of actin bundles, which is translated into a traction force at the filopodial tip (*97*). Purich and coworkers have demonstrated that *Listeria monocytogenes* forms consistent right-handed helical actin comet tails during actin-based motility in cell-free extracts (*51*). However, this right-handed homochirality was not observed with microbeads coated with a different actin-nucleation-promoting factor, indicating that the ultrastructure of the actin network is crucial in establishing a consistent handedness, because a different actin-nucleation-promoting factor may produce a slightly different actin network architecture (*98, 99*). Bershadsky and coworkers have recently demonstrated that cellular chirality arises from actin chirality, and that cellular chirality can be reversed by mediating the torque produced by the rotation of F-actin with actin-crosslinking proteins (*100*). Although the opposite handedness of the helical actin waves on the opposite sides of a ridge (Figure 3.6C) that we proposed requires further investigation, several studies support the plausibility of our hypothesis. Vunjak-Novakovic and coworkers have found that the boundary of micropatterns is essential in establishing cellular chirality, and that the biased direction of cell migration is determined by the position of the boundary relative to the cells (*101*). Mezzenga and coworkers have found that when a chiral and polar fibril is placed in an inhomogeneous environment such as an interface, fibril bending and ring formation are induced (*102*). Based on these findings, it is reasonable to propose that the high-

curvature top surface of the nanoridges induces the initial nucleation of actin, which then propagate along the sides down to the bottom surface of the grooves, forming helical waves with opposite handedness.

3.2.4. Flickering F-actin rings around nanodots versus traveling actin waves on nanoridges with nanodots equally spaced on top

We also replicated separated nanodots with a diameter of 500 nm (Figure 3.7A) and nanodots that are connected with nanoridges (Figure 3.7B). We observed preferential actin polymerization around each nanodot (Figure 3.7C), leading to F-actin rings with a persistence time of roughly 40 s. These F-actin rings flicker on and off. Figure 3.7D shows the average fluorescence intensity around adjacent nanodots as a function of time. We found that the peak intensity around dot 1 corresponds to a dark state around dot 2, indicating that the fluorescence around adjacent nanodots is probably negatively correlated, presumably due to the competition for, and depletion of, actin monomers, actin nucleation promoting factors, and ATP in the limited microenvironment. Because there are few traveling actin waves on nanodots, cells on nanodots are reluctant to move, although they extend more filopodia to explore the environment. In contrast, actin waves on nanodots that are connected with nanoridges initiate around a dot and propagate along the ridges bidirectionally. The traveling actin waves tend to stall when they encounter a dot (Figure 3.7E). Cell migration is also bidirectionally guided along the ridges due to the guided actin waves.

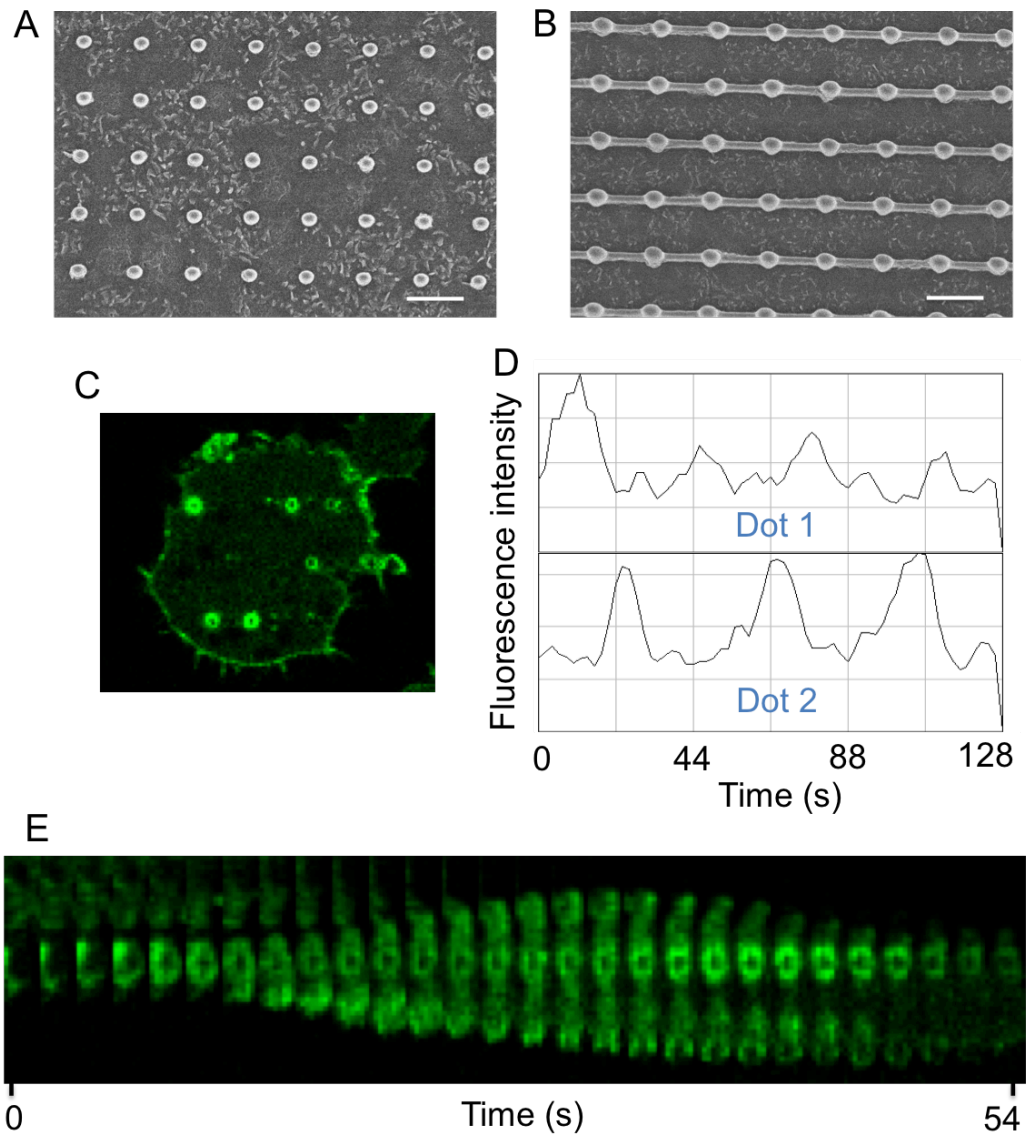

Figure 3.7. Scanning electron micrographs of separated nanodots (A) and nanodots that are connected with nanoridges (B). Scale bars, 2 μm. (C) Snapshot of persistent F-actin rings around separated nanodots. (D) Average fluorescence intensity around adjacent nanodots as a function of time. (E) Kymograph of an actin wave on nanodots that are connected with nanoridges. The wave initiates from a nanodot and travels along the nanoridge in opposite directions. The wave tends to stall upon encountering another nanodot.

3.3. Summary

We found that actin preferentially polymerizes along nanoridges and nanogrooves in *D. discoideum*. Actin waves on nanoridges exhibit coupled dynamics, whereas waves on nanogrooves do not. Actin polymerization preferentially occurs around individual nanoridges, forming a wave that travels along the ridges at 25 to 30 μm/min. Even in cells that migrate perpendicular to the nanoridges, actin waves are still mostly guided along the ridges. The guidance efficiency of actin waves depends on the spacing and gap width of the nanoridges. Nanoridges with a spacing that provides enough guidance cues for individual cells and a gap width that fits the 500-nm-wide actin streaks most efficiently, such as the 1.5-μm-spaced nanoridges with a gap width of 1.2 μm, lead to the optimum cellular contact guidance.

We observed helical actin waves that propagate through the gaps between adjacent nanoridges with a spacing of 1.5 to 2 μm. The waves travel through two helical repeating units with a persistence time of 22 s before depolymerization. Actin polymerizes into straight linear waves in nanogrooves, due to the confinement arising from the small groove width (500 nm).

Actin preferentially polymerizes into persistent rings around individual nanodots, however, actin waves on nanodots that are connected with nanoridges initiate around individual dots and propagate along the ridges. Further investigation is required to elucidate the mechanism of the transition between static and traveling actin waves.

3.4. Outlook

Because the coupled dynamics of actin waves depend on the ridge width, it is worthwhile to evaluate the effects on cellular contact guidance and actin wave dynamics of sets of ridges with constant spacing and systematically varying widths. We can establish a correlation between the ridge width and the persistence length, as well as the propagation speed, of the actin streaks. Wide ridges can be used to assess at what width the linear F-actin streaks on two sides of a single ridge do not appear in pairs. As the ridge width further increases, the gap width between adjacent ridges will drop to a value that is smaller than the intrinsic width of actin streaks (500 nm). We can assess the probability of the formation of actin streaks in these thin gaps, and how the cellular contact guidance is affected if the thin actin streaks still form. On the other hand, resolution augmentation through photo-induced deactivation (RAPID) can be employed to fabricate thinner and sharper ridges, which can be used to investigate whether the thin ridges enhance the coupled dynamics of actin waves and whether the high-curvature features promote initial actin nucleation.

We previously observed static actin aggregates with a persistence time of tens of seconds in cells that were plated on nanoparticle-coated surfaces and reactive-ion-etching-treated (RIE-treated) polymer films (nanograss). Based on this observation, we hypothesize that rough surfaces induce the formation of static F-actin. It is of great interest to investigate the effect of rough nanoridges – such as RIE-treated ridges and nanoparticle-coated ridges – on guidance efficiency. Both of these nanotopographies can be molded through solvent-assisted nTM with high fidelity, as

discussed in Chapter 2. The replication of the nanoparticle-coated ridges with acrylic resin provides a nanoparticle-topography with uniform surface chemistry, which can be used to assess the toxicity of nanoparticles through their physical interference with actin. Additionally, tilted nanograss with a specific angle relative to the surface can be prepared through RIE. This introduced anisotropy may guide both actin waves and cell migration in a particular direction. Further experiments are needed to shed light on the interaction between actin waves and enhanced surface roughness.

Super-resolution microscopy is needed to study the structural details (*e.g.* handedness) and dynamics of the helical actin waves that we observed on 1.5- and 2-μm-spaced nanoridges. Structured illumination microscopy (SIM) is an excellent option due to its high temporal and spatial resolution, as well as its compatibility with a broad variety of dyes, such as GFP. We can use SIM to observe the dynamics of deformed helical actin waves. The different types of deformation of a helix, such as bending, twisting, and stretching, are interdependent. Bending the helical wave by curved ridges with a particular curvature may twist a helix with one type of handedness and untwist a helix with the opposite handedness, causing one type of handedness to be more stable than the other. Enhancement of the favored handedness may lead to unidirectional cell motion. On the other hand, based on the observation of persistent F-actin rings around individual nanodots, standing waves of actin polymerization could be induced by a microdot with a bump on the periphery. The bump is intended to promote the initial nucleation of actin. The actin polymerization waves are likely to travel along the periphery of the microdot in the opposite directions. If the circumference of the microdot equals an integer number of

wavelengths, standing waves could form along the periphery of the microdot. All of these proposed experiments will deepen our understanding of helical actin waves.

3.5. Materials and Methods

LimEΔcoil-GFP *D. discoideum* cells from an AX3 background were grown in HL-5 medium (In 1 liter of water: 20 g of maltose, 10 g of bacto proteose peptone, 5 g of bacto yeast extract, 0.965 g of $Na_2HPO_4 \cdot 7H_2O$, 0.485 g of KH_2PO_4, and 0.03 g of streptomycin) at 21.5°C, washed with development buffer (DB) (5-mM Na_2HPO_4, 5-mM NaH_2PO_4, 2-mM $MgSO_4$, and 0.2-mM $CaCl_2$), and resuspended in DB at a density of 2×10^7 cells/mL. Cells were pulsed with 20-nM cyclic adenosine monophosphate (cAMP) every 6 minutes for 5 h while being shaken at 150 rpm. To block the intracellular cAMP synthesis and cut off signal relay, cells were incubated with 2-mM caffeine for 20 minutes after development (*55*). After being plated onto a nanoridge surface, cells were stimulated with extraneous cAMP with a uniform concentration of 5 μM. Both fluorescence and bright-field images were obtained simultaneously on a Leica SP5 X confocal microscope every 2 seconds with a 100× objective.

Chapter 4: Asymmetric Nanotopography Biases Cytoskeletal Dynamics and Promotes Unidirectional Cell Guidance

This chapter is adapted from Sun, Driscoll, Guven, Das, Parent, Fourkas and Losert. The manuscript is submitted to *Proc. Natl. Acad. Sci. U.S.A.* and is under review. Sun carried out the fabrication of sawteeth and cell experiments. Driscoll and Guven contributed the analysis. Das contributed to the neutrophil experiments.

4.1. Introduction

Directed cell migration is essential for many critical biological and physiological processes (*1*), such as embryonic development (*2*), wound healing (*3*), immune response (*4*) and angiogenesis (*5*). Guidance of cells can be achieved through external gradients in properties such as chemical concentration (*14, 15*), substrate rigidity (*16*), and adhesion (*19*). The total distance over which gradients can guide cells is limited by the finite dynamic range of cellular sensing, i. e. guidance by a gradient between the front and back of each cell requires that the overall signal change significantly with the cell's position (Figure 4.1A). Cells can overcome this limitation by relaying chemotactic signals, but chemical relay of directional information requires intricate orchestration and timing of signals (*7, 8, 15*). Shear flow is another approach to guide cells unidirectionally over large distances, but it is an active process that requires constant fluid flow. Additionally, the flow rate and the viscosity of the fluid need to

be controlled precisely to produce an accurate shear stress (*20, 21*). Surface nanotopography, such as ridges, grooves (*30, 39, 86, 103*) or aligned collagen fibers (*104*), can act as a primitive and ubiquitous guidance cue, but the symmetric structures used in prior studies only provided bidirectional guidance.

Although previous work has implicated cytoskeletal structures (in particular, the alignment of stress fibers (*39*)) in similar contact guidance processes, we have shown that nanotopography also steers the dynamics of the cell's scaffolding by biasing actin polymerization waves (*86*) (see Chapter 3). Intracellular dynamics that involve the self-assembly of actin and its associated proteins into three-dimensional, traveling waves that propel a cell forward through a sustained cycle of polymerization and depolymerization have recently been found to be ubiquitous in cell migration (*45, 46, 48, 56*). Nanotopographies that are present in natural and physiological environments, such as collagen fibers, often include asymmetric structures. We therefore hypothesized that nanotopographic asymmetries on an appropriate length scale can bias actin waves and cell migration unidirectionally.

We used surfaces composed of parallel ridges of nanosawteeth (Figure 4.1B) to induce unidirectional guidance in two prototypical cell types that move via amoeboid migration: *Dictyostelium discoideum*, which migrates using pseudopods that protrude away from surface contacts, and neutrophils, which migrate using lamellipodia that spread along surface contacts. Investigating cell types that use distinct mechanisms in migration will help to reveal the generality of the phenomenon of biasing actin waves and cell migration through asymmetric nanotopographies.

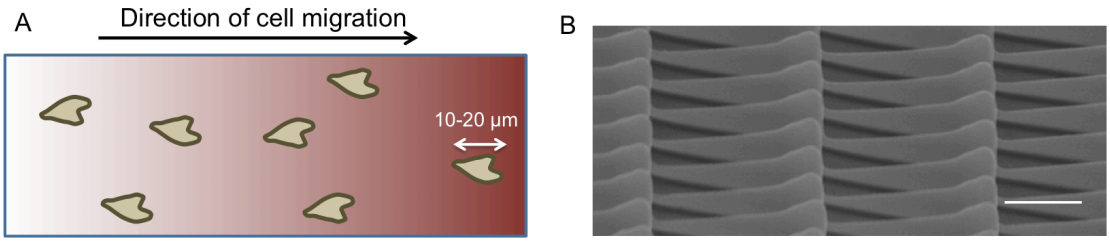

Figure 4.1. (A) A global gradient must be maintained over a distance that is much larger than the cell length. (B) Side-view scanning electron micrograph of nanosawteeth. Scale bar, 3 μm.

4.2. Results and Discussion

4.2.1. Nanosawteeth guide cell migration unidirectionally

The sawtooth dimensions (length, height, and width) and the spacing between adjacent sawtooth ridges are all comparable in size to natural collagen fibers (*104*), and are considerably smaller than the dimensions of an individual cell (the average width of a polarized cell is 5 μm for *D. discoideum* and 10 μm for neutrophils). Thus, individual cells span several ridges and many sawteeth (Figure 4.2A).

To explore how *D. discoideum* conforms to nanosawteeth, we visualized YFP-labeled cAR1 cells, which express a fluorescent transmembrane protein that is uniformly distributed in the plasma membrane (*105*). Figures 4.2B and C show top- and side-view fluorescent confocal images, respectively, of an individual cell on a nanosawtooth surface. The nanosawtooth boundary highlighted in the top-view image indicates that the cell membrane is in contact with the entire surface of each nanosawtooth, leading to a thicker plasma membrane around the nano-sawteeth, and

hence an increased cAR1-YFP density. Side-view images confirm that cells conform to the deepest and highest positions of nanosawteeth.

We imaged signal-relay-deficient *D. discoideum* cells (*aca*$^{-}$ mutants) without an external chemical gradient to study nanotopographic cell guidance. The cytoplasm was dyed with cellTracker Green (*15*) to enable tracking of centroid motion. Representative tracks (Figure 4.2D) exhibit substantial unidirectional bias up the nanosawtooth slope.

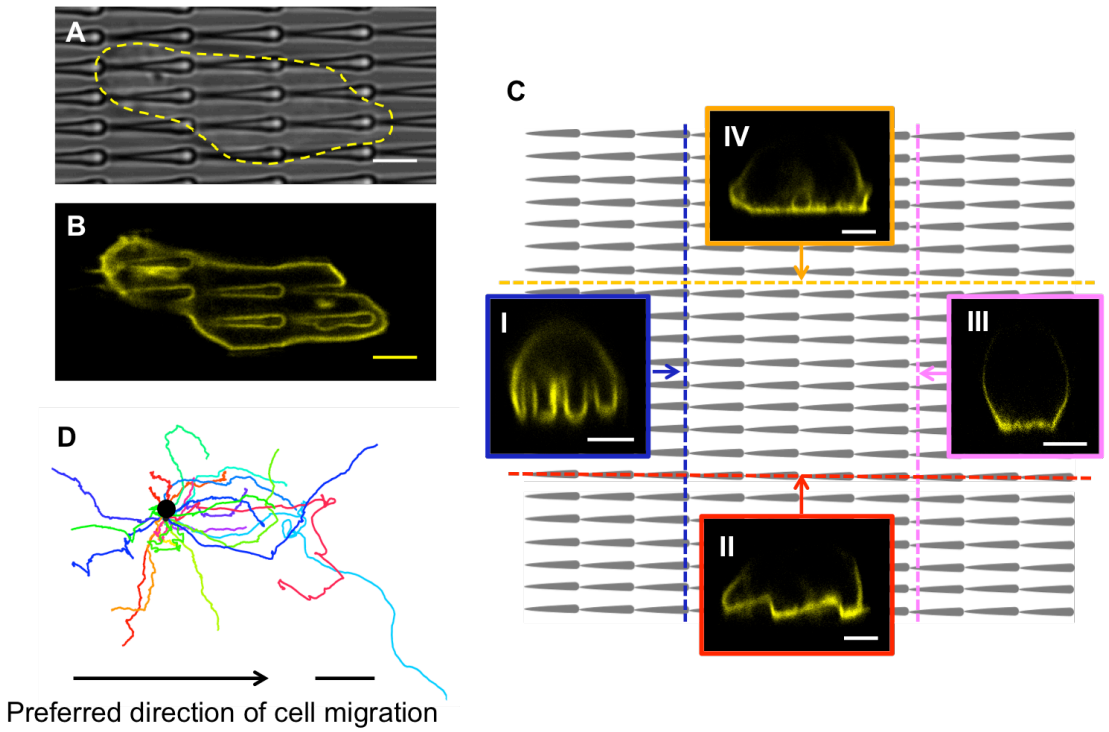

Figure 4.2. Guidance of cells by a surface with 2-µm-spaced ridges of sawteeth of length 6 µm, height 1.8 µm, and width 630 nm (denoted as 6-µm sawteeth). (A) Top-view bright-field and (B) confocal micrographs of a cAR1-YFP-expressing cell on nanosawteeth. The dashed line in (A) delineates the cell boundary. (C) Side-view confocal micrographs of different cross-sections of a cAR1-YFP-expressing cell on nanosawteeth. The grey background schematic represents the nanosawtooth surface. Each image was obtained at a plane perpendicular to the surface in the position of the dashed line of the color of the image border. Scale bars in (A)-(C), 3 µm. (D) Centroid motion tracks of 25 representative cells over 18 min. All tracks were translated to begin at the black dot. The height of each sawtooth increases from left to right. Scale bar, 20 µm.

4.2.2. The direction of cellular contact guidance depends on the details of the nanosawteeth

To quantify the unidirectional bias, we analyzed cellular velocity with respect to the orientation of 2-μm-spaced ridges composed of nanosawteeth either 8 μm long, 2.4 μm high, and 630 nm wide (denoted as 8-μm sawteeth) or 2 μm long, 1 μm high and 630 nm wide (denoted as 2-μm sawteeth). The polar histogram (Figure 4.3A) and the probability distribution (Figure 4.3B) of the direction of motion on 8-μm sawteeth demonstrate bias of motion up the sawtooth slope. There is also a slight preference for motion along the 90°-270° axis. This minor component of directional bias arises because the sawtooth ridges are in registry, and so the sawtooth minima act as grooves that are perpendicular to the ridges. The slowest cells exhibit the smallest degree of directional preference in their migration (Figure 4.3D). Furthermore, the most elongated cells show the greatest alignment with the ridges (Figure 4.3E). In contrast, the preferred direction on 2-μm sawteeth is down the nanosawtooth slope (Figures 4.3F-J). These results illustrate that the direction of guidance is dependent on the details of the nanotopography.

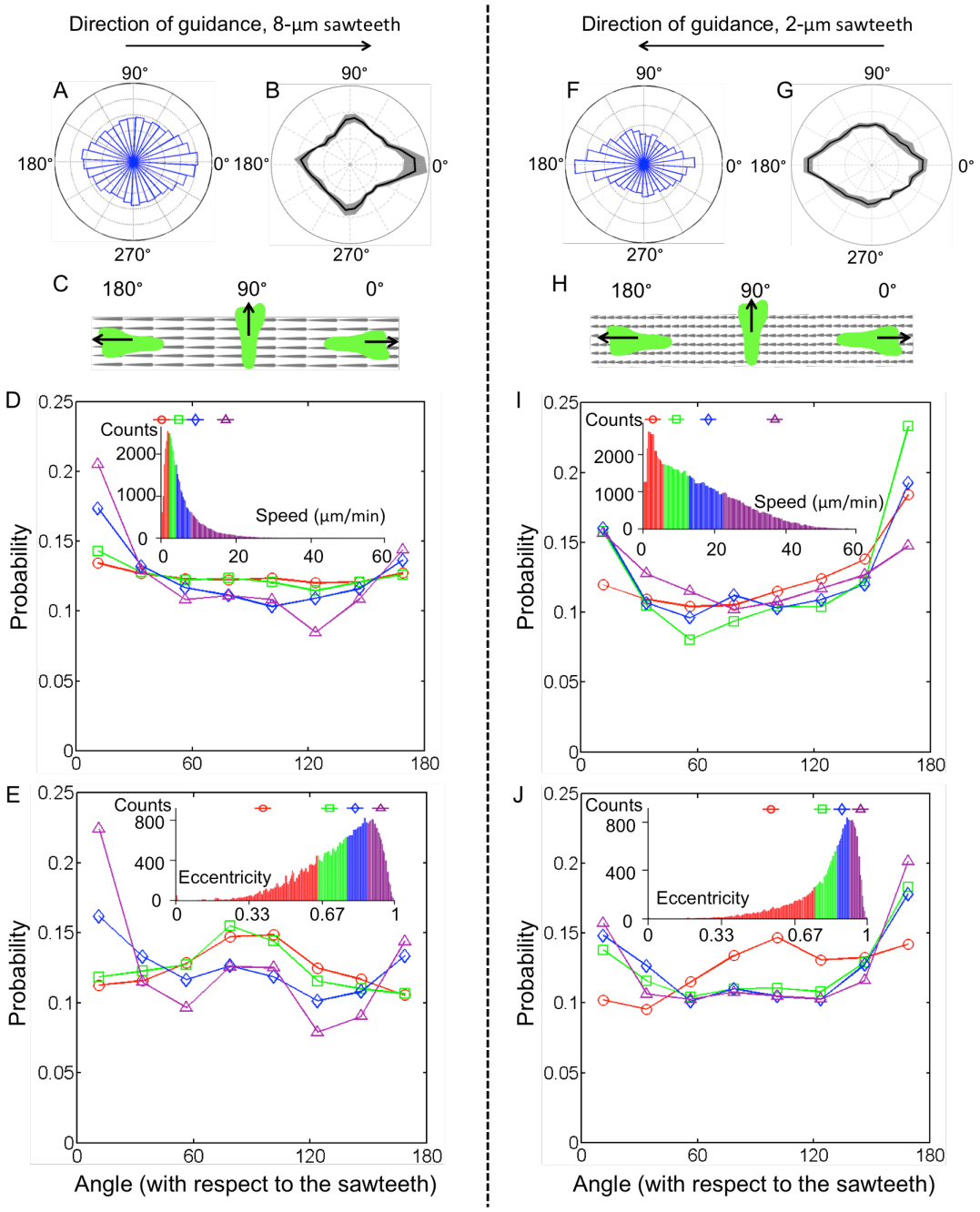

Figure 4.3. Unidirectional cell migration is sensitive to details of the nanotopography. On 8-μm sawteeth cells migrate up the slant (A)-(E), whereas on 2-μm sawteeth they migrate down the slant (F)-(J). (A),(F) Polar histograms of the direction of motion. (B),(G) Probability distributions of the direction of motion weighted by speed. The solid line is an average over three experiments. The shaded area represents the standard error. (C),(H) Cartoons illustrate the definitions of the angles used to describe cell motion relative to the sawteeth. (D),(I) Probability densities of cellular velocity with respect to the sawtooth orientation. The inset shows the speed distribution and range for each quartile. (E),(J) Probability densities of cellular alignment with respect to the sawtooth orientation. The alignment direction is corrected by the direction of motion. The insets show the eccentricity distribution and range for each quartile.

For further assessment of the relationship between the guidance direction and the frequency at which the cell encounters the sawteeth, it would be desirable to study cell motion on nanosawtooth surfaces in which the sawtooth length is 1 μm or smaller. However, due to the constraints of our fabrication method, it is difficult to fabricate asymmetric sawteeth with lengths of 1 μm or less. Instead, we fabricated nanosawtooth surfaces with an offset configuration in which the adjacent ridges are out of phase at a constant distance. Cell migration was monitored on such surfaces featuring 800-nm-spaced ridges of sawteeth of length 2 μm, height 400 nm, and width 400 nm (Figures 4.4A and *B*). Sawteeth in adjacent ridges were offset by 1 μm. Due to this offset, a cell encounters one new tooth for every 1 μm of displacement. The spacing between ridges was reduced from 2 μm to 0.8 μm to provide each cell with more guidance cues. The probability distribution of direction of motion (Figure 4.4C) indicates that cells tend to migrate parallel to the ridges and down the sawteeth.

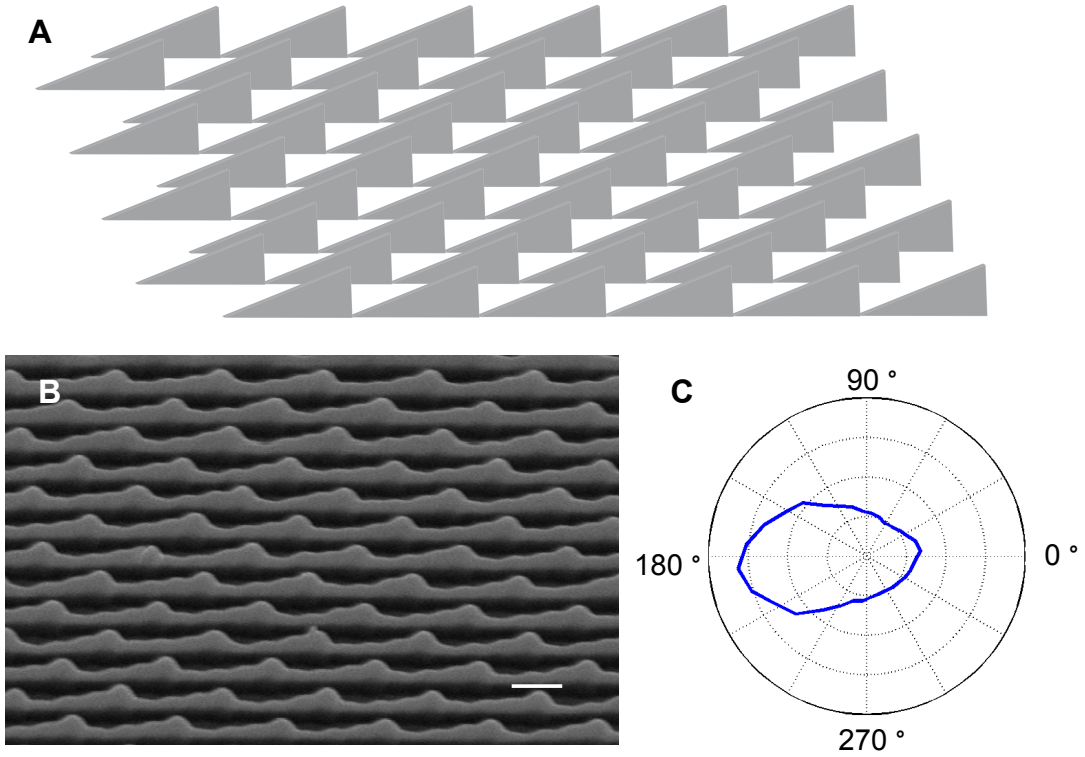

Figure 4.4. Unidirectional guidance of cell motion by a surface of offset, 2-μm nanosawteeth. (A) Schematic diagram and (B) side-view scanning electron micrograph of the offset nanosawteeth. (C) Probability distribution of direction of motion weighted by speed, averaged over three experiments. Scale bar in (B), 1 μm.

4.2.3. Actin waves are guided in the same direction as and are more strongly biased than is cell migration

We next consider how the sawteeth influence intracellular dynamics. Snapshots of the spatial distribution and dynamics of actin filaments (F-actin) using cells that overexpress proteins associated with actin polymerization (LimEΔcoil-GFP and LifeAct-TagRFP) show that F-actin forms streak-like linear structures parallel to the

ridges of 8-μm nanosawteeth. These structures extend 500 nm away from the ridges. Time-lapse imaging reveals that F-actin streaks are actin polymerization waves in which the leading tip of each streak sweeps to probe the nanoenvironment. The linear actin structures that adhere to the opposite sides of a sawtooth typically exhibit coupled dynamics (Figures 4.5A-C), as is seen in the actin streaks adhering to the sides of the nanoridges (see Chapter 3). To confirm that the dynamic fluorescence arises from the *in situ* actin polymerization rather than from an optical effect, we imaged cAR1-YFP cells migrating on the nano-sawtooth surface as a control. The fluorescence in the plasma membrane remains spatially uniform, with no apparent bursts of intensity enhancement or depletion.

To assess the role of the ridges in the unidirectional contact guidance, cell motion was analyzed on a single sawtooth "ridge" with a width of 300 μm (i.e. a pattern akin to closed louvers). Cell motion on a film of 8-μm-long, 2.4-μm-high sawteeth (Figures 4.6A and B) exhibits a bidirectional bias along the perpendicular sawtooth grooves, whereas migration along the sawteeth is suppressed (Figure 4.6C). Therefore, the existence of ridges is a prerequisite for achieving unidirectional guidance, presumably because the edges of ridges promote the streak-like polymerization of actin adhering to them.

We adapted an optical-flow algorithm to determine the direction and magnitude of the apparent flux of actin polymerization for each pixel. Although this flux has the same preferred direction as cell motion, actin polymerization is more strongly unidirectional than is cell migration (cf. Figures 4.3B and 4.5D). Averaging polymerization activity around each 8-μm sawtooth shows that sawtooth minima

serve as sources of actin polymerization waves that propagate up the sawteeth (Figure 4.5E). The actin waves have a uniform speed, but sometimes stall at the tips of sawteeth (Figure 4.5F). 2-μm nanosawteeth also induce localized waves that are confined along the tops of the sawteeth (Figures 4.5G-L), yet in this case the waves migrate preferentially down the sawtooth slope. The speed of actin waves is comparable in both cases, about 30 μm/min. This behavior is consistent with the observed cell motion. As was the case for 8-μm sawteeth, actin polymerization is more strongly biased than is migration for 2-μm sawteeth (cf. Figures 4.3G and 4.5J).

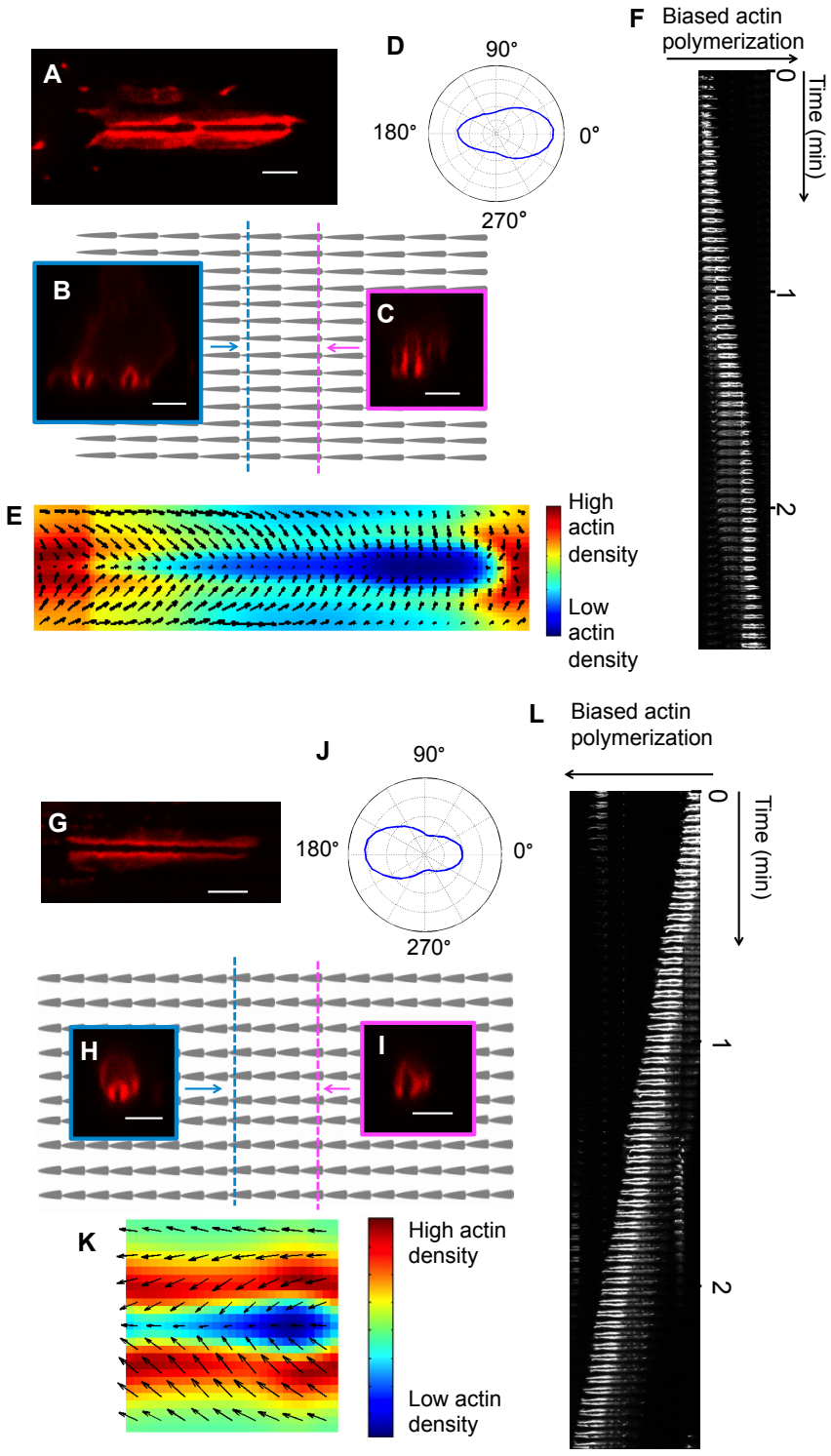

Figure 4.5. Actin morphology and flux for *D. discoideum* depend on details of the nanotopography. (A)-(F) 8-µm nanosawteeth and (G)-(L) 2-µm nanosawteeth. (A),(G) Top-view confocal micrographs of F-actin on nanosawteeth. Confocal micrographs of cross-sections perpendicular to the ridges going through (B),(H) the sawtooth minima and (C),(I) maxima. (D),(J) Actin-wave directionality. (E),(K) Average actin flux around a nanosawtooth. (F),(L) 60-frame (2.55-min) space/time plot of actin waves along a ridge. Scale bars: 3 µm in (A)-(C) and (G)-(I), 16 µm in (F) and 4 µm in (L).

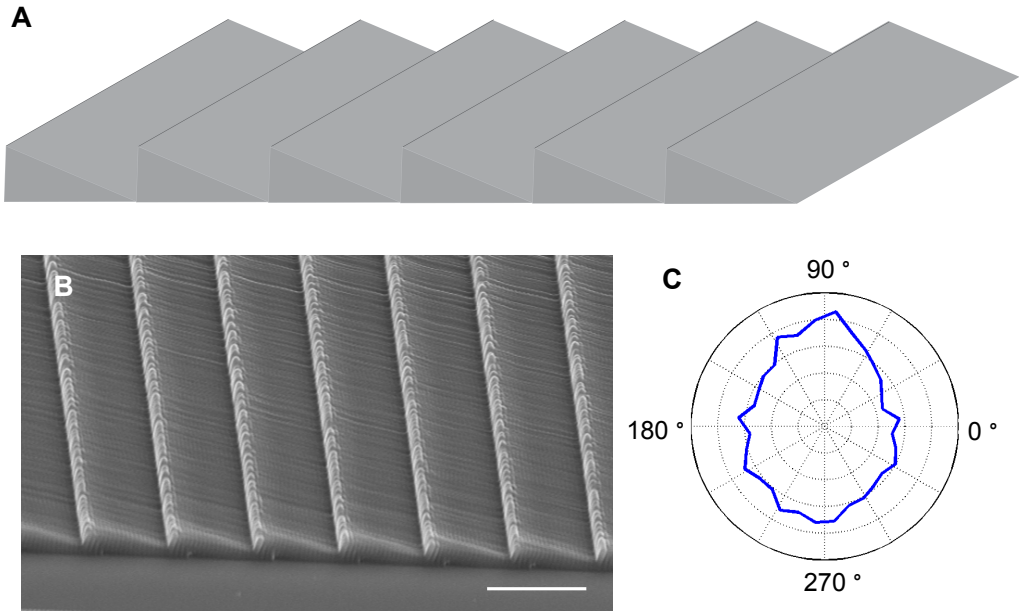

Figure 4.6. Perpendicular bidirectional guidance of cell motion by continuous, 8-μm sawteeth. (A) Schematic diagram and (B) scanning electron micrograph of the sawtooth film. (C) Probability distribution of direction of motion weighted by speed. Scale bar in (B), 10 μm.

We also studied actin-wave propagation in human neutrophils (YFP-actin HL60). Unlike *D. discoideum*, which protrudes pseudopods that can be microns above the surface, neutrophils extend lamellipodia (Figures 4.7A and B) that adhere firmly to the surface. The actin-wave dynamics in HL60 cells on nanosawteeth are similar to those of *D. discoideum*, even though actin waves in HL60 cells are localized in lamellipodia. HL60 cells on 8-μm nanosawteeth exhibit unidirectional bias of actin waves and migrate up the sawteeth (Figure 4.7C). Individual actin waves undergo persistent propagation along multiple sawteeth (Figure 4.7D). The average speed of actin waves in HL60 cells is faster when the waves are propagating up the

sawteeth than when they are propagating down the sawteeth (Figure 4.7E), and is significantly slower than in *D. discoideum*. Actin waves in HL60 cells on 2-μm nanosawteeth exhibit bidirectional guidance (Figure 4.7F). The speed of the actin waves on 2-μm nanosawteeth is significantly slower than that on 8-μm nanosawteeth (Figure 4.7G).

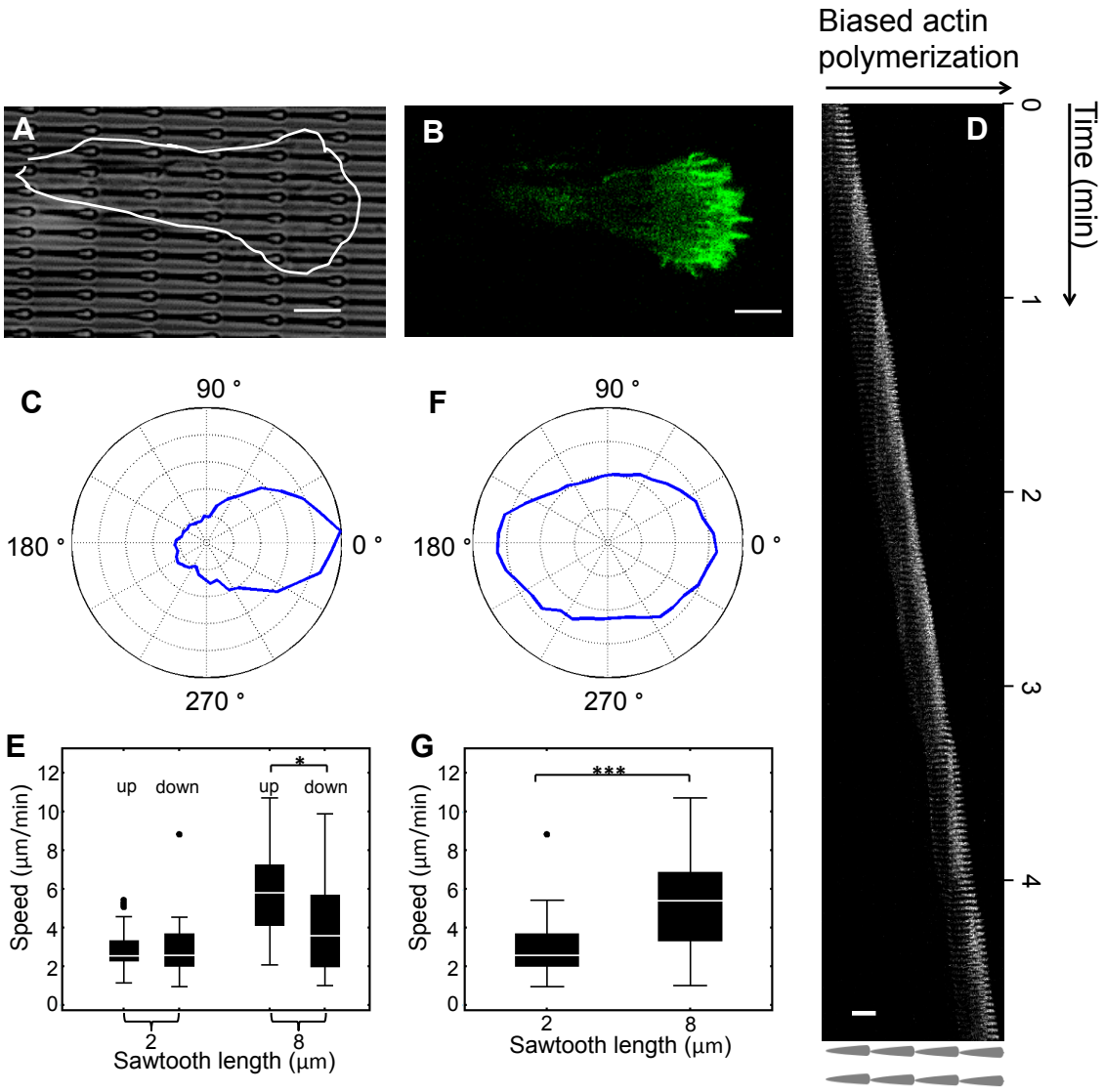

Figure 4.7. Cellular morphology and actin waves of YFP-actin HL60 neutrophils on nanosawteeth. (A) Bright-field micrograph and (B) confocal micrograph of a polarized neutrophil. (C),(F) Directionality of actin waves. (D) Space/time plot of actin waves along a ridge over 146 frames (4.83 min). (E),(G) Actin-wave propagation speed. * $P \leqslant 0.05$, *** $P \leqslant 0.001$. Scale bars: 4 μm in (A) and (B), 8 μm in (D).

4.2.4. Separated nanosawteeth guide actin waves unidirectionally, but not cell motion

To investigate whether the continuity of the nanosawtooth ridges and their spacing are crucial for unidirectional guidance, we studied cell motion and actin waves on separated nanosawteeth (Figure 4.8A). Because we observed consistent unidirectional guidance down the slope on 2-μm sawteeth, and up the slope on both 6-μm (Figure 4.8B-E) and 8-μm sawteeth, we fabricated 2-μm-spaced ridges composed of 6-μm-separated 2-μm sawteeth (Figure 4.8F) and 2-μm-separated 6-μm sawteeth (Figure 4.8G), as well as 4-μm-spaced ridges composed of 2-μm-separated 6-μm sawteeth (Figure 4.8H) and 8-μm sawteeth (Figure 4.8I). All of these separated sawteeth are connected with ridges to retain the linear actin waves. A constant periodicity of 8 μm (the sum of sawtooth length and separation length) is maintained to keep the frequency at which the cell encounters the sawteeth along a single ridge the same. We found that cell guidance is predominantly bidirectional on all of these separated nanosawteeth (Figures 4.8J-M). Although Figures 4.8K and L show a slight bias towards up the slope, this bias is not significant. Despite the lack of unidirectional cellular contact guidance, separated nanosawteeth guide actin waves unidirectionally (Figures 4.8N-S). The preferred guidance direction is consistent with that of the continuous nanosawteeth of the same length, although the bias is weaker (cf. Figures 4.8N and 4.5J, 4.8O and 4.8 D). Actin waves on nanosawteeth with a ridge spacing of 2 μm are more confined along the ridges than those on nanosawteeth with a ridge spacing of 4 μm (cf. Figures 4.8O and P). This phenomenon corresponds with our results for actin waves on nanoridges with different spacings (see Chapter 3).

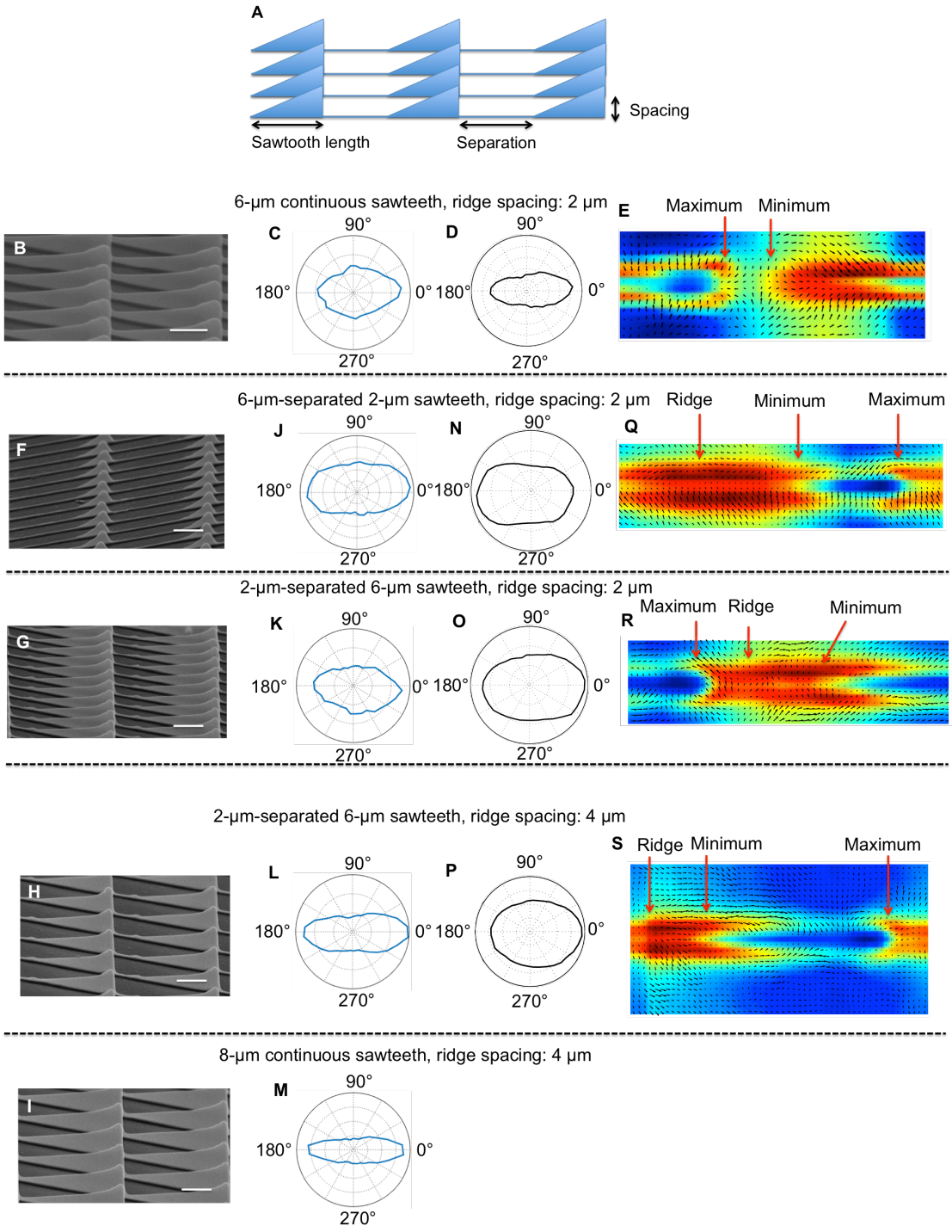

Figure 4.8. Guidance of cell motion and actin waves on continuous and separated nanosawteeth. (A) A schematic of separated nanosawteeth with connecting ridges. (B), (F)-(I) Scanning electron micrographs. Scale bars, 2 μm. (C), (J)-(M), Probability distributions of the direction of motion weighted by speed. (D), (N)-(P), Actin-wave directionality. (E), (Q)-(S) Average actin flux around a nanosawtooth.

We also studied actin waves on 2-μm-separated, 6-μm sawteeth and 6-μm-separated, 2-μm sawteeth without connecting ridges. In contrast to other 6-μm sawteeth we have investigated, 2-μm-separated 6-μm sawteeth without connecting ridges guide actin waves down the sawteeth (Figure 4.9A). 6-μm-separated, 2-μm sawteeth without connecting ridges exhibit minimal actin-wave guidance (Figure 4.9B). The average actin flux around each type of separated sawtooth shows that the sawtooth maxima serve as sources of actin polymerization waves that propagate down the sawteeth (Figure 4.9C and D). On 6-μm-separated, 2-μm sawteeth, the large portion of random actin waves on the flat area dominates, overwhelming the small portion of guided actin waves around the sawteeth. Figures 4.9E and F are kymographs of an actin wave around 6-μm-separated, 2-μm sawteeth with (Figure 4.9E) and without connecting ridges (Figure 4.9F), respectively. On both types of nanosawteeth, actin wave are initiated at the maxima and propagate down the slope of the sawtooth. However, on the separated sawtooth without connecting ridges, the linear actin wave loses its directionality and converts into circular waves upon reaching the flat area (Figure 4.9F). Due to the large separation between adjacent sawteeth, many guided actin waves around the sawteeth lose their directionality before pushing on the plasma membrane, resulting in random cell motion. For the separated sawteeth with connecting ridges, the inclusion of the ridges increases the probability of bidirectional guidance of actin waves. Even if a wave that propagates down a sawtooth is still guided along the ridge, it may stall and depolymerize before reaching the membrane, leading to the observed bidirectional guidance of cell motion (Figures 4.8H-K). Therefore, unidirectional cellular contact guidance is only achieved

with continuous nanosawteeth, on which actin waves are efficiently induced and guided, frequently pushing on the plasma membrane to propel the cell in a preferred direction.

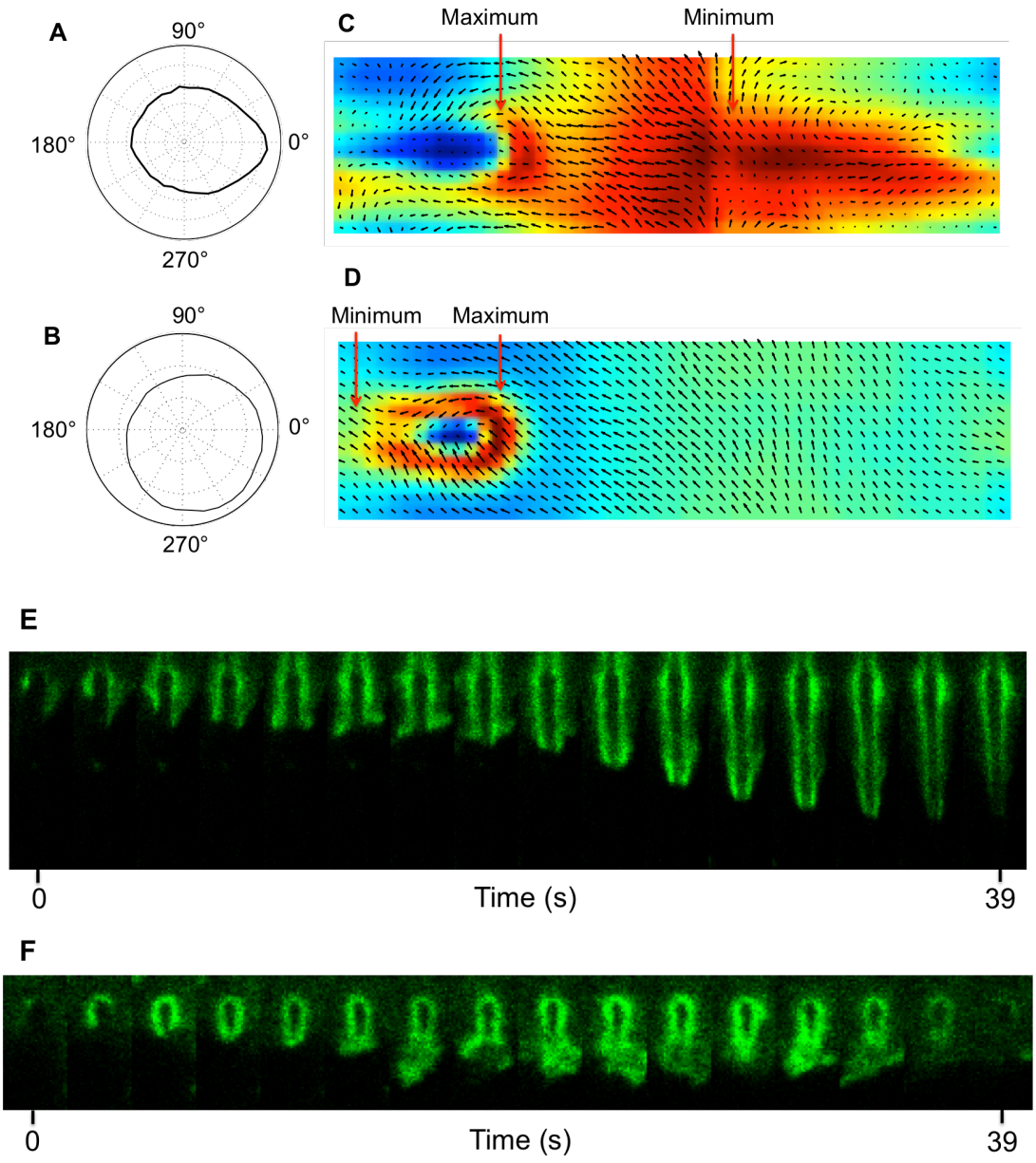

Figure 4.9. (A) Actin-wave directionality and (C) average actin flux around a nanosawtooth on 2-μm-separated, 6-μm sawteeth withouth connecting ridges. (B) Actin-wave directionality and (D) average actin flux around a nanosawtooth on 6-μm-separated, 2-μm sawteeth withouth connecting ridges. Kymographs of an actin wave on 6-μm-separated, 2-μm sawteeth with (E) and without (F) connecting ridges.

4.3. Summary

Our results demonstrate unambiguously that unidirectional guidance can be achieved by local nanotopographical gradients on scales smaller than that of a single cell, and comparable to typical sizes of collagen fibers. Nanotopography guides intracellular dynamics (waves of actin polymerization), propelling the cell in a preferred direction. The conservation of this behavior for different cell types with distinct surface interactions during migration, and the prevalence of polarity and asymmetry in the local microenvironment of cells, suggest that biasing of intracellular waves is important in many physiological processes. For instance, aligned collagen fibers guide cancer cells, and are a prognostic signature of breast carcinoma (*106*). Our results suggest the possibility that asymmetric nanotopography of collagen fibers promotes unidirectional contact guidance *in vivo*. Controlled anisotropic nanotopographies imprinted on surfaces or embedded in three-dimensional structures should be able to guide cells over large distances, with possible applications in the broad range of biomedical problems in which directed cell migration is important.

4.4. Materials and Methods

4.4.1. Coating nanosawtooth surfaces with fibronection

The fabrication and molding of nanosawteeth has been described in Chapter 2. Nanosawtooth surfaces for neutrophils were UV cured for 50 s (Blak-Ray, B-100AP, 100 W, 365 nm, samples were cured 254 mm from the source), baked at 90 °C for 10 min, and then coated with 1 μg/mL fibronectin in HBSS (F1141, Sigma-Aldrich;

fluorescent fibronectin: FNR02-A, Cytoskeleton) at 37 °C for 1 h. The coated surfaces exhibit uniform fibronectin density (Figure 4.10).

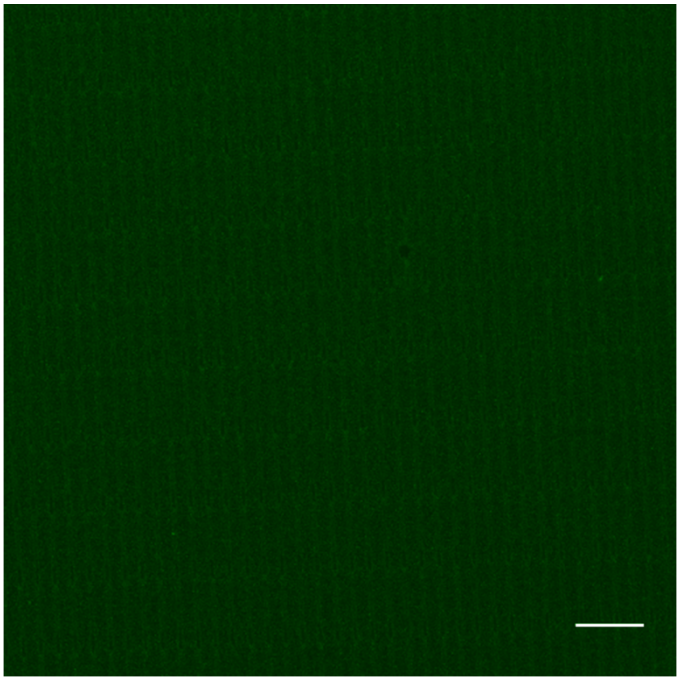

Figure 4.10. Maximum intensity projection of *z*-stack confocal images of a nanosawtooth surface coated with fluorescent fibronectin (green fluorescent, HiLyte 488). The uniform fluorescence intensity indicates a uniform fibronectin coating. Scale bar, 8 μm.

4.4.2. Cell preparation and imaging

Dictyostelium discoideum cells, cAR1-YFP, *aca*$^-$, LimEΔcoil-GFP and Lifeact-TagRFP/*aca*$^-$ (all are in an AX3 background) were prepared as described previously (*15*). cAR1-YFP and LimEΔcoil-GFP cells were developed for 4 hours. *aca*$^-$ and Lifeact-TagRFP/*aca*$^-$ cells were developed for 5 hours.

cAR1-YFP cells were incubated with 2-mM caffeine for 20 minutes to block the intracellular activation of cAMP synthesis (*55*). After being plated onto a nanosawtooth surface, cells were stimulated with extraneous cAMP with a uniform concentration of 5 μM. Fluorescence images were obtained on a Leica SP5 X confocal microscope every 2 seconds with a 100× objective and a scanner zoom factor of 2.

For cell motion imaging, *aca*$^-$ cells were cytoplasmically dyed with 25-μM CellTracker Green CDMFA (Invitrogen) for 30 minutes and then washed twice with phosphate buffer. After being plated onto a nanosawtooth surface, cells were stimulated with extraneous cAMP with a uniform concentration of 100 nM. Fluorescence images of *aca*$^-$ cells were obtained on a Leica TCS SP2 confocal microscope every 4 seconds for 80 min with a 10× objective and a scanner zoom factor of 2. Images were obtained in a 512 × 512 pixel format.

For actin-wave imaging, LimEΔcoil-GFP cells were incubated with 2-mM caffeine for 20 minutes after development. LimEΔcoil-GFP and Lifeact-TagRFP/*aca*$^-$ cells were stimulated with extraneous cAMP with a uniform concentration of 5 μM and 100 nM, respectively. Both fluorescence and bright-field images were obtained simultaneously on a Leica SP5 X confocal microscope every 2.6 seconds with a 100× objective and a scanner zoom factor of 2. Images were obtained in a 1024 × 1024 pixel format to provide more information for actin-flux analysis.

The neutrophil-like human leukaemia cell line HL60 overexpressing YFP-actin was a kind gift of Dr. Orion Weiner (University of California, San Francisco). Cells

were maintained in RPMI 1640 (medium developed at Roswell Park Memorial Institute) with Glutamax (Invitrogen), 10% fetal bovine serum and penicillin/streptomycin. Cells were passaged every 3 to 4 days to maintain a density between 10^5 cells/ml and 10^6 cells/ml. Cells were differentiated at a density of 4.5×10^5 cells/ml for 6 days in culture medium containing 1.3% dimethyl sulfoxide. Before imaging, cells were plated on a nanosawtooth surface coated with 1 μg/mL fibronectin and stimulated with 100-nM f-Met-Leu-Phe (fMLP) in mHBSS for 10 min. Fluorescence and bright-field time-lapse images were obtained on a Leica SP5 X confocal microscope every 2 seconds with a 100× objective.

4.4.3. Tracking cells

This section is contributed by Meghan Driscoll

Migrating *D. discoideum* cells were tracked as previously described (*15, 86*). Due to image noise, even stationary cells appear to have a direction of motion. We therefore measured the distribution of direction of motion in two different ways: a simple histogram of direction of motion (*e.g.*, Figures 4.3A and E) and a probability distribution of direction of motion weighted by speed (*e.g.*, Figures 4.3B and F). The weighted plots show the net speed of cells moving in each direction. In all plots, each included speed corresponds to that of a cell in a specific frame rather than the mean speed of a single cell averaged across time.

We also plotted the velocity direction distributions (unweighted) for each speed quartile (*e.g.*, Figures 4.3C and G) and the orientation distributions for each eccentricity quartile (*e.g.*, Figures 4.3D and H). Angles were defined relative to the sawtooth orientation; a cell migrating 5° to the right of the direction up the sawteeth and a cell moving 5° to the left of the direction up the sawteeth would both be described as migrating at 5° relative to the sawtooth orientation. The alignment and eccentricity of cells were calculated as described previously (*86*). We calculated the cell orientation, which ranges from 0° to 360°, from the cell alignment, which ranges from 0° to 180°, using the direction of cellular motion. From the two possible orientations that correspond to each alignment, the orientation was chosen that was closest to the direction of the cell. Additionally, all quartile plots were scaled so that the sum of all angular bins was unity.

4.4.4. Tracking actin polymerization

This section is contributed by Meghan Driscoll and Can Guven

In *D. discoideum* and neutrophils, actin polymerization occurs in reaction-diffusion type waves. To measure the directionality of these polymerization waves, we used a modified optical-flow algorithm. Optical-flow algorithms assign a pixel-dependent apparent velocity in an image sequence. At each pixel, our algorithm assigns a direction of actin-wave polymerization and a quantity of newly polymerized

actin. Although the algorithm does not track stationary actin foci, stationary regions of actin polymerization are included in the unit-cell analysis described below.

To adjust for differences in protein expression levels from cell to cell, all *D. discoideum* and neutrophil images were gamma corrected using a gamma of 0.5 prior to calculating the difference images. To track actin polymerization across a pair of subsequent frames, f_t and f_{t+1}, we first found the difference image $f_{t+1} - f_t$. Then, to reduce noise, the difference image was smoothed with a Gaussian filter of standard deviation 3 pixels for *D. discoideum* and 1 pixel for neutrophils. Intensity values in our images ranged from 0 to 255. For further noise reduction, a lower threshold of 43 was applied for *D. discoideum* and 24 for neutrophils. Different parameters were used for the analysis of *D. discoideum* and neutrophils, because these cell types migrate at different speeds and were imaged at different resolutions. The intensity of each pixel in this difference image was assumed to be proportional to the amount of newly polymerized actin. To associate a direction with the newly polymerized actin at each pixel, an actin polymerization wave was assumed to be most likely to come from the direction of greatest newly polymerized actin in the previous difference image. Similarly, it is expected that the newly polymerized actin is most likely to travel towards the direction of greatest newly polymerized actin in the future difference image. Therefore, the previous difference image, $f_t - f_{t-1}$, and the future difference image, $f_{t+2} - f_{t+1}$, were then found. Both difference images were then smoothed with Gaussian filters of standard deviation 5 pixels for *D. discoideum* and 3 pixels for neutrophils. This smoothing step spreads information about the previous and future newly polymerized actin to the location of the newly polymerized actin in the current

difference image. The standard deviation of the filter in this smoothing determines the speed of the fastest actin wave that can be tracked by the algorithm. In addition to reducing noise, the first smoothing and the lower threshold described above determine the speed of the slowest actin wave that can be tracked by the algorithm. Finally, we associated a direction with the newly polymerized actin by subtracting the normalized gradient of the previous difference image from the normalized gradient of the future difference image.

4.4.5. Averaged actin flux analysis

This section is contributed by Meghan Driscoll and Can Guven

We measured the mean actin fluorescence and actin flux around a sawtooth by averaging across the sawteeth in a movie. To locate the sawteeth, cells were imaged simultaneously in fluorescence and bright-field modes. The sawtooth orientation, ridge spacing, and sawtooth length were measured in each bright-field image. First, a Radon transform (*107*) with an angular step size of 0.1 degrees was used to find the sawtooth orientation. Each bright-field image was then rotated such that the sawteeth were aligned horizontally. The image edges were discarded, because they exhibit interpolation artifacts due to the rotation. Next, each image was projected onto the vertical and horizontal axes. To measure the ridge spacing and sawtooth length to sub-pixel accuracy, each projection was interpolated using a cubic spline with a spacing of 0.1 pixels. The spacing and pitch were then measured from the auto-

correlations of the splines. The spacing was measured from the vertical projection, which is in the direction perpendicular to the ridges, and the pitch was measured from the horizontal projection, which is in the direction parallel to the ridges.

The actin fluorescence intensity and actin flux were next averaged across all of the sawteeth. Each fluorescence image was rotated so that the sawteeth were horizontal. The actin-flux measure was similarly rotated, as was the angle of the vectors within the field. Next, the images were enlarged using a bilinear interpolation, such that the ridge spacing and sawtooth length would be of the next greatest integer size. For instance, if the ridge spacing were 26.8 pixels, then the corresponding dimension of the image would be enlarged by the factor 27/26.8. Forcing the ridge spacing and sawtooth length to have integer dimensions allows for simple averaging across multiple sawteeth. Within each image, the averages of the measures around each sawtooth were next found by tiling the image into sub-images of sawtooth size and averaging across the sub-images. The mean measures were averaged across images by using the positions of the sawteeth tips in the bright-field images as a guide. To align the sawteeth to subpixel scale, all of the averaged measures were first enlarged by a factor of eight. The bright-field averaged image was then blurred using a Gaussian filter with a standard deviation of 16 pixels. Next, the sawtooth tip was found in the direction parallel to the ridges by finding the row with the greatest standard deviation in bright-field intensity. The position of the tip parallel to the ridges was then found as the position with the greatest bright field intensity along the ridge. After centering, the mean measures were shrunk by a factor of eight and then averaged across all frames.

4.4.6. Measuring actin wave speed

The actin-wave propagation speed in neutrophils (Figures 4.7E and G) was measured using space/time plots (Figure 4.11). An actin wave traveling along a single ridge was cropped and resized into a single-pixel width using the ImageJ software package (NIH) (*83*). The same processing was repeated on every cropped image in the time-lapse series. The resized actin waves were montaged into a space/time plot. Actin-wave propagation speed was obtained by dividing the distance that the wave front traveled by the time lapse. More than 60 individual speeds were measured on each type of nanosawtooth surface.

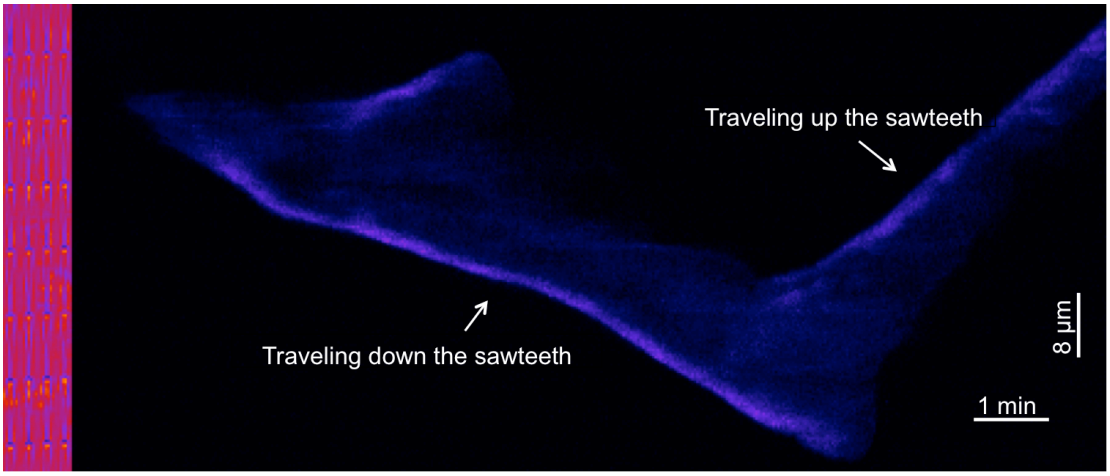

Figure 4.11. Space/time plot of a resized actin wave traveling along a single ridge. The bright-field image on the left shows the orientation of the sawteeth. The speeds of actin waves traveling up and down the nanosawteeth measured in this space/time plot are 7.3 µm/min and 4.5 µm/min, respectively.

Chapter 5: Concentric Nanorings Promote Counterclockwise Actin Wave Propagation and Cell Motion via Intrinsic Cytoskeletal Chirality

5.1. Introduction

Left-right asymmetry is a ubiquitous biological property that is well-conserved across species. Such asymmetry has been seen in climbing plants (*108*), helices of snail shells (*109*), directional rotation of the hindgut epithelial tube (*110*), placement of viscera in human body (*111*), *etc*. It has been demonstrated that laterality is established during the early cleaving stage of embryo development (*112, 113*), and that disruption in the left-right asymmetry results in birth defects and disease. However, the mechanism of the initial left-right symmetry breaking remains unclear. Among all of the mechanisms that have been proposed, the one that involves cytoskeletal proteins and their associated proteins is intriguing due to the intrinsic chirality of those molecules. Levin and coworkers have proposed a model that considers the cytoskeletal chirality to elucidate the establishment of laterality in multicellular organisms (*114, 115*). In this model, a chiral cytoskeleton orients the left-right axis with respect to the anterior-posterior and dorso-ventral axes, and actively directs the asymmetric intracellular localization of proteins in the embryo during the early cleavage stage. This model therefore suggests that the initial left-

right symmetry breaking during embryo development may arise from the chirality of the cytoskeleton.

As a major component of the cytoskeleton, actin has been studied in the establishment of embryonic laterality and cellular chirality. It has been shown that in cleaving *Xenopus* embryos, long actin fibers generate large-scale torsion, causing the cortex of the animal hemisphere to twist in a consistent counterclockwise (CCW) direction (*116*). Vunjak-Novakovic and coworkers found that cells plated on 2D micropatterns form an invariant chiral alignment upon reaching confluency, and that depolymerizing F-actin switches the chirality of the cells (*101*). In addition to the actin-related cellular chirality observed in multicellular systems, single-cell chirality has recently been demonstrated. Bershadsky and coworkers showed that the radially symmetric actin bundles in individual fibroblasts tend to tilt in a particular direction, breaking the cellular symmetry by self-organizing into linear actin arrays (Figure 5.1) (*100*). Together, these findings suggest that actin polymerization may provide potential built-in machinery that leads to cellular chirality.

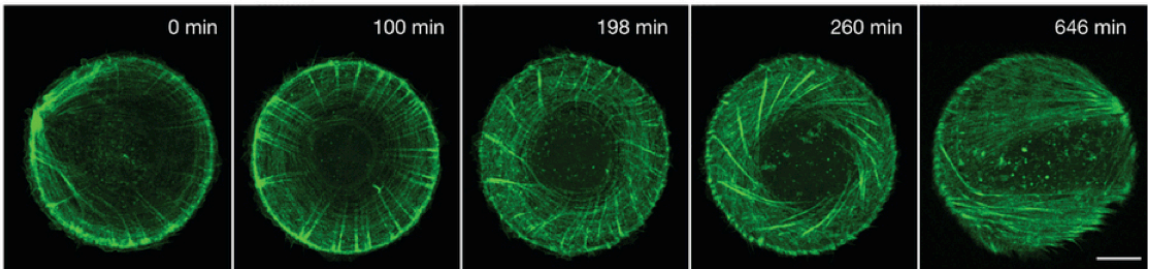

Figure 5.1. A typical example of the dynamic self-organization of the actin cytoskeleton that breaks the cellular symmetry (*100*). Scale bar, 10 μm.

Another cytoskeletal component, microtubules, has been investigated in relation to cell polarity. Because the microtubule organizing center (MTOC) is asymmetric, it could serve to amplify subcellular asymmetry to cell-level asymmetry. Neutrophils were shown to polarize preferentially to the left of an arrow pointing from the center of the nucleus to the MTOC (*117*). This leftward bias is abolished if the microtubule is depolymerized. This finding suggests that intrinsic cellular chirality may be a property of all MTOC-containing cells.

We previously showed that actin polymerizes into helical (chiral) waves in *D. discoideum* that travel through the gaps between adjacent ridges, and discussed the possibility of biasing the chirality of the helical waves, and even cell motion, by bending the helical waves via curved ridges (see Section 3.2.3). In this chapter, I will discuss the effect of concentric nanorings on actin-wave propagation and cell motion of *D. discoideum* and neutrophils in details. The polarity of neutrophils on concentric nanorings is investigated through staining of the microtubules, F-actin and nuclei of the fixed cells.

5.2. Results and Discussion

5.2.1. Nanorings exert spacing-, curvature-, and height-dependent counterclockwise (CCW) guidance on actin waves and cell motion

We studied Lifeact/*aca*$^{-}$ *D. discoideum* cells on sets of concentric nanorings that were spaced 0.8 μm and 2 μm apart, respectively. We found that on both sets of nanorings, cells migrate along the rings; actin waves also exhibit coupled dynamics

along the curved ridges. Additionally, cells tend to migrate in the CCW direction on 0.8-μm-spaced nanorings (Figure 5.2), but not 2-μm-spaced nanorings. This spacing-dependent unidirectional guidance may stem from the different morphological dynamics of actin waves on 0.8- and 2-μm-spaced rings. Because each ring is 300 nm wide, the gap between adjacent 0.8-μm-spaced rings is 500 nm wide. As discussed in Chapter 3, the formation of helical actin waves is prohibited in such narrow gaps due to the confinement. Therefore, a torque may build up as the actin wave propagates along the gap. If the chirality of the wave propagating in the clockwise (CW) direction is opposite to that of the wave propagating in the CCW direction, bending the waves with rings may relax the torque in waves with one type of chirality but accumulate the torque in waves with the other, leading to a biased CW or CCW cell motion, as observed on 0.8-μm-spaced rings. In contrast, helical actin waves do form on 2-μm-spaced rings. If the actin streaks adhering to the opposite sides of a single ridge transform into helical waves with opposite handedness, as indicated in Figure 3.6C, bending the waves with rings has the same effect on actin waves traveling in the CW and CCW directions, leading to the equal probability of cell motion in both directions.

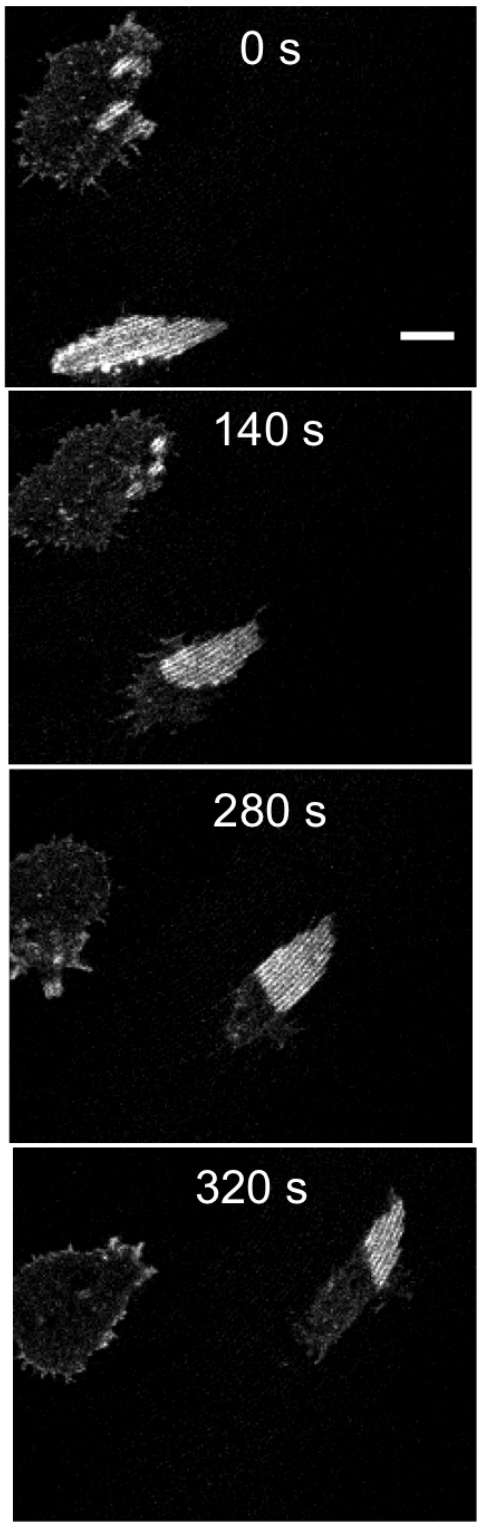

Figure 5.2. A typical example of actin waves that propagate persistently in the CCW direction in a *D. discoideum* cell. Scale bar, 8 μm.

We also investigated the effects of nanorings on actin-YFP neutrophils that were stimulated with extraneous f-Met-Leu-Phe (fMLP) with a uniform concentration of 100 nM. We found a CCW bias of both cell motion and actin-wave propagation on nanorings with a spacing of 2 μm, a height of 1 μm, and a radius of 50 to 90 μm (Figure 5.3). Cells tend to migrate persistently on rings within such a radius range. However, cells that migrate on rings with a radius larger than 100 μm often switch directions, and tend to migrate more in the radial direction than do cells that migrate on smaller rings. We did not observe helical actin waves in neutrophils. Therefore, the ultrastructure of actin architecture in neutrophils may differ from that in *D. discoideum*, presumably resulting in a different effect of 2-μm-spaced nanorings on cell motion. On the other hand, neutrophils form focal adhesions on the surface, requiring various surface-adhesion molecules to be expressed. It has been shown that formin, a protein that regulates actin polymerization, caps and immobilizes the barbed end of F-actin at peripheral focal adhesions in fibroblasts (*100*). As actin polymerizes, the filaments rotate unidirectionally relative to the formin. A similar event could occur in neutrophils. Actin waves propagating in the CCW direction may release the torsional strain, leading to a CCW bias in cell motion.

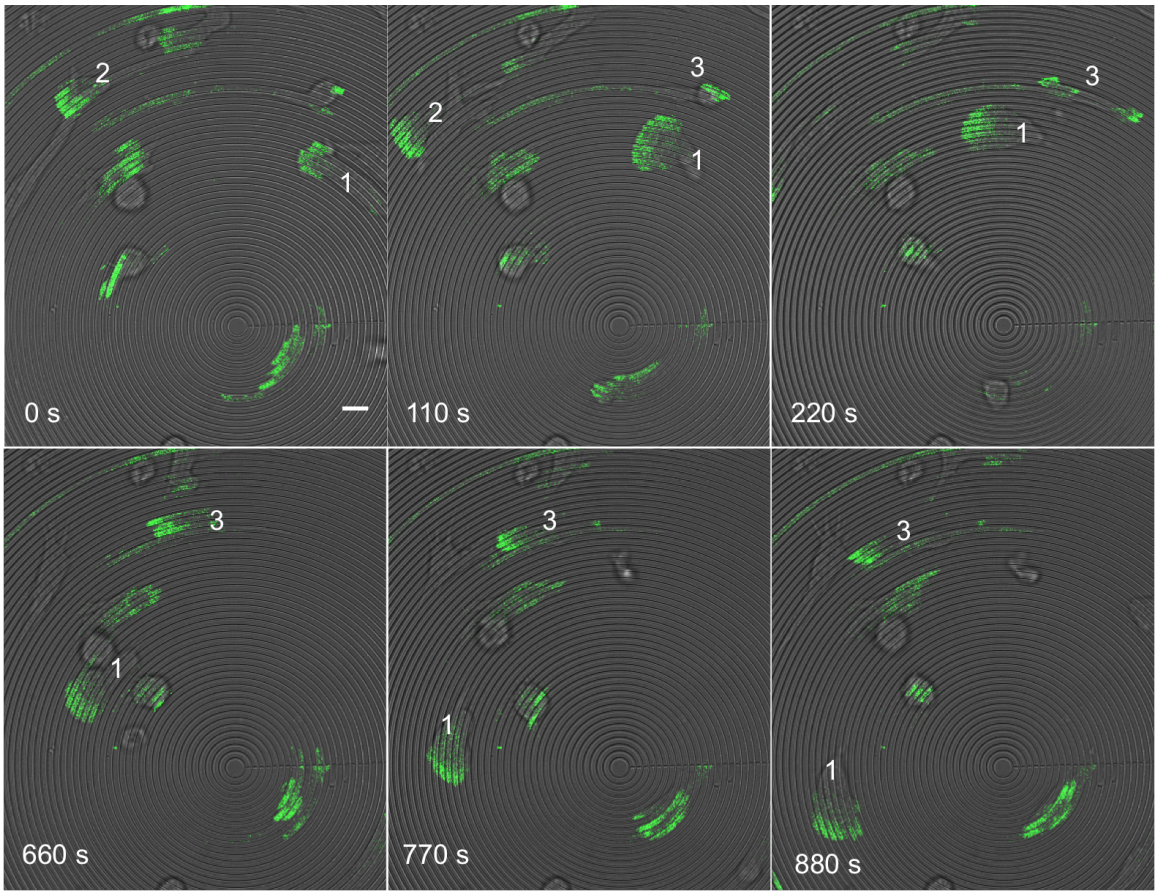

Figure 5.3. Series of time lapse snapshots showing the CCW cell motion and actin wave propagation in neutrophils on 2-μm-spaced, 1-μm-high nanorings. The concentric nanorings were imaged in the bright-field channel. Actin waves were imaged in the fluorescence channel. The same cells are marked with the same number. Scale bar, 8 μm.

Additionally, neutrophils can spread and migrate persistently on nanorings even without the stimulation of fMLP (Figure 5.4), indicating that fibronectin-coated nanotopographies alone can stimulate and activate neutrophils. The details of

activating intracellular signaling pathways with nanotopographies require further investigation.

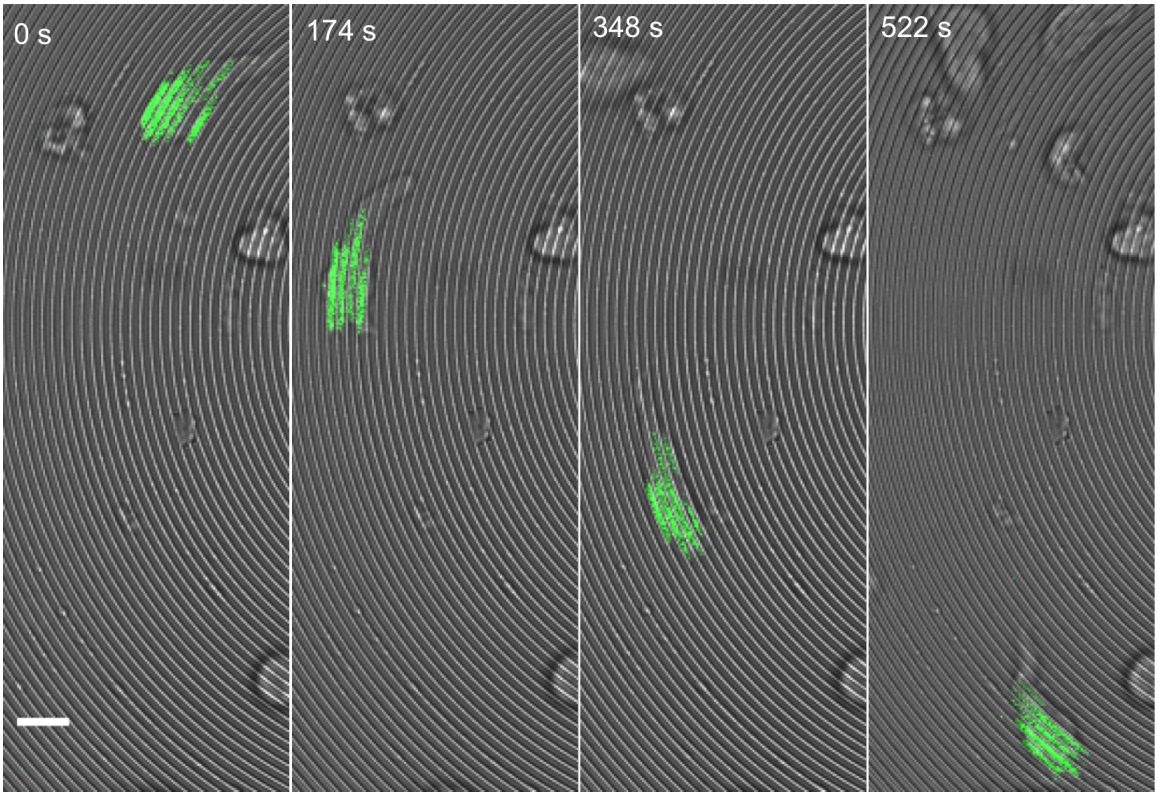

Figure 5.4. A typical example of a neutrophil that migrates persistently on concentric nanorings without being stimulated with fMLP. Scale bar, 8 μm.

To assess the effect of ring height on the CCW guidance efficiency, we also studied neutrophils on nanorings with a spacing of 2 μm and a height of 2 μm. However, we did not observe an apparent CCW bias in either cell motion or actin-wave propagation. In contrast to *D. discoideum*, the migration direction of which is independent of the position of the MTOC (*118*), the migration direction of neutrophils is related to the asymmetric distribution of microtubules, which is

determined by the position of the MTOC relative to the nucleus (*117, 119, 120*). Because the MTOC does not always locate on the bottom of the cell, taller rings are more likely to interact with or confine the MTOC (Figure 5.5), and thus affect its position in the cell. The effects of nanorings on the position of the MTOC and the polarity of neutrophils will be discussed in detail in the following section.

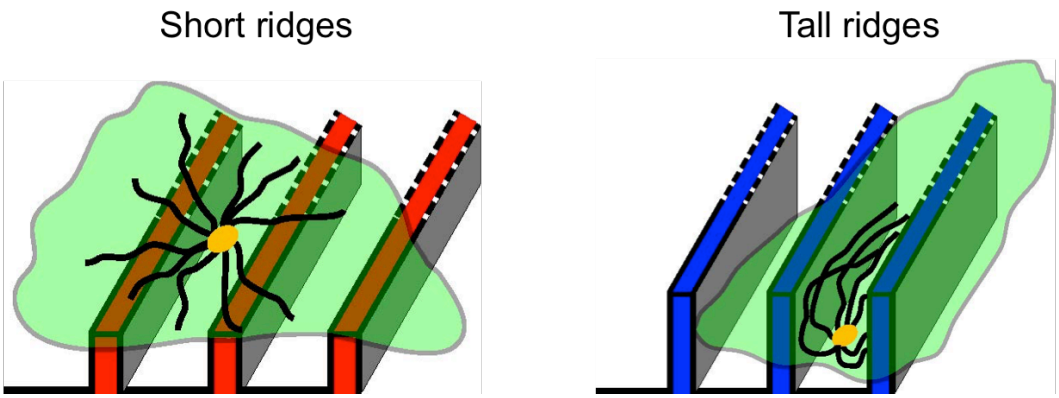

Figure 5.5. A schematic showing the possible effect of ridge height on MTOC and microtubules. Tall ridges are more likely to confine the MTOC within the gaps than short ridges.

5.2.2. Neutrophils exhibit ring-height-dependent CCW polarization on nanorings

We assessed the polarity of neutrophils on 2-μm-spaced nanorings with a height of 1 μm and 2 μm, respectively, by staining F-actin, microtubules and nuclei (Figure 5.6). In a polarized neutrophil migrating on a 2D surface, the nucleus is located right behind the actin network in the lamellipodia, whereas the MTOC is located behind the nucleus, extending microtubules predominantly directed towards the back of the

cell (*120*). Therefore, the direction of neutrophil polarization can be inferred from the position of the MTOC relative to the nucleus. We observed a higher CCW to CW polarization ratio in neutrophils on rings with a height of 1 μm than on ones with a height of 2 μm (Figure 5.6). This result corresponds to our observations on cell migration. It has been demonstrated that microtubules are coupled to retrograde actin flow and to anterograde actin motion (*121*), and that microtubules also grow along actin bundles (*122*). Therefore, the microtubule actin interaction could alter the actin architecture and affect its chirality. Because the microtubule disassembly has been shown to induce a polarized distribution of F-actin in neutrophils (*123*), it is worthwhile to compare the actin-wave propagation in microtubule-disrupted neutrophils on nanorings with different heights, and to assess whether the CCW bias could be enhanced in neutrophils migrating on 1-μm-high nanorings and restored in neutrophils migrating on 2-μm-high nanorings.

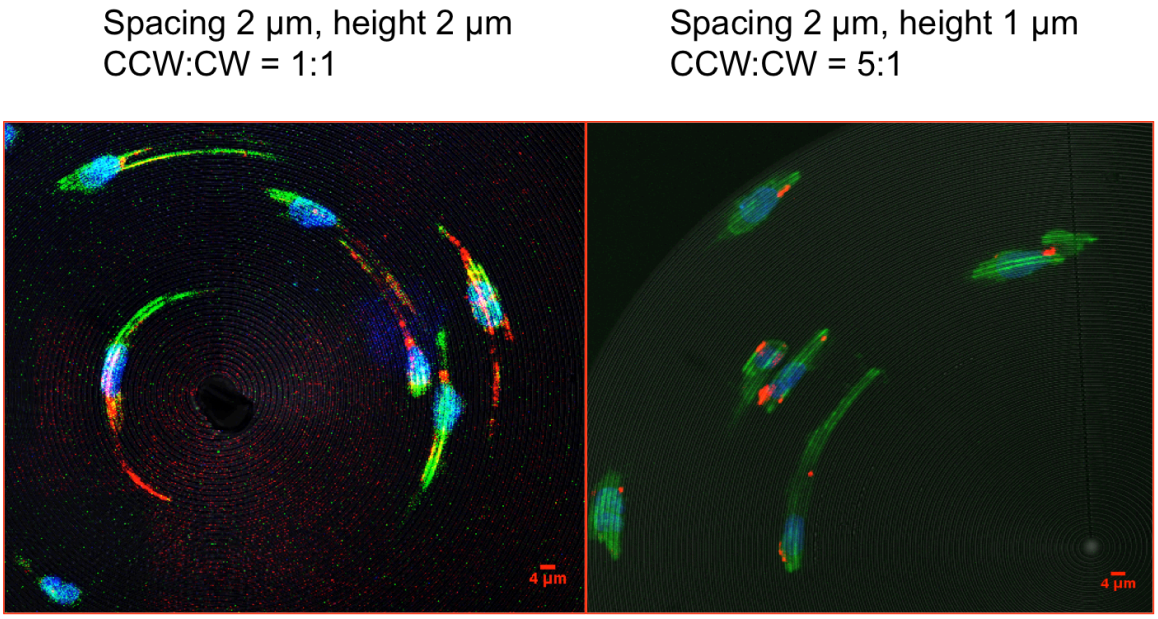

Figure 5.6. Neutrophils exhibit a CCW-biased polarization on 1-μm-high rings, but not on 2-μm-high rings. Green: F-actin. Red: microtubules. Blue: nuclei. Scale bars, 4 μm.

5.3. Summary

We demonstrated that unidirectional bias in actin-wave propagation and cell motion can be induced by symmetric nanotopography, such as concentric nanorings. The observed unidirectional bias presumably results from the effects of the nanorings on the cytoskeletal chirality. *D. discoideum* tends to migrate in the CCW direction on 0.8-μm-spaced rings, but not on 2-μm-spaced rings. We speculated that this spacing-dependent CCW guidance is related to morphological dynamics of actin waves. Because the formation of helical actin waves is prohibited on 0.8-μm-spaced nanorings, a torsional strain may accumulate in the linear actin waves. Waves that

travel in the CCW direction could relax the strain, leading to a biased, CCW cell motion. Nanorings with a spacing of 2 μm and a height of 1 μm exhibit CCW guidance of neutrophils, indicating that the ultrastructure of the actin network in neutrophils is different from that in *D. discoideum*. This CCW guidance is also curvature-dependent. Neutrophils migrating on larger rings are less persistent in their migration direction and tend to migrate more radially compared with those migrating on smaller rings. A CCW-biased cell polarization is also observed in the fixed neutrophils on the same nanorings. However, neither cell motion nor cell polarization exhibit CCW bias in neutrophils on nanorings with 2-μm spacing and 2-μm height, suggesting that taller nanorings may affect the position and activity of the MTOC, which eventually affects the ultrastructure of actin network through the microtubule-actin interaction.

5.4. Outlook

Because the CCW bias that we observe in *D. discoideum* and neutrophils on nanorings is spacing-, height-, and curvature-dependent, it is important to evaluate the guidance efficiency on nanorings with a systematically varying spacing and height. To test our hypothesis that the confinement of actin waves on 0.8-μm-spaced rings leads to the CCW bias, concentric rings composed of 500-nm-wide nanogrooves need to be employed to study their effects on actin-wave propagation and cell motion. The optimum curvature for CCW guidance can be obtained by establishing a relationship between guidance efficiency and ring curvature. A fish-scale pattern composed of

repeating arches with the optimum curvature, spacing and height, as shown in Figure 5.7, can be used to guide cell motion unidirectionally. Structured-illumination microscopy can be employed to investigate the actin-wave dynamics on nanorings with a higher temporal and spatial resolution. It is also worthwhile to image the ultrastructure of actin networks in cells on nanorings by cryo-electron microscopy, which provides molecular-scale resolution and will directly reveal the effects of bending or confinement on the detailed structure or chirality of the actin architecture.

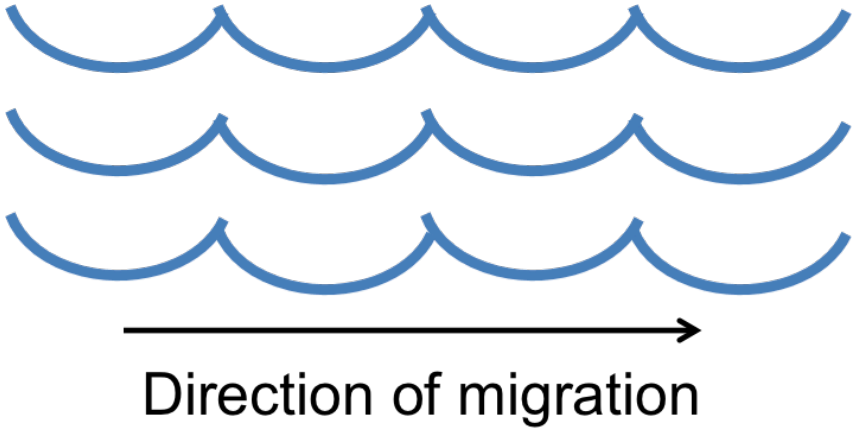

Figure 5.7. A schematic showing the design of the fish scale pattern.

The directions of both cell motion and cell polarization in neutrophils on nanorings depend on the ring height, suggesting that the MTOC and microtubules may interact with actin network, or act in a competing mechanism against the CCW bias induced by actin waves. Depolymerizing microtubules or imaging their dynamics directly in neutrophils on nanorings will provide more insights on the role of microtubules in contact guidance.

5.5. Materials and Methods

5.5.1. Neutrophil fixation

The culturing and development of neutrophils have been described in Chapter 4. After development, cells were plated on the nanoring surface coated with 1 μg/mL fibronectin, stimulated with extraneous f-Met-Leu-Phe (fMLP) with a uniform concentration of 100 nM in mHBSS, and incubated at 37 °C for 10 min. Cells were fixed with 6.4% paraformaldehyde, 0.05% glutaraldehyde, and 0.125-mg/ml saponin in PBS for 5 min, and subsequently washed three times with PBS. Cells were then treated with 10% heat-inactivated fetal calf serum and 0.125-mg/ml saponin in blocking buffer at 37 °C for 30 min, and again washed three times with PBS.

5.5.2. Staining for F-actin, microtubules and nuclei

Cells were incubated with primary alpha-tubulin antibody (1:200 dilution in blocking buffer) at 37 °C for 1 h, Alexa Fluor 488 secondary antibody (1:200 dilution in blocking buffer) at 37 °C for 30 min, phalloidin-tetramethylrhodamine (phalloidin-TRITC) (1:500 dilution in blocking buffer) for 30 min at room temperature, and DAPI (4',6-diamidino-2-phenylindole) for 10 min at room temperature. Cells were washed with mHBSS for three times between each staining step and imaged in mHBSS. Fluorescence images were obtained on a Leica SP5 X confocal microscope.

Chapter 6: Summary

This thesis has discussed cellular contact guidance through dynamic sensing of nanotopographies via actin polymerization waves. Cell migration is a critical physiological process that originates from the actin polymerization in the front of a cell and actomyosin contraction in the back of a cell. Most of the studies in the field of cell migration have focused on the intracellular signaling pathways that are triggered by specific molecules, such as chemotaxis and haptotaxis. Because cells migrate in response to the physical geometry of their environment, which is on a length scale of tens to hundreds of nanometers, we investigated the effects of nanotopographies on actin wave propagation and cell motion. Two distinct prototypical systems for cell migration, D. discoideum and neutrophils were employed in our study, aiming to reveal the generality of the phenomenon of biasing actin waves and cell motion through nanotopography.

To investigate cell migration on diverse nanotopographies, we need to replicate the nanotopographies precisely and in a parallel manner. Solvent-assisted nanotransfer molding (nTM) is one such method, and was described in Chapter 2. The master nanotopography was fabricated via multiphoton absorption polymerization and then coated with fluorocarbon to facilitate the release in the molding process. A low-viscosity solvent was added to the h-PDMS prepolymer to improve the fluidity and conformability, which allows for a high molding resolution. Nanogrooves–the complementary topographies of nanoridges–were replicated

through a double-molding process. The molding of nanograss indicates that the resolution of solvent-assisted nTM is approximately 30 nm. For further improvement on the molding resolution, the formulation and curing condition of the h-PDMS prepolymer need to be optimized. A different fluorocarbon with a shorter chain length can be used if the length scale of the features to be molded is approaching the molecular scale. The nanotopographies can be functionalized with proteins through Michael addition if the acrylic resin is partially cured. All of the surfaces for studying neutrophils were coated with fibronectin by such a method.

In Chapter 3, I discussed the effect of nanoridges/nanogrooves on the actin waves in *D. discoideum*. Both cell motion and actin wave propagation are bidirectionally guided along the nanoridges/nanogrooves. Actin preferentially polymerizes around individual ridges. The actin streaks that adhere to the opposite sides of a single nanoridge exhibit couple dynamics, whereas actin streaks in nanogrooves separated by microridges travel independently. Actin waves travel at a speed of 20 to 35 μm/min. The guidance efficiency of actin waves depends on the ridge spacing. Actin waves on nanoridges with a small spacing (0.8 μm and 1.5 μm) are confined to travel along the ridges. In contrast, actin waves on nanoridges with a large spacing (3 μm) are more dispersive and transform into circular waves upon reaching the flat area between adjacent ridges. Actin streaks that initially adhere to the sides of the nanoridges can transform into helical waves that propagate through the gaps between the 1.5- to 2-μm-spaced nanoridges. However, due to the confinement in nanogrooves, actin polymerizes in linear waves. A transition between static and traveling actin waves was observed on nanodots that are connected with

nanoridges. Super-resolution microscopy, such as structured illumination microscopy, is required to image the structural and dynamic details of the helical actin waves, as well as to elucidate the mechanism of the transition between static and traveling actin waves.

Unidirectional guidance of cell motion is usually achieved by actively imposing a global spatial gradient to cells. However, guidance over large distance is limited by the finite dynamic range of cellular sensing. In Chapter 4, I discussed the unidirectional cell guidance via biasing the actin-wave dynamics using asymmetric nanosawteeth. In this method, cells passively conform to the nanosawteeth in the absence of a global gradient. We found that *D. discoideum* cells tend to migrate up the slope on 8-μm sawteeth but down the slope on 2-μm sawteeth. The actin flux analysis shows that actin waves are guided in the same direction as cell motion, and are more strongly biased. Neutrophils are also guided up the slope on 8-μm sawteeth, with the actin waves that propagate up the sawteeth traveling faster than those that propagate down the sawteeth. Separated nanosawteeth guide actin waves unidirectionally, but not cell motion. Together, the details of nanotopographies are crucial to induce unidirectional guidance on cell motion. For future application, nanosawteeth can be incorporated into microfluidic devices to provide long-distance unidirectional guidance on cell motion without a chemical gradient.

F-actin is intrinsically a right-handed helix. Bending F-actin causes the helix to twist or untwist, and thus leads to an enhanced or reduced actin polymerization based on the stability of the modified F-actin conformation. Therefore, it is possible to bias

the direction of cell motion via the intrinsic cytoskeletal chirality using symmetric nanotopographies. Chapter 5 focused on inducing biased actin-wave propagation and cell motion with concentric nanorings. We observed a CCW bias in *D. discoideum* migrating on 0.8-μm-spaced rings, but not on 2-μm-spaced rings. This spacing-dependent CCW guidance is speculated to be related to the morphology of actin waves. Due to the confinement between the adjacent 0.8-μm-spaced rings, the formation of helical actin waves is prohibited, resulting in a torque accumulated in the linear actin waves. Linear waves that propagate in the CCW direction may release the torque and thus enhance the actin polymerization. Neutrophils exhibit a CCW bias on nanorings that are 2-μm-spaced and 1-μm-high. The directions of both cell motion and cell polarization are sensitive to the height of the nanorings. Super-resolution microscopy will allow for the investigation of the dynamics and ultrastructure of the actin architecture in more detail.

Bibliography

1. A. J. Ridley, M. A. Schwartz, K. Burridge, R. A. Firtel, M. H. Ginsberg, G. Borisy, J. T. Parsons, A. R. Horwitz, Cell migration: integrating signals from front to back. *Science* **302**, 1704-1709 (2003).
2. M. Doitsidou, M. Reichman-Fried, J. Stebler, M. Köprunner, J. Dörries, D. Meyer, C. V. Esguerra, T. Leung, E. Raz, Guidance of Primordial Germ Cell Migration by the Chemokine SDF-1. *Cell* **111**, 647-659 (2002).
3. R. Farooqui, G. Fenteany, Multiple rows of cells behind an epithelial wound edge extend cryptic lamellipodia to collectively drive cell-sheet movement. *Journal of Cell Science* **118**, 51-63 (2005).
4. Y. Ding, J. Xu, J. S. Bromberg, Regulatory T cell migration during an immune response. *Trends in immunology* **33**, 174-180 (2012).
5. Y.-K. Seo, H.-H. Yoon, K.-Y. Song, S.-Y. Kwon, H.-S. Lee, Y.-S. Park, J.-K. Park, Increase in cell migration and angiogenesis in a composite silk scaffold for tissue-engineered ligaments. *Journal of Orthopaedic Research* **27**, 495-503 (2009).
6. P. S. Ciano, R. B. Colvin, A. M. Dvorak, J. McDonagh, H. F. Dvorak, Macrophage migration in fibrin gel matrices. *Laboratory investigation; a journal of technical methods and pathology* **54**, 62-70 (1986).
7. P. V. Afonso, M. Janka-Junttila, Young J. Lee, Colin P. McCann, Charlotte M. Oliver, Khaled A. Aamer, W. Losert, Marcus T. Cicerone, Carole A. Parent, LTB4 Is a Signal-Relay Molecule during Neutrophil Chemotaxis. *Developmental Cell* **22**, 1079-1091 (2012).
8. P. W. Kriebel, V. A. Barr, C. A. Parent, Adenylyl cyclase localization regulates streaming during chemotaxis. *Cell* **112**, 549-560 (2003).
9. M. L. Rachel, H. K. Douglas, N. N. Kerstin, T. O. Nicholas, L. Wolfgang, Quantifying stretching and rearrangement in epithelial sheet migration. *New Journal of Physics* **15**, 025036 (2013).
10. D. A. Lauffenburger, A. F. Horwitz, Cell migration: a physically integrated molecular process. *Cell* **84**, 359-369 (1996).
11. D. J. Tschumperlin, Fibroblasts and the Ground They Walk On. *Physiology* **28**, 380-390 (2013).
12. E. Sahai, C. J. Marshall, Differing modes of tumour cell invasion have distinct requirements for Rho/ROCK signalling and extracellular proteolysis. *Nature Cell Biology* **5**, 711-719 (2003).
13. T. Lammermann, M. Sixt, Mechanical modes of 'amoeboid' cell migration. *Current Opinion in Cell Biology* **21**, 636-644 (2009).
14. C. A. Parent, P. N. Devreotes, A Cell's Sense of Direction. *Science* **284**, 765-770 (1999).
15. C. P. McCann, P. W. Kriebel, C. A. Parent, W. Losert, Cell speed, persistence and information transmission during signal relay and collective migration. *Journal of Cell Science* **123**, 1724-1731 (2010).
16. C.-M. Lo, H.-B. Wang, M. Dembo, Y.-l. Wang, Cell Movement Is Guided by the Rigidity of the Substrate. *Biophysical Journal* **79**, 144-152 (2000).

17. G. Tai, B. Reid, L. Cao, M. Zhao, in *Chemotaxis Methods and Protocols,* T. Jin, D. Hereld, Eds. (Humana Press, 2009), vol. 571, chap. 5, pp. 77-97.
18. B. Cortese, I. E. Palama, S. D'Amone, G. Gigli, Influence of electrotaxis on cell behaviour. *Integrative Biology* **6**, 817-830 (2014).
19. S. Cattaruzza, R. Perris, Proteoglycan control of cell movement during wound healing and cancer spreading. *Matrix Biology* **24**, 400-417 (2005).
20. E. Decave, D. Garrivier, Y. Brechet, B. Fourcade, F. Bruckert, Shear flow-induced detachment kinetics of Dictyostelium discoideum cells from solid substrate. *Biophysical Journal* **82**, 2383-2395 (2002).
21. E. Decave, D. Rieu, J. Dalous, S. Fache, Y. Brechet, B. Fourcade, M. Satre, F. Bruckert, Shear flow-induced motility of Dictyostelium discoideum cells on solid substrate. *Journal of Cell Science* **116**, 4331-4343 (2003).
22. P. Provenzano, K. Eliceiri, J. Campbell, D. Inman, J. White, P. Keely, Collagen reorganization at the tumor-stromal interface facilitates local invasion. *BMC Medicine* **4**, 38 (2006).
23. P. Weiss, Nerve regeneration in the rat following tubular splicing of severed nerves. *Archives of Surgery* **46**, 525-547 (1943).
24. P. Weiss, Experiments on cell and axon orientation in vitro: The role of colloidal exudates in tissue organization. *Journal of Experimental Zoology* **100**, 353-386 (1945).
25. A. S. G. Curtis, M. Varde, Control of Cell Behavior: Topological Factors. *Journal of the National Cancer Institute* **33**, 15-26 (1964).
26. G. A. Dunn, J. P. Heath, A new hypothesis of contact guidance in tissue cells. *Experimental Cell Research* **101**, 1-14 (1976).
27. B. S. Eckert, R. H. Warren, R. W. Rubin, Structural and Biochemical Aspects of Cell Motility in Amebas of Dictyostelium discoideum. *The Journal of Cell Biology* **72**, 339-350 (1977).
28. A. Wood, Contact guidance on microfabricated substrata: the response of teleost fin mesenchyme cells to repeating topographical patterns. *Journal of Cell Science* **90**, 667-681 (1988).
29. X. F. Walboomers, H. J. E. Croes, L. A. Ginsel, J. A. Jansen, Growth behavior of fibroblasts on microgrooved polystyrene. *Biomaterials* **19**, 1861-1868 (1998).
30. K. A. Diehl, J. D. Foley, P. F. Nealey, C. J. Murphy, Nanoscale topography modulates corneal epithelial cell migration. *Journal of Biomedical Materials Research Part A* **75A**, 603-611 (2005).
31. P. Clark, P. Connolly, A. S. Curtis, J. A. Dow, C. D. Wilkinson, Cell guidance by ultrafine topography in vitro. *Journal of Cell Science* **99**, 73-77 (1991).
32. C. D. W. Wilkinson, M. Riehle, M. Wood, J. Gallagher, A. S. G. Curtis, The use of materials patterned on a nano- and micro-metric scale in cellular engineering. *Materials Science and Engineering: C* **19**, 263-269 (2002).
33. S. Ber, G. Torun Köse, V. HasIrcI, Bone tissue engineering on patterned collagen films: an in vitro study. *Biomaterials* **26**, 1977-1986 (2005).
34. A. I. Teixeira, G. A. Abrams, P. J. Bertics, C. J. Murphy, P. F. Nealey, Epithelial contact guidance on well-defined micro- and nanostructured substrates. *Journal of Cell Science* **116**, 1881-1892 (2003).

35. W. A. Loesberg, J. te Riet, F. C. M. J. M. van Delft, P. Schön, C. G. Figdor, S. Speller, J. J. W. A. van Loon, X. F. Walboomers, J. A. Jansen, The threshold at which substrate nanogroove dimensions may influence fibroblast alignment and adhesion. *Biomaterials* **28**, 3944-3951 (2007).
36. F. Amyot, A. Small, H. Boukari, D. Sackett, J. Elliott, D. McDaniel, A. Plant, A. Gandjbakhche, Thin films of oriented collagen fibrils for cell motility studies. *Journal of Biomedical Materials Research Part B: Applied Biomaterials* **86B**, 438-443 (2008).
37. H. L. Khor, Y. Kuan, H. Kukula, K. Tamada, W. Knoll, M. Moeller, D. W. Hutmacher, Response of Cells on Surface-Induced Nanopatterns:â€‰ Fibroblasts and Mesenchymal Progenitor Cells. *Biomacromolecules* **8**, 1530-1540 (2007).
38. M. T. Eliason, E. O. Sunden, A. H. Cannon, S. Graham, A. J. García, W. P. King, Polymer cell culture substrates with micropatterned carbon nanotubes. *Journal of Biomedical Materials Research Part A* **86A**, 996-1001 (2008).
39. A. D. Doyle, F. W. Wang, K. Matsumoto, K. M. Yamada, One-dimensional topography underlies three-dimensional fibrillar cell migration. *Journal of Cell Biology* **184**, 481-490 (2009).
40. C. Y. Xu, R. Inai, M. Kotaki, S. Ramakrishna, Aligned biodegradable nanofibrous structure: a potential scaffold for blood vessel engineering. *Biomaterials* **25**, 877-886 (2004).
41. A. Disanza, A. Steffen, M. Hertzog, E. Frittoli, K. Rottner, G. Scita, in *Cellular and Molecular Life Sciences CMLS*. (Birkhäuser-Verlag, 2005), vol. 62, pp. 955-970.
42. J. A. Theriot, T. J. Mitchison, Actin microfilament dynamics in locomoting cells. *Nature* **352**, 126-131 (1991).
43. V. I. Risca, E. B. Wang, O. Chaudhuri, J. J. Chia, P. L. Geissler, D. A. Fletcher, Actin filament curvature biases branching direction. *Proceedings of the National Academy of Sciences* **109**, 2913-2918 (2012).
44. K. H. Song, S. J. Park, D. S. Kim, J. Doh, Sinusoidal wavy surfaces for curvature-guided migration of T lymphocytes. *Biomaterials* **51**, 151-160 (2015).
45. G. Gerisch, T. Bretschneider, A. Müller-Taubenberger, E. Simmeth, M. Ecke, S. Diez, K. Anderson, Mobile Actin Clusters and Traveling Waves in Cells Recovering from Actin Depolymerization. *Biophysical Journal* **87**, 3493-3503 (2004).
46. O. D. Weiner, W. A. Marganski, L. F. Wu, S. J. Altschuler, M. W. Kirschner, An actin-based wave generator organizes cell motility. *PLoS Biology* **5**, e221 (2007).
47. T. Bretschneider, S. Diez, K. Anderson, J. Heuser, M. Clarke, A. Muller-Taubenberger, J. Kohler, G. Gerisch, Dynamic actin patterns and Arp2/3 assembly at the substrate-attached surface of motile cells. *Current Biology* **14**, 1-10 (2004).
48. G. Giannone, B. J. Dubin-Thaler, H.-G. Döbereiner, N. Kieffer, A. R. Bresnick, M. P. Sheetz, Periodic Lamellipodial Contractions Correlate with Rearward Actin Waves. *Cell* **116**, 431-443 (2004).

49. T. Bretschneider, K. Anderson, M. Ecke, A. Müller-Taubenberger, B. Schroth-Diez, H. C. Ishikawa-Ankerhold, G. Gerisch, The Three-Dimensional Dynamics of Actin Waves, a Model of Cytoskeletal Self-Organization. *Biophysical journal* **96**, 2888-2900 (2009).
50. R. H. Depue, R. V. Rice, F-actin is a right-handed helix. *Journal of Molecular Biology* **12**, 302-303 (1965).
51. W. L. Zeile, F. Zhang, R. B. Dickinson, D. L. Purich, Listeria's right-handed helical rocket-tail trajectories: mechanistic implications for force generation in actin-based motility. *Cell Motility and Cytoskeleton* **60**, 121-128 (2005).
52. T. Svitkina, Imaging Cytoskeleton Components by Electron Microscopy. *Methods in molecular biology* **586**, 187-206 (2009).
53. C. P. McCann, E. C. Rericha, C. Wang, W. Losert, C. A. Parent, *Dictyostelium* Cells Migrate Similarly on Surfaces of Varying Chemical Composition. *PLoS One* **9**, e87981 (2014).
54. A. Bagorda, V. A. Mihaylov, C. A. Parent, Chemotaxis: moving forward and holding on to the past. *Thrombosis and Haemostasis* **95**, 12-21 (2006).
55. M. Brenner, S. D. Thoms, Caffeine blocks activation of cyclic AMP synthesis in Dictyostelium discoideum. *Developmental Biology* **101**, 136-146 (1984).
56. T. Bretschneider, S. Diez, K. Anderson, J. Heuser, M. Clarke, A. Müller-Taubenberger, J. Köhler, G. Gerisch, Dynamic Actin Patterns and Arp2/3 Assembly at the Substrate-Attached Surface of Motile Cells. *Current Biology* **14**, 1-10 (2004).
57. J. Riedl, A. H. Crevenna, K. Kessenbrock, J. H. Yu, D. Neukirchen, M. Bista, F. Bradke, D. Jenne, T. A. Holak, Z. Werb, M. Sixt, R. Wedlich-Soldner, Lifeact: a versatile marker to visualize F-actin. *Nat Methods* **5**, 605-607 (2008).
58. A. B. Hauert, S. Martinelli, C. Marone, V. Niggli, Differentiated HL-60 cells are a valid model system for the analysis of human neutrophil migration and chemotaxis. *The International Journal of Biochemistry & Cell Biology* **34**, 838-854 (2002).
59. Y. Xia, G. M. Whitesides, Soft Lithography. *Angewandte Chemie International Edition* **37**, 550-575 (1998).
60. H. Kang, J. Lee, J. Park, H. H. Lee, An improved method of preparing composite poly(dimethylsiloxane) moulds. *Nanotechnology* **17**, 197 (2006).
61. L. Li, R. R. Gattass, E. Gershgoren, H. Hwang, J. T. Fourkas, Achieving Î»/20 Resolution by One-Color Initiation and Deactivation of Polymerization. *Science* **324**, 910-913 (2009).
62. F. Formanek, N. Takeyasu, T. Tanaka, K. Chiyoda, A. Ishikawa, S. Kawata, Three-dimensional fabrication of metallic nanostructures over large areas by two-photon polymerization. *Optics Express* **14**, 800-809 (2006).
63. T. Tanaka, S. Kawata, Real-time observation of birefringence by laser-scanning surface plasmon resonance microscope. *Optics Express* **13**, 6905-6911 (2005).
64. S. Jeon, V. Malyarchuk, J. A. Rogers, G. P. Wiederrecht, Fabricating three-dimensional nanostructures using two photon lithography in a single exposure step. *Optics Express* **14**, 2300-2308 (2006).

65. X.-M. Duan, H.-B. Sun, S. Kawata, Microfabrication of Two and Tree Dimensional Structures by Two-Photon Polymerization. *Journal of Photopolymer Science and Technology* **17**, 393-396 (2004).
66. H. B. Sun, A. Nakamura, S. Shoji, X. M. Duan, S. Kawata, Three-Dimensional Nanonetwork Assembled in a Photopolymerized Rod Array. *Advanced Materials* **15**, 2011-2014 (2003).
67. C. N. LaFratta, T. Baldacchini, R. A. Farrer, J. T. Fourkas, M. C. Teich, B. E. A. Saleh, M. J. Naughton, Replication of Two-Photon-Polymerized Structures with Extremely High Aspect Ratios and Large Overhangs. *The Journal of Physical Chemistry B* **108**, 11256-11258 (2004).
68. C. N. LaFratta, L. Li, J. T. Fourkas, Soft-lithographic replication of 3D microstructures with closed loops. *Proceedings of the National Academy of Sciences* **103**, 8589-8594 (2006).
69. H. Schmid, B. Michel, Siloxane Polymers for High-Resolution, High-Accuracy Soft Lithography. *Macromolecules* **33**, 3042-3049 (2000).
70. M. K. Chaudhury, G. M. Whitesides, Direct measurement of interfacial interactions between semispherical lenses and flat sheets of poly(dimethylsiloxane) and their chemical derivatives. *Langmuir* **7**, 1013-1025 (1991).
71. K. M. Choi, J. A. Rogers, A photocurable poly(dimethylsiloxane) chemistry designed for soft lithographic molding and printing in the nanometer regime. *J Am Chem Soc* **125**, 4060-4061 (2003).
72. T. W. Odom, J. C. Love, D. B. Wolfe, K. E. Paul, G. M. Whitesides, Improved Pattern Transfer in Soft Lithography Using Composite Stamps. *Langmuir* **18**, 5314-5320 (2002).
73. L. Li, J. T. Fourkas, Multiphoton polymerization. *Materials Today* **10**, 30-37 (2007).
74. J. N. Lee, C. Park, G. M. Whitesides, Solvent Compatibility of Poly(dimethylsiloxane)-Based Microfluidic Devices. *Analytical Chemistry* **75**, 6544-6554 (2003).
75. G. Y. Jung, Z. Li, W. Wu, Y. Chen, D. L. Olynick, S. Y. Wang, W. M. Tong, R. S. Williams, Vapor-phase self-assembled monolayer for improved mold release in nanoimprint lithography. *Langmuir* **21**, 1158-1161 (2005).
76. Y. Xia, J. J. McClelland, R. Gupta, D. Qin, X.-M. Zhao, L. L. Sohn, R. J. Celotta, G. M. Whitesides, Replica molding using polymeric materials: A practical step toward nanomanufacturing. *Advanced Materials* **9**, 147-149 (1997).
77. B. D. Gates, G. M. Whitesides, Replication of Vertical Features Smaller than 2 nm by Soft Lithography. *Journal of the American Chemical Society* **125**, 14986-14987 (2003).
78. F. Hua, Y. Sun, A. Gaur, M. A. Meitl, L. Bilhaut, L. Rotkina, J. Wang, P. Geil, M. Shim, J. A. Rogers, A. Shim, Polymer Imprint Lithography with Molecular-Scale Resolution. *Nano Letters* **4**, 2467-2471 (2004).
79. F. Hua, A. Gaur, Y. Sun, M. Word, J. Niu, I. Adesida, M. Shim, A. Shim, J. A. Rogers, Processing dependent behavior of soft imprint lithography on the 1-10-nm scale. *Nanotechnology, IEEE Transactions on* **5**, 301-308 (2006).

80. S. Elhadj, R. M. Rioux, M. D. Dickey, J. J. DeYoreo, G. M. Whitesides, Subnanometer Replica Molding of Molecular Steps on Ionic Crystals. *Nano Letters* **10**, 4140-4145 (2010).
81. E. G. Shafrin, W. A. Zisman, Constitutive relations in the wetting of low energy surfaces and the theory of the retraction method of preparing monolayers1. *The Journal of Physical Chemistry* **64**, 519-524 (1960).
82. M. K. Bernett, W. A. Zisman, Surface properties of perfluoro acids as affected by terminal branching and chlorine substitution. *The Journal of Physical Chemistry* **71**, 2075-2082 (1967).
83. T. J. Collins, ImageJ for microscopy. *BioTechniques* **43**, 25-30 (2007).
84. A. I. Teixeira, G. A. McKie, J. D. Foley, P. J. Bertics, P. F. Nealey, C. J. Murphy, The effect of environmental factors on the response of human corneal epithelial cells to nanoscale substrate topography. *Biomaterials* **27**, 3945-3954 (2006).
85. B. Wójciak-Stothard, A. Curtis, W. Monaghan, K. Macdonald, C. Wilkinson, Guidance and Activation of Murine Macrophages by Nanometric Scale Topography. *Experimental Cell Research* **223**, 426-435 (1996).
86. M. K. Driscoll, X. Sun, C. Guven, J. T. Fourkas, W. Losert, Cellular Contact Guidance through Dynamic Sensing of Nanotopography. *ACS Nano* **8**, 3546-3555 (2014).
87. T. P. Kunzler, C. Huwiler, T. Drobek, J. Vörös, N. D. Spencer, Systematic study of osteoblast response to nanotopography by means of nanoparticle-density gradients. *Biomaterials* **28**, 5000-5006 (2007).
88. S. Britland, H. Morgan, B. Wojiak-Stodart, M. Riehle, A. Curtis, C. Wilkinson, Synergistic and Hierarchical Adhesive and Topographic Guidance of BHK Cells. *Experimental Cell Research* **228**, 313-325 (1996).
89. E. T. den Braber, J. E. de Ruijter, L. A. Ginsel, A. F. von Recum, J. A. Jansen, Orientation of ECM protein deposition, fibroblast cytoskeleton, and attachment complex components on silicone microgrooved surfaces. *Journal of Biomedical Materials Research* **40**, 291-300 (1998).
90. K. Matsuzaka, F. Walboomers, A. De Ruijter, J. A. Jansen, Effect of microgrooved poly-l-lactic (PLA) surfaces on proliferation, cytoskeletal organization, and mineralized matrix formation of rat bone marrow cells. *Clinical Oral Implants Research* **11**, 325-333 (2000).
91. E. Eisenbarth, P. Linez, V. Biehl, D. Velten, J. Breme, H. F. Hildebrand, Cell orientation and cytoskeleton organisation on ground titanium surfaces. *Biomolecular Engineering* **19**, 233-237 (2002).
92. P. Uttayarat, G. K. Toworfe, F. Dietrich, P. I. Lelkes, R. J. Composto, Topographic guidance of endothelial cells on silicone surfaces with micro- to nanogrooves: Orientation of actin filaments and focal adhesions. *Journal of Biomedical Materials Research Part A* **75A**, 668-680 (2005).
93. S. Gerecht, C. J. Bettinger, Z. Zhang, J. T. Borenstein, G. Vunjak-Novakovic, R. Langer, The effect of actin disrupting agents on contact guidance of human embryonic stem cells. *Biomaterials* **28**, 4068-4077 (2007).

94. J. Prassler, A. Murr, S. Stocker, J. Faix, J. Murphy, G. Marriott, DdLIM Is a Cytoskeleton-associated Protein Involved in the Protrusion of Lamellipodia in Dictyostelium. *Molecular Biology of the Cell* **9**, 545-559 (1998).
95. N. Schneider, I. Weber, J. Faix, J. Prassler, A. Müller-Taubenberger, J. Köhler, E. Burghardt, G. Gerisch, G. Marriott, A Lim protein involved in the progression of cytokinesis and regulation of the mitotic spindle. *Cell Motility and the Cytoskeleton* **56**, 130-139 (2003).
96. M. K. Driscoll, C. McCann, R. Kopace, T. Homan, J. T. Fourkas, C. Parent, W. Losert, Cell Shape Dynamics: From Waves to Migration. *PLoS Computational Biology* **8**, e1002392 (2012).
97. N. Leijnse, L. B. Oddershede, P. M. Bendix, Helical buckling of actin inside filopodia generates traction. *Proceedings of the National Academy of Sciences* **112**, 136-141 (2015).
98. J. W. Shaevitz, D. A. Fletcher, Curvature and torsion in growing actin networks. *Physical Biology* **5**, 026006-026006 (2008).
99. H. Kang, D. S. Perlmutter, V. B. Shenoy, J. X. Tang, Observation and kinematic description of long actin tracks induced by spherical beads. *Biophysical Journal* **99**, 2793-2802 (2010).
100. Y. H. Tee, T. Shemesh, V. Thiagarajan, R. F. Hariadi, K. L. Anderson, C. Page, N. Volkmann, D. Hanein, S. Sivaramakrishnan, M. M. Kozlov, A. D. Bershadsky, Cellular chirality arising from the self-organization of the actin cytoskeleton. *Nature Cell Biology* **17**, 445-457 (2015).
101. L. Q. Wan, K. Ronaldson, M. Park, G. Taylor, Y. Zhang, J. M. Gimble, G. Vunjak-Novakovic, Micropatterned mammalian cells exhibit phenotype-specific left-right asymmetry. *Proceedings of the National Academy of Sciences* **108**, 12295-12300 (2011).
102. S. Jordens, E. E. Riley, I. Usov, L. Isa, P. D. Olmsted, R. Mezzenga, Adsorption at liquid interfaces induces amyloid fibril bending and ring formation. *ACS Nano* **8**, 11071-11079 (2014).
103. B. Wójciak-Stothard, Z. Madeja, W. Korohoda, A. Curtis, C. Wilkinson, Activation of macrophage-like cells by multiple grooved substrata. Topographical control of cell behaviour. *Cell Biology International* **19**, 485-490 (1995).
104. J. Wang, J. W. Petefish, A. C. Hillier, I. C. Schneider, Epitaxially Grown Collagen Fibrils Reveal Diversity in Contact Guidance Behavior among Cancer Cells. *Langmuir*, (2014).
105. Z. Xiao, N. Zhang, D. B. Murphy, P. N. Devreotes, Dynamic distribution of chemoattractant receptors in living cells during chemotaxis and persistent stimulation. *Journal of Cell Biology* **139**, 365-374 (1997).
106. M. W. Conklin, J. C. Eickhoff, K. M. Riching, C. A. Pehlke, K. W. Eliceiri, P. P. Provenzano, A. Friedl, P. J. Keely, Aligned Collagen Is a Prognostic Signature for Survival in Human Breast Carcinoma. *The American Journal of Pathology* **178**, 1221-1232 (2011).
107. S. R. Deans, *The Radon Transform and Some of Its Applications*. Dover Books on Mathematics Series (Dover Publications, Mineola, New York, 2007).

108. W. Edwards, A. T. Moles, P. Franks, The global trend in plant twining direction. *Global Ecology and Biogeography* **16**, 795-800 (2007).
109. Y. Shibazaki, M. Shimizu, R. Kuroda, Body handedness is directed by genetically determined cytoskeletal dynamics in the early embryo. *Current Biology* **14**, 1462-1467 (2004).
110. K. Taniguchi, R. Maeda, T. Ando, T. Okumura, N. Nakazawa, R. Hatori, M. Nakamura, S. Hozumi, H. Fujiwara, K. Matsuno, Chirality in Planar Cell Shape Contributes to Left-Right Asymmetric Epithelial Morphogenesis. *Science* **333**, 339-341 (2011).
111. A. Raya, J. C. Izpisua Belmonte, Left-right asymmetry in the vertebrate embryo: from early information to higher-level integration. *Nature Reviews Genetics* **7**, 283-293 (2006).
112. S. Nonaka, H. Shiratori, Y. Saijoh, H. Hamada, Determination of left-right patterning of the mouse embryo by artificial nodal flow. *Nature* **418**, 96-99 (2002).
113. M. Levin, Left–right asymmetry in embryonic development: a comprehensive review. *Mechanisms of Development* **122**, 3-25 (2005).
114. S. Aw, M. Levin, What's left in asymmetry? *Developmental Dynamics* **237**, 3453-3463 (2008).
115. D. Qiu, S.-M. Cheng, L. Wozniak, M. McSweeney, E. Perrone, M. Levin, Localization and loss-of-function implicates ciliary proteins in early, cytoplasmic roles in left-right asymmetry. *Developmental Dynamics* **234**, 176-189 (2005).
116. M. V. Danilchik, E. E. Brown, K. Riegert, Intrinsic chiral properties of the Xenopus egg cortex: an early indicator of left-right asymmetry? *Development* **133**, 4517-4526 (2006).
117. J. Xu, A. Van Keymeulen, N. M. Wakida, P. Carlton, M. W. Berns, H. R. Bourne, Polarity reveals intrinsic cell chirality. *Proceedings of the National Academy of Sciences* **104**, 9296-9300 (2007).
118. M. Sameshima, Y. Imai, Y. Hashimoto, The position of the microtubule-organizing center relative to the nucleus is independent of the direction of cell migration in dictyostelium discoideum. *Cell Motility and the Cytoskeleton* **9**, 111-116 (1988).
119. R. J. Eddy, L. M. Pierini, F. R. Maxfield, Microtubule asymmetry during neutrophil polarization and migration. *Molecular Biology of the Cell* **13**, 4470-4483 (2002).
120. J. Xu, F. Wang, A. Van Keymeulen, M. Rentel, H. R. Bourne, Neutrophil microtubules suppress polarity and enhance directional migration. *Proceedings of the National Academy of Sciences* **102**, 6884-6889 (2005).
121. S. L. Gupton, W. C. Salmon, C. M. Waterman-Storer, Converging populations of f-actin promote breakage of associated microtubules to spatially regulate microtubule turnover in migrating cells. *Current Biology* **12**, 1891-1899 (2002).
122. W. C. Salmon, M. C. Adams, C. M. Waterman-Storer, Dual-wavelength fluorescent speckle microscopy reveals coupling of microtubule and actin movements in migrating cells. *Journal of Cell Biology* **158**, 31-37 (2002).

123. V. Niggli, Microtubule-disruption-induced and chemotactic-peptide-induced migration of human neutrophils: implications for differential sets of signalling pathways. *Journal of Cell Science* **116**, 813-822 (2003).